ISBN 978-82-326-5130-6 (printed ver.)
ISBN 978-82-326-5131-3 (electronic ver.)
ISSN 1503-8181 (printed ver.)
ISSN 2703-8084 (electronic ver.)

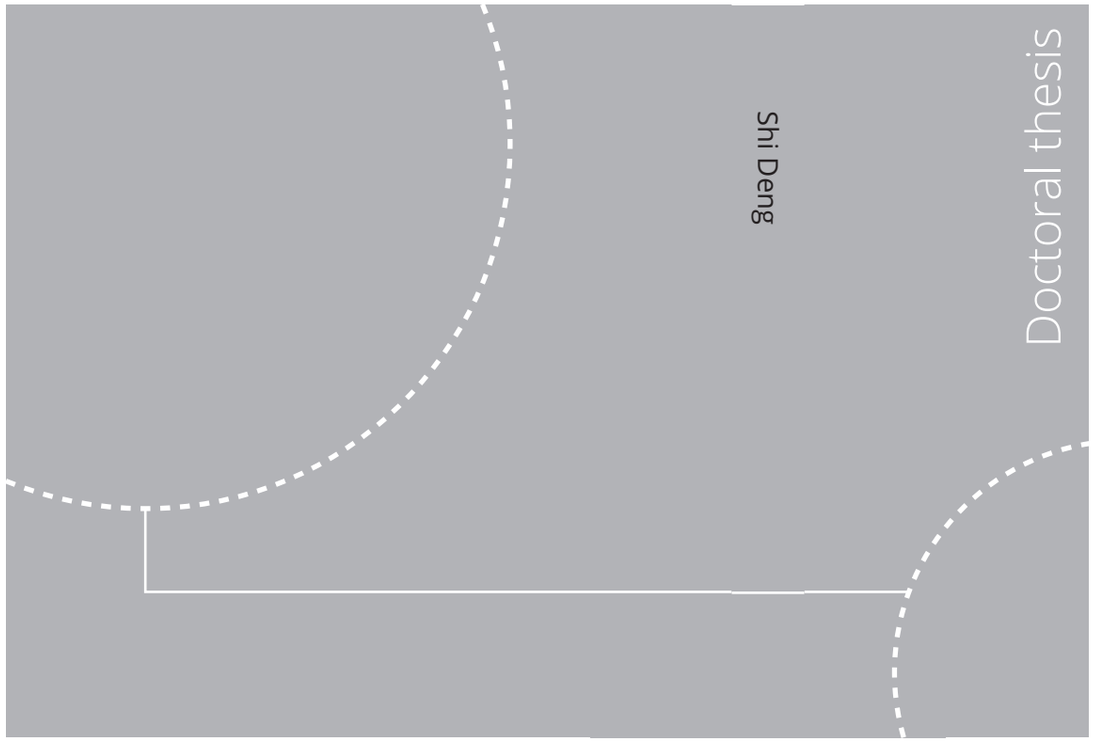


Doctoral theses at NTNU, 2020:392

Shi Deng

# Experimental and numerical study of hydrodynamic responses of a twin-tube submerged floating tunnel considering vortex-induced vibration

NTNU
Norwegian University of Science and Technology

Doctoral theses at NTNU, 2020:392

**NTNU**
Norwegian University of Science and Technology
Thesis for the degree of Philosophiae Doctor
Faculty of Engineering
Department of Marine Technology

NTNU
Norwegian University of Science and Technology

Shi Deng

# Experimental and numerical study of hydrodynamic responses of a twin-tube submerged floating tunnel considering vortex-induced vibration

Thesis for the degree of Philosophiae Doctor

Trondheim, December 2020

Norwegian University of Science and Technology
Faculty of Engineering
Department of Marine Technology

NTNU
Norwegian University of
Science and Technology

**NTNU**
Norwegian University of Science and Technology

Thesis for the degree of Philosophiae Doctor

Faculty of Engineering
Department of Marine Technology



ISBN 978-82-326-5130-6 (printed ver.)
ISBN 978-82-326-5131-3 (electronic ver.)
ISSN 1503-8181 (printed ver.)
ISSN 2703-8084 (electronic ver.)

Doctoral theses at NTNU, 2020:392

PRINTED IN NORWAY
NO - 1598

NORDIC SWAN ECOLABEL
Printed matter
2041 0731

Printed by Skipnes Kommunikasjon AS

# Abstract

A pontoon-supported submerged floating tunnel (SFT) is a reasonable means crossing a fjord with large depth and width. A relevant design of such a tunnel consists of two identical tubes in a tandem configuration and suspended approximately 20-30 $m$ below the mean sea level. The two tubes are rigidly connected by large diameter diagonal truss elements. The natural frequencies of the low-order modes of the full-scale SFT (the first vertical motion-dominant mode and the first two lateral motion-dominant modes) are well within the energy content of the spectrum of vortex shedding induced forces and the difference-frequency wave excitation force. The vortex-induced vibration (VIV) and wave-induced hydroelastic response represent the main challenges in the design of the SFT. Regarding the above two considerations, this work aims at investigating the following aspects: (1) VIV features of a tandem twin-cylinder model and the lift and drag coefficients used in the simplified time domain VIV prediction method. (2) Hydrodynamic features of the SFT considering the $2^{nd}$ order wave force acting on pontoons, short-crested waves and VIV.

A series of self-oscillation tests were first conducted with an elastically supported rigidly connected tandem twin rigid-cylinder model, to gain a better understanding of the VIV features of an SFT with respect to the flow velocity, spacing distance and submergence. Nondimensional parameters including the reduced velocity, spacing and submergence ratios build relations between the test model and prototype. The crossflow (CF) response amplitude and lift force coefficients were observed to be strongly related to the spacing distance and flow velocity, as expected. The interaction between the twin cylinders leads to a smaller critical reduced velocity (corresponding to the initiation of the VIV) and response frequency than those of a single cylinder when the spacing ratio is less than 4. The lift forces on the two cylinders strongly depend on the reduced velocity, but their rates of change are different. This difference induces an extra torsional moment, which is also sinusoidal in time but quadratic in the flow velocity. An abrupt in-

crease in the torsional moment is observed at a small reduced velocity when the spacing ratio is 2, and a large final constant value is found in the case of a spacing ratio equal to 4. In addition to the CF lift forces, VIV also strongly amplifies the inline (IL) drag forces, and they achieve their maxima coincidently with the response amplitude. Two drag forces are in direction with each other in the VIV condition rather than opposite directions in stationary result for spacing ratios of 2 and 3. The influence of the free surface on the response amplitude and drag forces can be neglected when the newly defined nondimensional depth h' ($h' = \frac{f_n h}{U}$, where $U$, $f_n$ and $h$ denote the flow velocity, natural frequency and submergence, respectively) is larger than 0.55.

Regarding the wave-induced hydroelastic features, the $2^{nd}$ order wave forces dominate the lateral motion by exciting the low frequency eigenmodes but have small effects on the vertical motion. The long-crest first order waves induce nearly twice as large lateral bending moments ($M_z$) as short-crest waves, by including the $2^{nd}$ order forces, the short-crest waves lead to a large $M_z$ due to that they can excite both the $1^{st}$ and $2^{nd}$ natural modes in the lateral direction. Based on the simplified VIV prediction method (in which, the crossflow hydrodynamic force is modelled as a summation of the vortex-induced force relying on self-oscillation tests and the damping force based on the Morison equation), the maximum standard deviation of the vertical motion ($STD/D \approx 0.31$) and the corresponding bending moment at the middle part is much larger than that induced by the long-crest waves. Except for the VIV in the central long span between pontoons, the VIV excitation is limited.

# Preface

This thesis is submitted to the Norwegian University of Science and Technology (NTNU) for partial fulfillment of the requirements for the degree of philosophiae doctor.

This doctoral work has been performed at Department of Marine Technology, NTNU, Trondheim. Professor Torgeir Moan from Department of Marine Technology, NTNU is the main supervisor. Professor Shixiao Fu from the School of Naval Architecture, Ocean and Civil Engineering, SJTU and NTNU as well as Professor Zhen Gao from Department of Marine Technology, NTNU are the co-supervisors.

The work was financially supported by a scholarship from Department of Marine Technology, NTNU from June 2018 to August 2020, which is greatly appreciated. The financial support from NPRA to carry out experiments is also acknowledged.

# Acknowledgment

First of all, I would like to appreciate my supervisors, Prof.Torgeir Moan, Prof.Shixiao Fu and Prof.Zhen Gao for their excellent guidance during this work. They are positive, enthusiastic and supportive, but, as true scientists, they are also skeptical and critical at all research problems. Besides the knowledge on hydroelasticity and VIV, they also provide a remarkable example of lifelong learning in their daily work.

I would like to extend my gratitude to Assistant Prof.Yuwang Xu. During the PhD study, his valuable suggestions and strong pushing helped me a lot when I was struggling. I would also like to thank my colleague Haojie Ren. He visited NTNU during the Chinese new year in 2018. Without his help, the experiments could not have been conducted. I also wish to express my thanks to NTNU laboratory staff, Torgeir Wahl, Terje Rosten, Trond Innset and Emil Bratlie for their assistance with the experiments.

I also greatly appreciate the help from Dr. Mengmeng Zhang and Shuai Li for their patient discussion on the VIV prediction and hydroelastic analysis methods. Thanks are also extended to Prof. Erin Bachynski for her kind ideas when I was stuck with software. I would like to appreciate the time and work of my thesis committee members: Prof. John M. Niedzwecki, Dr. Narakorn Srinil and Prof.Svein Saevik.

Thanks to all my friends and colleagues at the Department of Marine Technology for making this long study a fun and pleasant experience. All the support and memory have become the highlights of my life. Finally, I want to express my deep gratitude to my family: my parents and girlfriend. Your love and understanding means everything to me.

Norwegian Public Roads Administration (NPRA) is gratefully acknowledged for the financial support of the lab-test.

Shi Deng
December 2020
Trondheim, Norway

# List of Appended Papers

## List of Appended Papers

**Paper 1:**
Deng S, Ren H, Xu Y, Fu S, Moan T, Gao Z. Experimental Study of Vortex-Induced Vibration of a Twin-tube Submerged Floating Tunnel Segment Model.*Journal of Fluids and Structures* 2020; **94**(3):102908.

**Paper 2:**
Deng S, Ren H, Xu Y, Fu S, Moan T, Gao Z. Experimental Study on the Drag Forces on a Twin-tube Submerged Floating Tunnel Segment Model in Current. *Applied Ocean Research* 2020. **104**:102326.

**Paper 3:**
Deng S, Xu Y, Ren H, Fu S, Li S, Moan T, Gao Z. Numerical simulation of wave-induced hydroelasticity and flow-induced vibration of a twin-tube submerged floating tunnel. *Prepare to submit.*

The first author of the papers was responsible for self-oscillation test of twin-cylinder model, post-processing of test data, numerical simulations, model verification and manuscript writing. Haojie Ren provided assistant in the experiments. Shuai Li and Prof. Yuwang Xu contributed with improving the scientific quality of the paper. Prof. Torgeir Moan, Shixiao Fu and Zhen Gao provided supervision on the project.

## List of Additional Papers (not included in the thesis)

**Paper 1:**
Deng S, Fu S, Moan T, Wei W, Gao Z. Hydro-Elastic Analysis of a Floating Bridge in Waves Considering the Effect of the Hydrodynamic Coupling and the Shore Sides. *ASME 2018 37th International Conference on Ocean, Offshore and Arctic Engineering*, American Society of Mechanical Engineers,

2018; V001T01A039.

**Paper 2:**
Deng S, Li S, Xu Y, Moan T, Fu S, Gao Z. Numerical study on the dynamic response of a submerged floating tunnel under current loads based on the segment model towing test results. *The 30th International Ocean and Polar Engineering Conference*, International Society of Offshore and Polar Engineers, 2020.

# Glossary

## List of Abbreviations

| | |
|---|---|
| **CFD** | Computational Fluid Dynamics |
| **CF** | Crossflow |
| **HPC** | High Performance Computing |
| **IL** | Inline |
| **MC-lab** | Marine Cybernetics Laboratory |
| **NPRA** | Norwegian Public Roads Administration |
| **NTNU** | Norwegian University of Science and Technology |
| **SFT** | Submerged Floating Tunnel |
| **STD** | Standard Deviation |
| **VIV** | Vortex Induced Vibration |
| **VLFS** | Very Large Floating Structure |

## Nomenclature

| | |
|---|---|
| $\alpha$ | spectral parameter |
| $\beta$ | form parameter |
| $\gamma$ | peakedness parameter |

| | |
|---|---|
| $\hat{f}$ | non-dimensional frequency |
| $\lambda$ | spacing ratio |
| $\Phi$ | wave potential |
| $\rho$ | fluid density |
| $\theta$ | wave direction angle |
| $\varphi$ | initial phase of lift force |
| $\zeta$ | structural damping ratio |
| $A^*$ | amplitude ratio |
| $C_A$ | added mass coefficient |
| $C_a$ | potential added mass coefficient |
| $C_D$ | mean drag coefficient |
| $C_L$ | lift coefficient |
| $C_T$ | torsional coefficient |
| $C_{La}$ | VIV-induced added mass coefficient |
| $C_{Le}$ | VIV-induced excitation coefficient |
| $D$ | cylinder diameter |
| $D(\theta)$ | direction distribution |
| $f^*$ | frequency ratio |
| $F_D$ | drag force |
| $F_L$ | lift force |
| $F_m$ | measured force |

| | |
|---|---|
| $f_n$ | natural frequency in still water |
| $F_z$ | lift force amplitude |
| $Fr$ | Froude number |
| $g$ | gravitational acceleration |
| $h$ | submerged depth, from lower side of the cylinder to the undisturbed free surface |
| $h'$ | non-dimensional submerged depth |
| $h^*$ | submergence ratio |
| $H_s$ | significant wave height |
| $k$ | spring stiffness |
| $L$ | center-to-center distance between two cylinders |
| $l$ | cylinder length |
| $L_T$ | effective length of the MC-towing tank |
| $m^*$ | mass ratio |
| $m_d$ | displaced fluid mass |
| $M_y$ | vertical bending moment |
| $M_z$ | lateral bending moment |
| $R_e$ | Reynolds number |
| $S(\omega)$ | unidirectional wave spectrum |
| $St$ | Strouhal number |
| $T$ | torsional moment |
| $t$ | time |

| | |
|---|---|
| $T_p$ | peak period |
| $U$ | flow velocity |
| $U_M$ | maximum velocity in the oscillatory flow |
| $Ur$ | reduced velocity |
| $y$ | inline displacement/lateral displacement |
| $z$ | cross flow displacement/vertical displacement |
| $N_{osc.}$ | number of stable cycles |
| $S_\xi(\omega_n, \theta_m)$ | directional wave spectrum |
| $T^1$ | transfer function of the $1^{st}$ order wave force |
| $T^2$ | transfer function of the $2^{nd}$ order wave force |
| $C_{D\_\delta}$ | coefficient of drag force difference |
| $C_{D\_T}$ | coefficient of total drag force |

# Contents

# List of Figures

# List of Tables

# Chapter 1

# Introduction

## 1.1 Background and Motivation

Transport across channels or straits can be accommodated by ferry connections, under seabed tunnels and bridges. For the fjords with large width and water depth, low transportation efficiency and large construction cost of the first two methods limit their usage. The Norwegian Public Road Administration (NPRA) is conducting a 'Ferry free coastal route E39' project [1–3]. Surface crossing floating bridges and submerged floating tunnels (SFTs) are planned to replace the ferry connections along the coastal highway, as shown in Fig. 1.1. Because of the smaller wave-induced motions for the latter concept, the SFT is attractive for the fjords always with high wave conditions. So far two typical SFT concepts have been proposed, i.e. tether- and pontoon-supported, as shown in Fig. 1.2. The design considered in this study is a twin-tube pontoon supported SFT. Most of the fjords are wide and deep. For instance, the Sognefjorden has a width of 3.7 $km$ and a depth of up to 1.25 $km$, the Bjornafjorden has a length of over 5 $km$ and a depth of approximately 0.55 $km$. Therefore, the large scale and fully submerged twin-tube structures of the SFT demand a significant extension of present bridge technology.


*Figure 1.1: Fjords along the E39 coastal highway.*

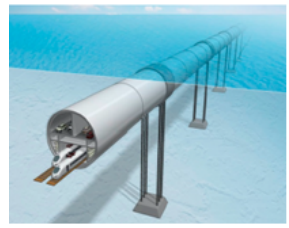

a. Tether support SFT

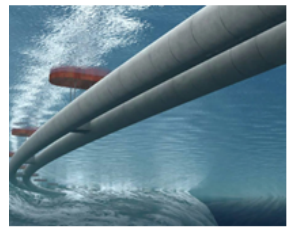

b. Pontoon support SFT

*Figure 1.2: Typical SFTs considered for fjords.*

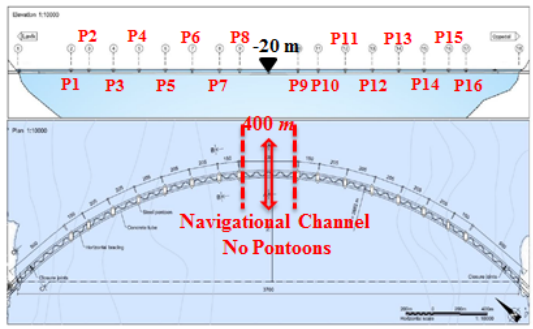


*Figure 1.3: Twin-tube pontoon-supported submerged floating tunnel for Sognefjorden, submergences highlighted in the figure defined by the distance from the upper side of the tunnel tube to the mean sea level.*

## 1.2 Hydroelasticity and VIV of pontoon supported submerged floating tunnel induced by wave and current

The SFT is a good choice for crossing fjords with a large width and depth. It also conveniently provides a ship passage, but implies some challenges.

Different from the surface crossing floating bridge, the wave and current loads could become equally important challenges for the design of the SFTs, as illustrated in Fig.1.4. Waves in a fjord are quite moderate compared with those in the open sea. For instance, typical $H_s$ and $T_P$ with 100-year return period in Sognefjorden and Bjornafjorden are about 2.0-2.5 $m$ and about 5-7 $s$, respectively. Moreover, the wave conditions in a fjord are inhomogeneous. The wave actions are comprised of the excitation forces on the pontoons and tubes, and the radiation forces induced by the motions of them. The current velocity in a fjord is related to the water depth, for instance it is around 0.9-1.8 $m/s$ at surface, but 0.45-0.70 $m/s$ at water depth of 30 $m$. The current actions consist of a time invarient mean drag force and fluctuating drag and crossflow lift forces [4–7].

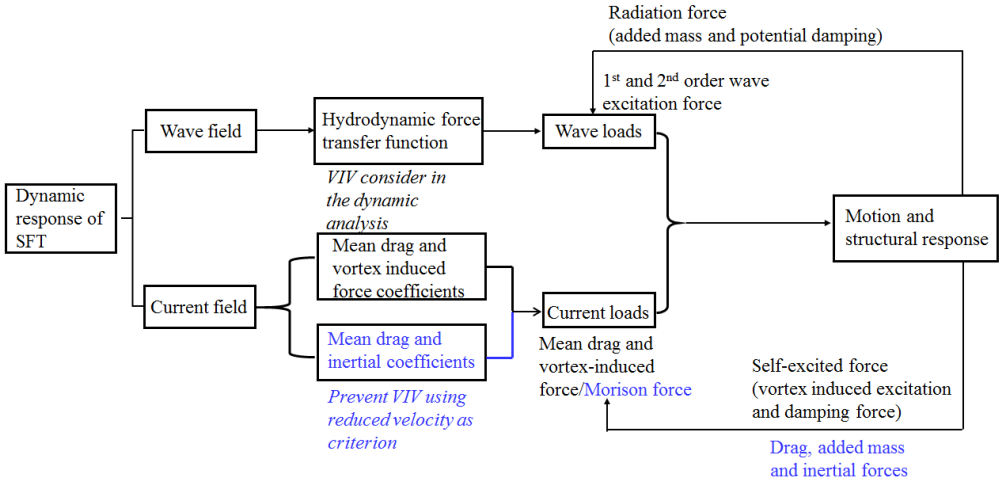


*Figure 1.4: Loads and responses of a submerged floating tunnel, blue part shows an conventional way for current loads calculation.*

For a very large floating structure (VLFS), like SFT, the coupling between the structural deformations and wave motions cannot be neglected. Previous researchers have proposed hydroelastic analysis methods including the modal superposition method [8–10], and discrete-module-based method [11, 12]. Kvale, Wu, Bishop and Seif et al. [13–17] developed frequency domain methods with high computational efficiency and used the methods in the hydroelastic analysis of floating airports, ships and floating bridges. Based on the latter one, Fu, Li, Wei and Cheng et al. [18–21] proposed a time-domain method considering the effects of nonlinear wave excitation forces, nonlinear connectors and inhomogeneous wave fields. In these meth-

ods mentioned above, the excitation and radiation wave forces were calculated by potential panel theory. For a slender SFT, with a large diameter circular cross section, the wave forces could be calculated by the Morison equation or potential flow theory. Kinisu et al. [22, 23] found that the two methods gave a similar result when $KC < 15$ at the submergence of 50 $m$, meaning that the inertial force was predominant.

Since the high frequency vortex-induced vibration (VIV) may lead to rapid accumulation of the fatigue damage and VIV-amplified inline drag loads may change the static deflection, VIV is conventionally to be avoided in the design. Two typical methods are usually adopted for the VIV prevention based on the reduced velocity ($U_r = \frac{U}{f_n D}$, where $f_n$ is the natural frequency and $D$ is the cylinder diameter), i.e. stiffen the structure or modify the cross section features (such as Helical strakes). However, such methods increase the structural cost.

For the VIV analysis of the SFT, anchor cables of the tether-supported concept has been studied. Chen et al. [24] found that, in a strong current condition, the cables could suffer a severe intermittent VIV and the vibration was significantly dominated by the lateral motion of the tunnel tube. For the cables with large aspect ratios, used for the SFT in large water depth, Wu et al. [25] proposed a modified wake oscillator model in VIV prediction and found VIV could excite several natural modes with high frequencies. Where, the traveling wave rather than standing wave will dominate the responses. The maximum response was observed in the travelling wave dominant region with high probability of fatigue damage. Ge et al, [26] studied the inline (IL) VIV of the cables in a coupled wave and current condition, and built a relationship between the wave frequency and IL VIV response amplitude. Xiang [27] proposed a theoretical model for the coupled tube-cable vibration to calculate the dynamic response of a SFT under a uniform current.

However, all the studies mentioned above are focused on SFTs with only one tube moored on the seabed. Virtually, no reference on the pontoon supported twin-tube concept has been published before, while the hydrodynamic features would be very different. On one hand, the wave induced load effects would be more significant due to the floating pontoons on the sea surface. On the other hand, the VIV features would be more complex owing to the interaction between the two identical tubes arranged in tandem. Vortex induced forces on the tubes have never been studied before, even for the single-tube SFT system. The published research mainly refers to the VIV of the anchor cables.

In line with the VIV study of the single cylinder, self-oscillation tests

of a rigidly connected tandem twin-rigid-cylinder will be conducted to gain the understandings of the VIV features and obtain lift and drag coefficients. Then, a simplified time domain VIV prediction method is further proposed to calculate the vibration in CF direction. VIV amplified IL drag force is also considered based on the laboratory test result in the calculation of the response in IL direction. At last, the dynamic response of the SFT in wave conditions will be numerically simulated where the effects of the $1^{st}$- and $2^{nd}$-order wave loads and long- and short-crested waves are evaluated. Hydrodynamic response of the SFT under the VIV condition is discussed compared with the wave-induced response, and a probable way to decrease the maximum response amplitude is further proposed to decrease the potential cost on VIV prevention.

## 1.3 Objectives of this thesis

The purpose of this study is to gain insight in the wave-induced hydroelastic and flow-induced vibration features of a twin-tube SFT. A conventional discrete-module-based time-domain method is adopted for the former objective considering the $1^{st}$- and $2^{nd}$-order wave forces and long- and short-crested waves. For the latter objective, the study starts by conducting self-oscillation tests of twin cylinders to understand the effects of the flow velocity and spacing distance on the VIV, and obtain the key parameters i.e. lift and mean drag coefficients. Then a simplified time-domain VIV prediction method is proposed and adopted for the simulation with limited date base stemming from self-oscillation tests. The overall objective is completed through a number subgoals, as follows,

- Based on the self-oscillation tests, build relations between the flow velocity (represented by the reduced velocity) and response amplitude. Critical range of the reduced velocity is defined by the occurrence of significant VIV. These results are used to measure the likelihood of lock-in in the VIV analysis.
- Based on the self-oscillation tests, the lift force coefficients, frequencies of the up- and downstream cylinders are obtained with respect to the flow velocity and spacing distance, as well as the phase difference between the two lift forces.
- Based on the self-oscillation tests, the mean drag coefficients of the two cylinders are obtained in terms of the flow velocity and spacing distance.

- Proposal of a simplified VIV prediction method in time domain based on the self-oscillation test results.

- Predict wave-induced hydroelasticity and flow-induced vibration of an SFT. Propose a way for reducing the maximum VIV response to the level.

## 1.4 Thesis organization

This thesis is written as a collection of articles, which are appended in full-length after the main section. These articles represent the research contributions from this work, while the main section is meant to provide an overview of the hydroelastic analysis method, VIV features for a single cylinder system and the corresponding prediction methods, as well as series of self-oscillation tests of twin cylinders and the numerical simulations. The remaining part of the thesis is organized as follows:

- **Ch. 2** contains a theoretical background of the hydroelastic analysis method for a VLFS in wave fields, focusing on the discrete-module-based method. In addition, the background of VIV analysis including the model test based-mechanism study and prediction method in frequency- and time-domain are described. Previous research on the VIV of a tandem twin-cylinder is summarized at last.

- **Ch. 3** describes the self-oscillation test of a twin-tube SFT segment model in purely CF directions.

- **Ch. 4** reveals the main findings of the test and also represents an extended summary of all the three research papers. The VIV features of the tandem twin cylinders are first described, followed by the lift and drag coefficients, which are the foundations of the dynamic analysis (Paper I and II). Then, the hydroelastic and VIV features of the SFT are revealed by the numerical simulations (Paper III), as shown in Fig.1.5.

- **Ch. 5** presents conclusions and the suggestions for future work based on the limitations of the present study.

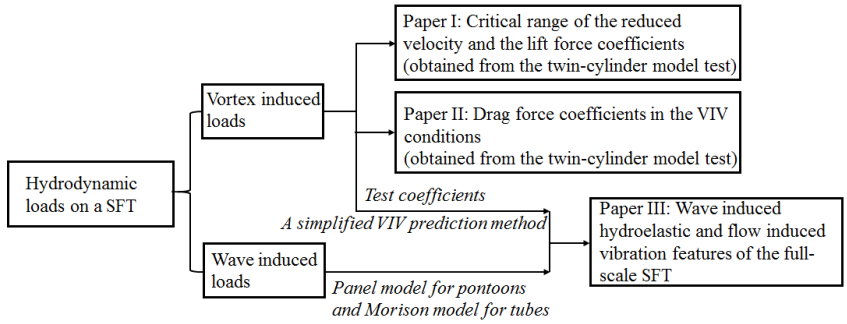


*Figure 1.5: Main results in the attached papers.*

# Chapter 2

# Theoretical Background

For a deeply submerged SFT with 4 $km$ length, wave-induced hydroelasticity and flow induced vibration are two of the main challenges in the hydrodynamic analysis. The conventional discrete-module-based hydroelastic analysis method has been proposed [11, 12], where the wave excitation and radiation forces on the pontoons are obtained from potential panel theory, the forces on the tubes are obtained from Morison equation, while the structural properties are modeled by beam elements. For the flow induced vibration, in line with the mature VIV research procedure of a single cylinder, the study is started by the fundamental features of VIV of twin cylinders.

This chapter starts from a theoretical background of the hydroelasticity theory analysis, followed by a review of VIV studies, including flow around a single cylinder, vortex-induced force, basic VIV features from self-oscillation test, VIV prediction methods and coefficients acquirement from forced oscillation test. Recent researches on twin-cylinder will be summarized at last.

## 2.1 Wave-induced hydroelastic analysis

A pontoon supported SFT can be regarded as series of rigid floating modules (pontoons) connected by elastic beams (tunnel tubes). Hydrodynamic analysis of such a structure under wave loads is quite similar to conventional 'discrete-modules-based' hydroelastic analysis [11]. The wave loads acting on the modules can be calculated by means of potential panel theory. For the tunnel tubes, the wave loads can be obtained using the Morison equation. Theoretical background will cover wave field description, wave loads calculation on floating structures and equations of motions for the complete SFT in waves.

### 2.1.1 Wave field description

Because of the complex topography, waves in a fjord are quite different from these in the open sea. Based on the field measurements and numerical simulations, Cheng and Fjeld et al. [3,21,28] proposed a suitable wave spectrum model and it is used directly in this study, by assuming a homogeneous wave condition. For a short-term sea state, the wave field can be regarded as Gaussian and stationary, and the wave elevation at any point can be expressed as a sum of all component waves from different directions

$$\xi(t) = R\left\{\sum_{n=1}^{N}\sum_{m=1}^{M}\sqrt{2S_{\xi}(\omega_n,\theta_m)\,\Delta\omega\Delta\theta}\,\exp\left[i\left(\omega_n t - k_n x\cos\theta_m - k_n y\sin\theta_m + \varepsilon_{nm}\right)\right]\right\} \tag{2.1}$$

where, $N$ and $M$ are the total numbers of wave frequency components and wave direction components, respectively. $\varepsilon_{nm}$ is the random initial phase $(0 \sim 2\pi)$ for each wave component. $x$ and $y$ are the position coordinates, $\theta$ is the wave direction angle, and $k$ is the wavenumber. $S_{\xi}(\omega_n,\theta_m)$ denotes the directional wave spectrum and is a function of frequency and direction

$$S_{\xi}(\omega_n,\theta_m) = S(\omega)\,D(\omega,\theta) \tag{2.2}$$

where $S(\omega)$ is the unidirectional wave spectrum and $D(\omega,\theta)$ symbolizes the direction distribution. The directional function for locally generated sea states is commonly approximated as being independent of frequency, i.e. $D(\omega,\theta) = D(\theta)$. The unidirectional wave spectrum has been defined by JONSWAP [29],

$$S(\omega) = \frac{\alpha g^2}{\omega^5}\exp\left[-\beta\left(\frac{\omega_p}{\omega}\right)^4\right]\gamma^{\exp\left(\frac{(\omega/\omega_p-1)^2}{2\sigma^2}\right)} \tag{2.3}$$

where

$$\begin{aligned}
&\alpha = 5.061\frac{H_s^2}{T_P^4}\left(1-0.287\ln(\gamma)\right)\\
&\omega_p = \frac{2\pi}{T_P}\\
&\sigma = \begin{cases} 0.07 & for \quad \omega < \omega_p \\ 0.09 & for \quad \omega \geq \omega_p \end{cases}
\end{aligned} \tag{2.4}$$

where $\alpha$ is the spectral parameter, $\beta$ is the form parameter and is chosen to be 1.25, and $\gamma$ is the peakedness factor. According to the metocean design basis [30] the peakedness factor estimated with the following expression.

$$\gamma = \begin{cases} 5 & for \quad \frac{T_P}{H_s} \leq 3.6 \\ exp\left(5.75 - 1.15\frac{T_P}{\sqrt{H_s}}\right) & for \quad 3.6 < \frac{T_P}{H_s} < 5 \\ 1 & for \quad \frac{T_P}{H_s} \geq 5 \end{cases} \tag{2.5}$$

The direction follows a $cos - s$ distribution, as follows,

$$D(\theta) = \frac{\Gamma(1 + s/2)}{\sqrt{\pi}\,(1/2 + s/2)} \cos^s(\theta - \theta_p) \tag{2.6}$$

where $s$ is the spreading exponent, and it set to 4 for short-crested waves. $\theta_p$ is the main wave direction and $|\theta - \theta_p| \leq \frac{\pi}{2}$,

### 2.1.2 Wave loads on floating modules

Firstly, author has revealed that the hydrodynamic coupling between adjacent supporting pontoons has little effect on the dynamic response when the spacing between adjacent pontoons is approximately 10 times of its width [31]. Therefore, all pontoons will be treated as independent floating structures in the wave loads calculation. Moreover, the hydrodynamic coupling between the pontoons and tunnel tubes is also neglected.

Wave loads on a floating structure in the ideal fluid, i.e. incompressible, irrotational and inviscid can be addressed by wave potential, which is the sum of incident, diffraction and radiation components.

$$\Phi = \Phi_I + \Phi_D + \Phi_R \tag{2.7}$$

Typically, the incident potential is known based on wave theory. From Laplace equation and boundary conditions (including free surface, sea bottom, radiation and body surface), the diffraction and radiation potential can be calculated. Boundary conditions for diffraction potential are listed below as an example,

$$\begin{cases} -\omega^2 \Phi_D + g \frac{\partial \Phi_D}{\partial z}\Big|_{z=0} = 0 \\ \frac{\partial \Phi_D}{\partial n} = \frac{\partial \Phi_I}{\partial n} \\ \frac{\partial \Phi_R}{\partial n}\Big|_{S_B} = 0 \\ \lim\limits_{r \to \infty} \left[ r^{1/2} \left( \frac{\partial \Phi_D}{\partial r} - ik\Phi_D \right) \right] = 0 \end{cases} \tag{2.8}$$

Based on Bernoulli equation, the wave excitation force can be obtained by the incident and diffraction potential, while the added mass and damping can be obtained by the radiation potential.

The first-order excitation force transfer function can be estimated in the frequency domain as $T_j^1(\omega, \theta)$ ($j$ is the degree of freedom). This function represents the force generated by a unit regular wave with a frequency of $\omega$ and a propagation direction of $\theta$. Thus, the total first-order wave force can

be estimated by,

$$F_j^1(x,y,t) = R\left\{\sum_{n=1}^{N}\sum_{m=1}^{M} \begin{array}{l} \left|T_j^1(\omega_n,\theta_m)\right|\sqrt{2S_\xi(\omega_n)D(\theta_m)\Delta\omega\Delta\theta} \\ \exp\left[i\left(\omega_n t - k_n x\cos\theta_m - k_n y\sin\theta_m + \varepsilon_{nm} + \phi_{T^1_{jnm}}\right)\right] \end{array}\right\} \tag{2.9}$$

where $\phi_{T^1_{jnm}}$ is the phase angle of the wave force transfer function.

Relying on the derivation of the autocorrelation function and the Wiener-Khinchin relation, the spectra of the first-order wave force can be obtained as follows:

$$S_{F_j^1}(\omega) = \int_{-\pi}^{\pi} T_j^1(\omega,\theta) S_\xi(\omega) D(\theta) T_j^{1*}(\omega,\theta)\, d\theta \tag{2.10}$$

where the asterisk $*$ is the complex conjugate. For a unidirectional wave field, the former equation can be re-written as

$$S_{F_j^1}(\omega) = T_j^1(\omega) S_\xi(\omega) T_j^{1*}(\omega_n) \tag{2.11}$$

In this time domain analysis, the first-order wave force spectra are obtained from the wave spectra and the transfer function.

For a floating structure in an irregular wave field, the second-order difference-frequency wave load is important. Two typical methods are usually applied to address this problem: the quadratic transfer function (QTF) based on the near field method and the Newman assumption. The former one is very time consuming and depends on first-order motions, which are difficult to obtain, especially for an SFT with motion coupling between the modules and beams. Admittedly, all components ($\omega_i$,$\omega_j$) in the QTF contribute to the second order wave force, but the values tend to be very small. The effect will be significant only when the frequency is close to one of the natural frequencies. Therefore, for the low-frequency lateral-motion of a floating structure, Newman proposed a method that consists of replacing each component ($\omega_i$,$\omega_j$) with the mean of the (($\omega_i$,$\omega_i$) and ($\omega_j$,$\omega_j$)) components.

$$T(\omega_i,\omega_j) = \frac{1}{2}\left[T(\omega_i+\omega_i) + T(\omega_j+\omega_j)\right] \tag{2.12}$$

Similar to the first order wave load, the second order difference-frequency wave force can be expressed in terms of the transfer function and wave spectrum,

$$F_j^2(x,y,t) = R\left\{\sum_{l=1}^{N}\sum_{n=1}^{N}\sum_{m=1}^{M} \begin{array}{l} \left|T_j^2(\omega_l,\omega_n,\theta_m)\right|\sqrt{2S_\xi(\omega_n)D(\theta_m)\Delta\omega\Delta\theta} \\ \sqrt{2S_\xi(\omega_l)D(\theta_m)\Delta\omega\Delta\theta} \\ \exp\left[i\left((\omega_l-\omega_n)t + \varepsilon_{lm} - \varepsilon_{nm} + \phi_{T^2_{jlnm}}\right)\right] \end{array}\right\} \tag{2.13}$$

where $T_j^2(\omega_l, \omega_n, \theta_m)$ denotes the difference-frequency transfer function, which can be simplified by Newman assumption to

$$T_j^2(\omega_l, \omega_n, \theta_m) = \frac{1}{2}\left[T_j^2(\omega_l, \omega_l, \theta_m) + T_j^2(\omega_n, \omega_n, \theta_m)\right] \tag{2.14}$$

The spectra of second-order difference-frequency wave forces can be written as,

$$S_{F_j^2}(\omega) = 8\int_0^\infty \int_{-\pi}^{\pi} \begin{array}{l} \int_{-\pi}^{\pi} T_j^2(\omega, \omega+\mu, \theta) S_\xi(\omega)\, D(\theta) \\ S_\xi(\mu-\omega)\, D(\theta)\, T_j^{2*}(\omega, \omega+\mu, \theta)\, d\theta \end{array} \tag{2.15}$$

### 2.1.3 Equations of motions for the complete SFT in waves

In this study, the pontoons are modeled as rigid floating structures. Their hydrodynamic coefficients, such as the added mass and radiation damping, and wave excitation forces are obtained as discussed above. The pontoons are connected by the tunnel tubes, which are simplified as elastic beams in the finite element model. The dynamic motion equations of the whole tunnel structure can be expressed as follows,

$$\begin{aligned} &[M + A + m + a(\infty)]_{6N\times 6N}\{\ddot{y}(t)\}_{6N\times 1} + \int_{-\infty}^{t} [H(t-\tau)]_{6N\times 6N}\{\dot{y}(t)\}_{6N\times 1} d\tau + \\ &[C]_{6N\times 6N}\{\dot{y}(t)\}_{6N\times 1} + [K + k]_{6N\times 6N}\{y(t)\}_{6N\times 1} = \left[F_{exc.}^P + F_{exc.}^M\right]_{6N\times 1} \end{aligned} \tag{2.16}$$

where $M$ and $A$ are the structural mass and added mass matrices, respectively, of the tunnel tubes, horizontal bracings and vertical columns. $m$ and $a(\infty)$ are the structural mass and added mass matrices of the floating pontoons at an infinite oscillation frequency. $C$ is the structural damping matrix. $\ddot{y}(t)$, $\dot{y}(t)$ and $y(t)$ are the structural acceleration, velocity and displacement, respectively. $H(t)$ is the retardation function representing the wave memory effect. $K$ and $k$ denote the structural stiffness of the tunnel tubes and hydrostatic restoring coefficient of the pontoons, respectively. $F_{exc.}^P$ is the excitation force which includes the first-order wave force, as well as the second-order mean and slowly varying drift forces on the pontoons.

$$F_{exc.}^P = F_j^1(t) + F_j^2(t) \tag{2.17}$$

The Newman assumption is adopted here for the calculation of the difference-frequency forces instead of using the full QTF. The generation of the first- and second-order wave forces in an irregular wave field has been addressed in the previous section. The viscous forces on the pontoons are neglected in this study.

$F^M_{exc.}$ is the is the sum of the viscous and Froude-Krylov forces on the tunnel tubes, bracings and columns based on the Morison equation. The forces per unit length are given by the following expression,

$$dF^M_{exc.} = \frac{1}{2}\rho C_D D\left(u - \dot{y}\right)\left|u - \dot{y}\right| dl + \rho C_M \frac{\pi D^2}{4}\dot{u}dl - \rho\left(C_M - 1\right)\frac{\pi D^2}{4}\ddot{y}dl \tag{2.18}$$

where $C_D$ and $C_M$ are the drag and inertial coefficients, which are set to 1.2 and 2.0, respectively, at a Reynolds number of approximately $10^7$ based on the guidance of DNV [32]; $D$ is the diameter of the corresponding structure; and $u$ and $\dot{u}$ are the water particle velocity and acceleration respectively, due to the wave at the submergence. The third term in Eq.2.18 is the added mass force that appears on the left-hand side in Eq.2.16 where $A = \rho\left(C_M - 1\right)\frac{\pi D^2}{4}dl$.

The above discussion provides a brief overview of the theoretical background for hydroelastic analysis of an SFT in a wave field, considering the first- and second-order wave forces and the influence of long- and short-crested waves. For a fully submerged structure, the current- and wave-induced VIV (as $KC$ is larger a critical value) is a different phenomenon and needs to be treated in a different manner. While, VIV often is treated as a phenomenon which should be avoided by satisfying certain criteria for the so-called reduced velocity. The aim in this thesis is to address both this traditional approach as well as introduce a time domain analysis of VIV-induced response. Moreover, previous studies have mainly focused on a single cylinder. A brief review of that is made in the following, and the differences between the flow around a single cylinder and twin cylinders will be emphasized to demonstrate the need for a more refined analysis of twin cylinders in the SFT design.

## 2.2 VIV for a single rigid cylinder

### 2.2.1 Flow around a circular cylinder

The basic understanding of the flow around a cylinder summarized in this section is based on the book by Sumer and Fredose [33]. Consider a smooth fixed circular cylinder in a steady flow, as shown in Fig. 2.1.

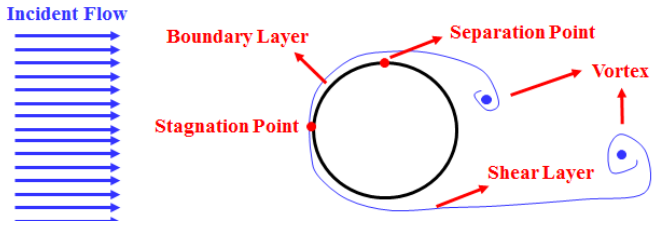


*Figure 2.1: Steady flow around a circular cylinder*

The flow, which is typically regarded as inviscid and irrational, is not affected by the cylinder at positions far away from it. On the surface of the cylinder, the no-slip condition must be satisfied at all times, which means that the flow velocity is zero. This causes the formation of a stagnation point and a thin boundary layer, characterized by a large velocity gradient in the radial direction. When the flow travels from the stagnation point to downstream of the cylinder, it will separate from the cylinder surface at a point and further induce a shear layer in the wake. Vorticity in the shear layer builds up to form a vortex. The Reynolds number, defined as the ratio between the inertial and viscous forces, is widely used to describe this phenomenon:

$$R_e = \frac{UD}{\nu} \tag{2.19}$$

where $U$ is the flow velocity, $D$ is the cylinder diameter, and $\nu$ is the kinematic viscosity of the fluid. When $R_e \leq 5$, no separation occurs, and the flow is attached to the cylinder surface. A fixed pair of symmetric vortices is observed in the wake when the Reynolds number is in the range of 5-40. When $R_e > 40$ , the larger vortex in the wake of the cylinder starts to be convected downstream by the flow, and a new vortex starts to form in its position. The previously smaller vortex eventually grows larger, drawing the new vortex across the wake [34]. This alternating vortex shedding gives rise to two rows of vortices, often referred to as a Karman vortex street. The features of the street and the boundary layer are strongly affected by the Reynolds number. When $40 < R_e < 200$ , both are laminar, which means that the vortex shedding is correlated along the length of the cylinder [35]. When $R_e$ reaches 300, the wake becomes turbulent. For $300 < R_e < 3 \times 10^5$ , named the subcritical region, the wake is completely turbulent, and the boundary layer starts to become turbulent. The vortex shedding is 3-dimensional, and the correlation length is typically approximately 3-10$D$ [29, 36, 37]. As $R_e$ continues to increase, 3 more

regimes are observed: 'critical' ($3 \times 10^5 < R_e < 3.5 \times 10^5$ ), 'supercritical' ($3.5 \times 10^5 < R_e < 1.5 \times 10^6$ ) and 'transcritical' ($R_e > 4.5 \times 10^6$ ). In the critical regime, the boundary layer becomes turbulent at one of the separation points of the cylinder, resulting in an asymmetric wake flow. The boundary layer separations are turbulent on both sides of the cylinder when $R_e$ is in the supercritical regime. The transition from laminar to turbulent occurs somewhere between the stagnation point and the separation. The boundary layer reaches total turbulence in the transcritical regime.

The above discussion has shown that vortex shedding will occur behind a cylinder once the Reynolds number is larger than 40 and that its features are strongly related to $R_e$, implying that the undisturbed flow velocity and the cylinder diameter are important for determining the vortex shedding mode (especially the frequency). The Strouhal number has been proposed to express the relation between these two parameters and the vortex shedding frequency $f_V$ [38]:

$$S_t = \frac{f_v D}{U} \tag{2.20}$$

There is a widely used result of Eq. 2.20 for the vortex shedding frequency of a fixed circular cylinder with a given diameter and flow velocity. Although $S_t$ varies with the Reynolds number and the surface roughness of the cylinder, $S_t = 0.2$ is generally reasonable in the subcritical regime [39]. For a smooth cylinder in the critical or supercritical regime, $S_t$ increases to approximately 0.45, while it subsequently drops to 0.25-0.3 as the Reynolds number continues to increase into the transcritical range. Typically, the vortex shedding frequency is consistent with a wideband spectrum that does not have a well-defined dominating frequency but instead may consist of several frequency components, except in certain cases in the subcritical regime [40]. In the following study, only vortex-related findings stemming from experiments in the subcritical regime are used in practical circumstances which could provide a good reference for the VIV features of an SFT and their effects on the dynamic responses.

### 2.2.2 Vortex-induced force on a single cylinder

In the process of vortex growth, the vorticity gives rise to an extra local velocity in the direction opposite to the flow, simultaneously reducing the local flow velocity and increasing the pressure [37]. The vortex-influenced pressure distribution generates two periodic forces in the IL and CF directions, termed the drag and lift forces, respectively. The asymmetric pressure distribution in the upstream and downstream regions of the cylinder creates

a drag force, as shown in Fig. 2.2. The force per unit length can be normalized as: $C_D = \frac{F_y}{\frac{1}{2}\rho D U^2}$ where $C_D$ is the drag coefficient, and $F_y$ denotes the corresponding drag force, and $y$ represents the inline direction. $\rho$ is the fluid density. $U$ is the undisturbed flow velocity. $C_D$ consists of two terms, namely, the mean and fluctuating drag coefficients. The former always exists regardless of the vortex conditions, and it typically has a value of 1.2 in the subcritical regime and experiences a significant decrease when $R_e$ is in the critical regime [41]. The separation point moving to the rear of the cylinder is the reason for this reduction, which is also referred to as the drag crisis. The latter term stems from the vortex-induced asymmetric pressure distribution, but the oscillation frequency is $2f_v$ , which is twice the vortex shedding frequency. The fluctuating term is much smaller than the mean term.

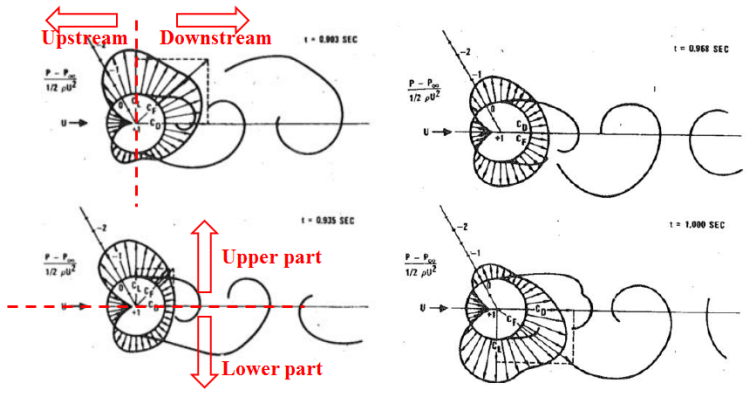


*Figure 2.2: Pressure distribution around a circular cylinder [37].*

For the CF lift force, which can be normalized as $C_L = \frac{F_z}{\frac{1}{2}\rho D U^2}$, $z$ represents the crossflow direction, the lift coefficient $C_L$ contains only a fluctuating term since it stems from the asymmetric velocity (pressure) distribution between the upper and lower parts of the cylinder, as shown in Fig. 2.2. It oscillates with the vortex shedding frequency $f_v$ and can induce a vibration in the CF direction. The vibration will be significantly amplified when $f_v$ is close to the natural frequency of the structure. It should be noted here that the surface roughness of the cylinder is another important factor affecting the coefficients discussed above; however, it will not be considered in this study.

### 2.2.3 Main features of VIV of a single cylinder observed from self-oscillation tests

The periodic lift force can exhibit a high-frequency CF vibration, i.e., VIV, when the structure is in a strong current. The features of this vibration, such as amplitude and frequency, strongly depend on the difference between the lift force frequency and the natural frequency. When this difference is small or near zero, a severe vibration can be observed; otherwise, the structure will remain static in the CF direction [42–44]. An effective method of measuring the significance of the VIV is necessary, but such a procedure must start from a sufficient understanding of the phenomenon. An elastically supported rigid cylinder with only one degree of freedom (DOF), as shown in Fig. 2.3 [45–47], is a widely used model for gaining knowledge of purely CF VIVs. In this system, the natural frequency ($f_n$) of the single DOF is determined by the spring stiffness $k$, the cylinder mass $m$, and the potential added mass force ($m_a = C_a m_d$, where $m_d$ is the displaced fluid mass and $C_a$ is the potential added mass coefficient, which is equal to 1 for a circular cylinder [48, 49]).

$$f_n = \frac{1}{2\pi}\sqrt{\frac{k}{m + m_a}} \tag{2.21}$$

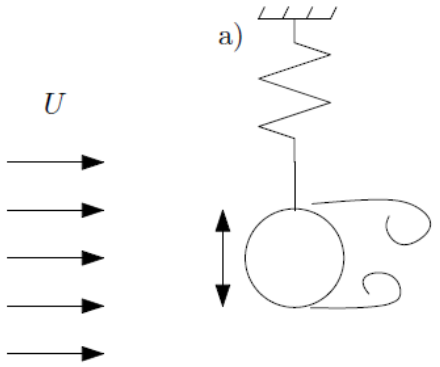


*Figure 2.3: Typical self-oscillation test in CF direction.*

The flow velocity $U$ gradually increases from zero. Initially, there are weak vortices in the wake flow, and the shedding frequency is far from the natural frequency; consequently, the cylinder oscillates with a small amplitude or remains static. As the flow velocity increases to a critical threshold, the vortex shedding synchronizes with the free vibration, resulting in

a significant vibration, and an energy balance between the flow force and structural damping is simultaneously achieved. In VIV analysis, this phenomenon is referred to as lock-in [33, 50–52]. The reduced velocity has been proposed to assess the likelihood of lock-in in VIV analysis [53, 54]:

$$U_r = \frac{U}{f_n D} \tag{2.22}$$

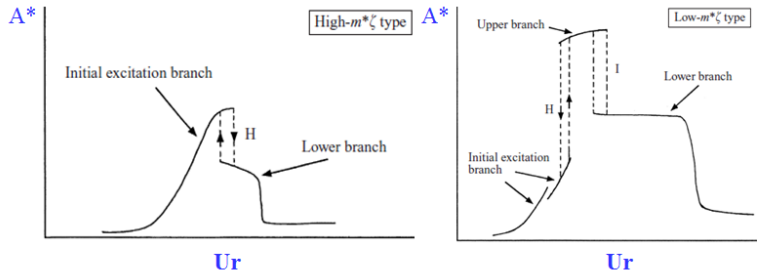


*Figure 2.4: Relation between response amplitude and reduced velocity with mass-damping ratios [54].*

Fig. 2.4 shows the critical range of $U_r$. Within this range, a significant response amplitude is observed at approximately $1D$, whereas outside of this range, the amplitude is very small. Typical range of $3 < U_r < 8$ is generally looked as VIV locking-in range. The dynamic motion of the cylinder under VIV conditions could further be described by

$$\begin{cases} m\ddot{z} + c\dot{z} + kz = F_L \\ z = z_0 \sin(\omega t) \\ F_L = F_z \sin(\omega t + \varphi) \end{cases} \tag{2.23}$$

where, $z_0$ and $F_z$ are the amplitudes of the VIV response and the CF lift force, respectively. $\omega$ is the lift frequency, which is the same as the vibration frequency. $\varphi$ is the initial phase difference between the cylinder vibration and lift force. For a given structure, these parameters describe a purely 2-dimensional CF VIV. Govardhan and Williamson [54] found that the phase difference is either 0 or $\pi$ for a stable VIV and that the lift force amplitude $F_z$ varies with $U_r$ and reaches its maximum coincidently with the maximum response amplitude.

In addition to the flow parameters, certain features of the structure, including the mass ratio and damping ratio, also strongly affect the VIV

features. Structures with different mass ratios ($m^* = \frac{m}{\frac{\pi}{4}D^2\rho l}$, the ratio between the mass of the structure and the mass of the displaced fluid) have different amplitude branches, as shown in Fig. 2.4. Specifically, for a low mass ratio, the response amplitude consists of three branches, namely, the 'initial', 'upper' and 'lower' branches, whereas the second branch disappears for a high mass ratio. The vortex mode remains constant within each branch but changes from '2S' to '2P' from the initial to the upper branch or from the initial to the lower branch, and the oscillation frequency $\omega$ and phase difference $\varphi$ change at the same time [54,55]. Moreover, $m^*$ also determines the threshold for the lower branch; ideally, the lower branch will never terminate if the mass ratio is equal to 0.54 [54]. Another important parameter found in self-oscillation tests is the combined mass-damping parameter $m^*\zeta$, where $\zeta$ is the structural damping ratio [56–60]. The maximum amplitude of the vibration has been found to mainly depend on $m^*\zeta$ for a range of conditions. This dependency is commonly displayed in a "Griffin plot" [61,62]. A critical review of the Griffin plot has been given by Willianson and Govardhan [42].

## 2.3 VIV prediction for a flexible pipe in current

The task of VIV prediction consists of two steps: first, obtaining the hydrodynamic forces acting on the given structure, and second, computing the structure's response to the hydrodynamic loads, considering the interaction between the hydrodynamic forces and the structural response.

### 2.3.1 Computational fluid dynamics method

The computational fluid dynamics (CFD) method is a suitable choice for accomplishing both steps simultaneously; a typical result is shown in Fig. 2.5.

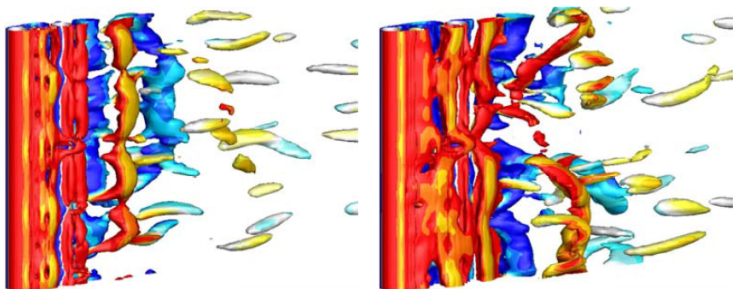

*Figure 2.5: Typical CFD result of tandem two flexible cylinders [63].*

The instantaneous fluid forces can be obtained by integrating the fluid pressure along the cylinder surface. The fluid velocity field is described by the Navier-Stokes (NS) equation, which is essentially Newton's second law for a fluid particle [64]. The flow field around the structure can be obtained through a combination of the NS equation and mass conservation. Researchers have proposed several numerical methods for discretizing the fluid domain and modeling turbulence. The finite-volume method is the most popular discretization method, while the available turbulence models include the Reynolds-averaged Navier-Stokes (RANS) [65], large eddy simulation (LES) (LES) [66, 67] and detached eddy simulation (DES) [68, 69]. Recently, a method for solving the NS equation directly (DNS) has been proposed as a result of considerable advancements in high-performance computing (HPC) [70, 71], This method is more accurate than the former three because it requires no assumption on the turbulence stress. However, the high computational cost limit the practical usage of all of these methods

Semiempirical methods are widely used instead of CFD because of their high simulation efficiency, and they can provide reasonable predictions and references for structural design. In these methods, the hydrodynamic forces are obtained from semiempirical equations and model tests (force coefficients), neglecting the flow velocity and pressure calculations.

### 2.3.2 Hydrodynamic coefficients in the semi-empirical approach

In the semiempirical approach, the amplitude of CF lift force is simplified as a product of the fluid density, the lift coefficient, the cylinder diameter and the square of the flow velocity:

$$F_L = \frac{1}{2}\rho C_L D U^2 \sin(\omega t + \varphi) \tag{2.24}$$

For a given case, the lift coefficient is the only challenging factor for the fluid force calculation. Bishop and Hassan firstly measured and recorded the fluid forces on a circular cylinder oscillating in the CF direction with various (oscillation) amplitudes and frequencies [72]. They found that when the cylinder oscillated with a frequency far from the Strouhal frequency, the lift force frequency was dominated by the Strouhal frequency, while when the cylinder oscillated with a frequency near the Strouhal frequency, the lift force was synchronized with the cylinder motion. This phenomenon reveals that the lift force may have two components, referred to as the Strouhal frequency and the cylinder motion frequency, either of which could

be dominant depending on the relation between them. In addition, the lift force amplitude is also related to the oscillation frequency and amplitude.

To provide suitable lift coefficients with a possible coupling with vibration amplitude and frequency for VIV prediction, a series of forced oscillations tests have been conducted [73–76] The cylinder was driven to oscillate with a series of given amplitudes and frequencies, and the CF lift force was recorded simultaneously. The cylinder oscillation was sinusoidal in time, similar to the observed results of self-oscillation tests:

$$z = z_0 \sin(\omega t) \tag{2.25}$$

The vibration velocity and acceleration can be expressed as,

$$\begin{cases} \dot{z} = \omega z_0 \cos(\omega t) \\ \ddot{z} = -\omega^2 z_0 \sin(\omega t) \end{cases} \tag{2.26}$$

The observed lift force per unit length can be decomposed as follows:

$$\begin{aligned} F_L(t) &= F_z \sin(\omega t + \varphi) \\ &= F_z \sin(\omega t)\cos(\varphi) + F_z \cos(\omega t)\sin(\varphi) \\ &= \tfrac{F_z \sin(\varphi)}{\omega z_0}\dot{z} + \tfrac{F_z \cos(\varphi)}{-\omega^2 z_0}\ddot{z} \end{aligned} \tag{2.27}$$

$$\begin{cases} \frac{F_z \sin(\varphi)}{\omega z_0}\dot{z} = \frac{1}{2}\rho D U^2 C_{Le}\frac{\dot{z}}{\omega z_0} \\ \frac{F_z \cos(\varphi)}{-\omega^2 z_0}\ddot{z} = \frac{\rho D^2 \pi}{4} C_{La}\ddot{z} \end{cases} \tag{2.28}$$

where $C_{Le}$ and $C_{La}$ denote the excitation force and added mass force coefficients, respectively. The former is related to the energy transfer between the fluid and the cylinder. A positive value indicates that energy is transferred from the fluid to the cylinder, whereas a negative value indicates that energy is transferred from the cylinder to the fluid, meaning that hydrodynamic damping occurs. The latter (added mass) is important in the eigenvalue analysis, which will be addressed in the 'VIV prediction in frequency domain' section.

Widely used excitation and added mass coefficients are presented as functions of the amplitude ratio $A/D$ and the nondimensional frequency $\hat{f} = \frac{fD}{U}$ . A typical result obtained by Gopalkrishnan [73] is shown in Fig. 2.6.

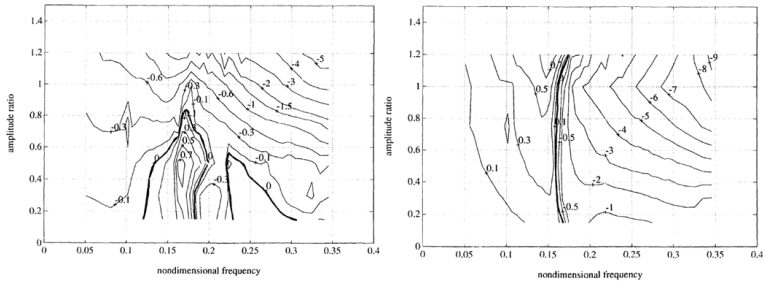


*Figure 2.6: Excitation and added mass coefficient obtained by Gopalkrishnan [73]*

Among the contours of the excitation coefficient, positive values in the range of $0.12 < \hat{f} < 0.2$ and low amplitudes correspond to the synchronization results given by Bishop. The bold line in the figure represents the 'zero-excitation coefficient', and the corresponding coupled amplitudes and frequencies could be the ideal self-oscillation test results (without structural damping). It should be mentioned here that the peak excitation coefficient is located at a frequency of $\hat{f} = 0.17$ rather than at the Strouhal frequency of 0.2, meaning that the vortex shedding frequency under vibration conditions is different from that under stationary conditions. Many researchers believe that the frequency- and amplitude-dependent added mass is the reason for this difference.

### 2.3.3 VIV prediction in the frequency domain

Based on the VIV observations from self-oscillation tests and the force coefficients from forced-oscillation tests, two typical semiempirical prediction methods have been proposed, namely, the frequency-domain method and the time-domain method. The former has been widely accepted in offshore engineering and is implemented in software such as VIVA [77], SHEAR7 [78] and VIVANA [79]. Although there are differences among various frequency-domain (FD) implementations, the main procedures are identical. A short discussion about the implementation in VIVANA is presented here. The slender structure is modeled using beam elements with structural damping based on the Rayleigh damping model. The analysis proceeds via the following steps:

1. Static analysis

2. Eigenvalue analysis in still water, with frequency-independent added mass

3. Identification of possible excitation frequencies considering frequency-dependent added mass via an iterative method

4. Determination of excitation and damping zones

5. Calculation of cross-flow response by convergence of the energy dissipation and import (The energy transferred from the fluid to the structure in the excitation zone is equal to the energy dissipation in the damping zone).

In this procedure, nonlinear effects, such as multi-frequency coupling, time-dependent boundary conditions and varying axial forces, must be neglected in order to maintain a linear approach: an application of superposition principle.

### 2.3.4 VIV prediction in the time domain

Recently, many time-domain VIV prediction methods have been proposed to compensate for the limitations of the frequency-domain method. In such methods, the key challenge is the modeling of the instantaneous lift forces on each section. Researchers have presented various models in their studies. Zhang et al [80]. defined the lift force per unit length at a given position in the excitation region as

$$\begin{aligned} F_L(x,t) &= \sum_{j=m}^{n} F_{j,L}(x,t) \\ &= \sum_{j=m}^{n} \tfrac{1}{2}\rho D[U(x)]^2 C_{L-e,j}\left[A_j(x)/D, f_j^*(x)\right]\cos\left(\omega_{n,j}(t)\,t + \varphi_j(x)\right) \end{aligned} \tag{2.29}$$

were, $j$ denotes the eigenmode that can be excited under VIV conditions. $\omega_{n,j}(t)\,t$ is the time-dependent eigenfrequency, by which the effect of the time-varying axial force on the structural stiffness can be considered. $C_{L,j}\left[A_j(x)/D, f_j^*(x)\right]$ denotes the excitation coefficient in terms of the response amplitude and frequency. The authors set the initial phase angle $\varphi_j(x)$ to either 0 or $\pi$ depending on the excited mode shape at point $x$, as shown in Fig. 2.7. The authors suggested that synchronization between the force and the response would be achieved when the VIV response is stable, meaning that the phase difference between the excitation force and the response velocity is zero. In the damping zone, Vagugopal damping model was used to calculate the hydrodyanmic damping force [81]. In this time-domain method, a time-varying pretension on the slender structure is considered

by updating the excitation frequencies, regions and coefficients in each iteration, and nonlinear effects are partially addressed [80]. The authors' understanding of the initial phase angle provides a reasonable reference for the VIV analysis of an SFT.

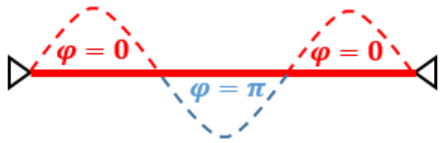


*Figure 2.7: Initial phase angle of the lift force based on the mode shape*

The time-domain method discussed above is, in some sense, an extension of the frequency-domain method since solving the eigenvalue problem is a necessary step in each iteration. In contrast, Thorsen et al. proposed an alternative method [82–84], in which the eigenvalue problem is not directly solved and the structure is no longer divided into 'excitation' and 'damping' regions. These authors modeled the hydrodynamic force in the CF direction as

$$F_{L,0} = \frac{1}{2}\rho D U^2 C_L \cos\phi_l - \frac{1}{2}\rho D C_1 U \dot{z} - \frac{1}{2}\rho D C_2 |\dot{z}| \dot{z} - \frac{\rho D^2 \pi}{4} C_a \ddot{z} \quad (2.30)$$

where $D$, $\rho$, and $U$ denote the cylinder diameter, fluid density and flow velocity, respectively. $\dot{z}$ and $\ddot{z}$ are the crossflow velocity and acceleration of the cylinder. $\phi_l$ is the instantaneous phase of the lift force. $C_1$ and $C_2$ are the constant in equivalent damping force. $C_a$ is the added mass coefficient. The second and third terms in the equation are the damping forces, which are the same as those used for the 'damping' region in the frequency-domain method. The last term is the potential added mass force, which typically appears on the left-hand side of the dynamic equation. $C_L$ is the lift coefficient, which is calculated based on the excitation coefficient. In the calculation process, the damping force is also considered, as the actual excitation coefficient is a result of both the power input from the lift force and the power output due to damping. A typical result for the lift coefficient is shown in Fig. 2.8.

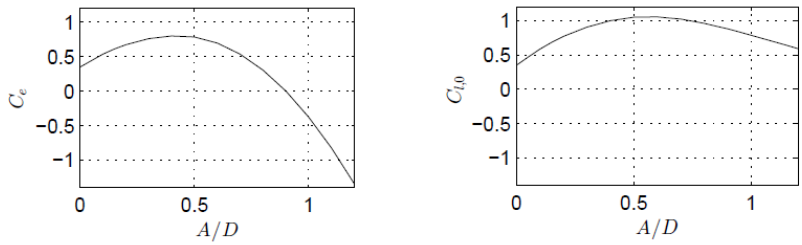


*Figure 2.8: Excitation coefficient and lift coefficient for a given frequency* $\hat{f} = 0.17$ *[82].*

It should be mentioned here that the sensitivity of the lift coefficient to the response amplitude is negligible compared with the sensitivity of the excitation coefficient. Thorsen et al. [85] treat the lift coefficient as an amplitude-independent constant in the time-domain prediction process for a given current state, and it is considered to be related only to the Reynolds number in their recent study.

Many researchers have proposed time-domain prediction methods that have specific advantages for certain special cases. Lu et al. [86] proposed an efficient time-domain prediction method for unsteady flows. In this method, a period-identification criterion is proposed to divide the entire vibration process into excitation and damping periods for each possible excited mode. The vibrations in each period are obtained individually to improve the simulation efficiency and convergence speed. Ulveseter [84, 87] extended Thorsen's method to purely IL vibrations to complete the method and make it suitable for fatigue damage calculation in the IL direction. Maincon [88, 89] proposed an innovative method in which a neural network was trained to convert the flow velocity into the hydrodynamic force. The concept of a wake oscillator has also been considered as a basis for prediction [90].

Time-domain prediction has attracted researchers' attention for a long time. Most researchers have proposed and verified their own methods, all of which are founded on the basic understanding of the VIV features obtained from self-oscillation tests, such as the critical range of the reduced velocity or nondimensional frequency used for lock-in assessment as well as sinusoidal time series of vibrations and lift forces.

For the VIV study of an SFT, little information is available, especially for rigidly connected tandem twin cylinders; some researches on the wake pattern of such a structure under static conditions has been reported [91–94].

## 2.4 VIV in oscillatory flow

For a slender structure, such as an SFT, VIV could also be excited by waves with a long period, as long as the $KC$ number ($KC = \frac{U_M T}{D}$) is larger than the critical value [95, 96].

Some researchers studied the VIV features in an oscillatory flow numerically, but the accuracy has not yet been examined [97,98]. A series of model tests have been conducted by Wang, Ren and Fu et al. [99–101], and they observed that the VIV in an oscillatory flow is quite different from that in a steady flow. The occurrence of intermittent VIV is the most notable phenomenon, which reveals a time varying response, as shown in Fig. 2.9. A larger number of vibration cycles and amplitude modulation are observed in the case with a larger $KC$. Mode transition is another important feature, when the reduced velocity is sufficiently large as shown in Fig. 2.10. Moreover, the well known '8-shaped' inline and crossflow VIV trajectory could be changed at small $KC$ as shown in Fig. 2.11.

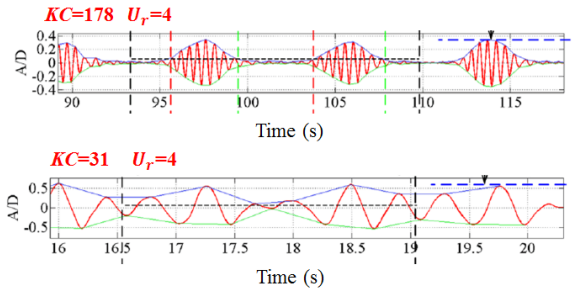


*Figure 2.9: Intermittent VIV in an oscillatory flow [95].*

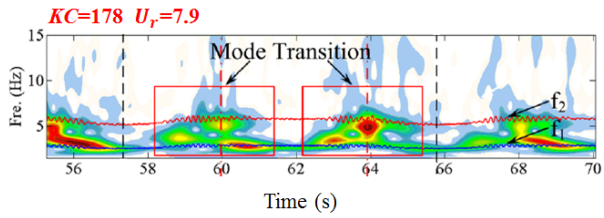


*Figure 2.10: Mode transition in an oscillatory flow [95].*

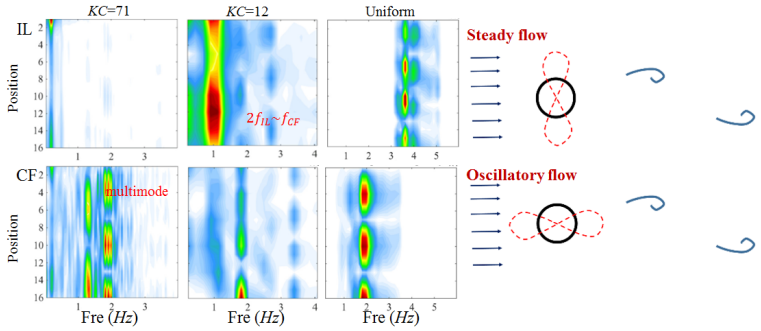


*Figure 2.11: VIV trajectory in an oscillatory flow [102].*

For the SFT both waves and pontoon motions could induce oscillatory flow to the tunnel tubes. For the wave-induced oscillatory flow, the $KC$ ($KC = \frac{\pi H}{D}$, where $H$ is the wave height, with $H = 1.86 \times H_s$ [32]) is about 1. For the pontoon motion-induced oscillatory flow, the $KC$ ($KC = \frac{2\pi A}{D}$, where $A$ is the lateral motion amplitude of the pontoons, $A$=1.2 $m$) is about 0.6. Hence, it dose not seem that the oscillatory flow-induced VIV is significant for the SFT, but the coupled response with the wave-induced hydroelasticity, and the difference between it and the steady flow-induced VIV should be further investigated.

Moreover, in practice the SFT is subjected to an irregular wave condition, which means that the oscillatory flow is not harmonic. So far the potential VIV in such an irregular oscillatory flow, has not been studied.

The investigation of VIV features of SFTs in an oscillatory flow is outside the scope of this thesis, but they should be investigated in future studies.

## 2.5 VIV of tandem twin cylinders

Few studies on VIV of tandem twin cylinders were available, while most researches have been focused on the fixed twin cylinders including the spacing distance effects on the flow pattern, Strouhal frequency and force coefficients. This part starts from a review of the stationary results followed by the VIV studies.

When the two cylinders are arranged in an IL or tandem configuration, the downstream cylinder will be shielded by the upstream cylinder, meaning that its incoming flow conditions are modified by the upstream cylinder; meanwhile, it also interferes with the wake dynamics and vortex formation region of the upstream cylinder. This interaction between the two cylinders causes the upstream cylinder to behave as a 'turbulence

generator', whereas the downstream cylinder can be regarded as a 'drag reduction device' or 'wake stabilizer' [103]. Many experimental studies of tandem cylinders under steady flow conditions have been conducted, where the effects of heat transfer [104–106] and mass transfer [107] have been the main considerations. There have also been many numerical studies of the flow around tandem two cylinders, primarily at low Reynolds numbers, e.g., for $R_e$=100 [108], $R_e$=200 [109], $R_e$=100-1000 [110], although some studies have also focused on higher Reynolds numbers [111].

### 2.5.1 Flow pattern

Pioneering researchers have found that the flow around tandem two circular cylinders is sensitive to both the Reynolds number and the spacing ratio (defined as the spacing distance divided by the cylinder diameter,$\lambda = L/D$, as shown in Fig. 2.12) [91, 94].

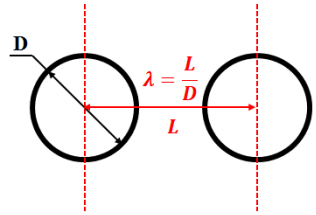


*Figure 2.12: Spacing ratio for tandem twin cylinders*

Related studies have identified eight different flow patterns for two tandem cylinders of equal diameter, as shown in Fig. 2.13. Following Zdravkovich's approach, researchers divided these flow patterns into three basic types by wake interference behavior [92, 112–114]:

- Single bluff body behavior, also referred to as the 'extended-body regime', at small $L/D$, where the two cylinders are sufficiently close to each other to act as if they are a single structure [92].
- Shear layer reattachment behavior, also referred to as the 'reattachment regime', at intermediate $L/D$, where the separated shear layers from the upstream cylinder reattach to the surface of the downstream cylinder and vortex formation may be observed in the gap area [115].
- Karman vortex shedding from each cylinder, also referred to as the 'co-shedding regime', at large $L/D$, where the two cylinders are sufficiently far away from each other to act as two independent single cylinders [116, 117].

The second regime can be subdivided into two basic flow regimes based on the behavior of the Strouhal number [93], the wake flow structure and the vortex dynamics [92], as shown in Fig. 2.14.

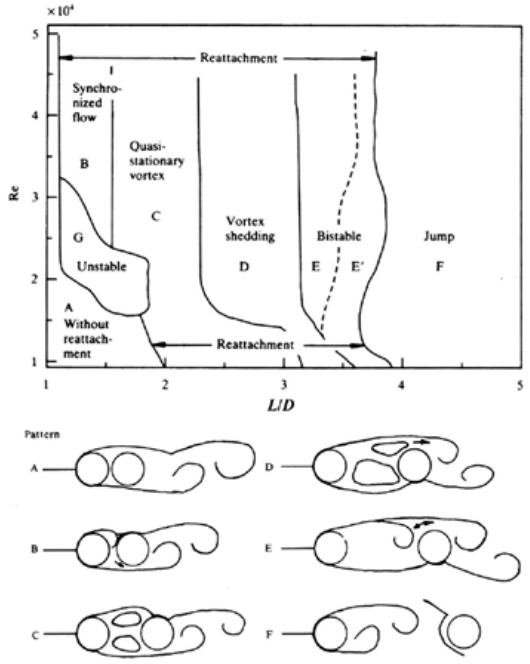


*Figure 2.13: Eight flow patterns identified by Igarashi [118]*

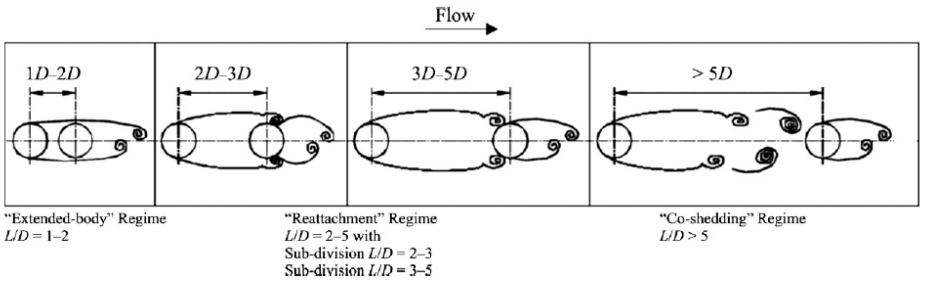


*Figure 2.14: Four regimes defined by Xu and Zhou [92]*

In the extended-body regime, typically corresponding to $1 < \lambda < 2$, the two cylinders are sufficiently close to each other to act as a single bluff body. The separated shear layers from the upstream cylinder are forced to enclose and wrap around the downstream cylinder, meaning that no

vortex shedding can be observed in the gap area [119–121]. Vortex formation behind the downstream cylinder can be observed, but the wake is narrower and the vortex street is more elongated compared with the case of a single cylinder [115].

In the reattachment regime, the vortices shed from the upstream cylinder will reattach to the downstream cylinder, with a reattachment point determined by the spacing ratio. At small $\lambda$, typically $2 < \lambda < 3$, reattachment often occurs on the downstream side of the downstream cylinder, and this phenomenon induces weak and small Karman vortices behind the downstream cylinder. At slightly larger $\lambda$, typically $3 < \lambda < 5$, reattachment occurs more often on the upstream side of the downstream cylinder. In this case, there is less effect on the Karman vortices behind the downstream cylinder [103, 111, 122, 123]. Numerical simulations have also revealed two main modes of fluid behavior [111]:

- Shared layers from the upstream cylinder symmetrically reattached to the downstream cylinder.

- Formation of a small vortex just upstream of the downstream cylinder, which is then entrained into the vortex shedding process of the downstream cylinder.

A complete vortex street can be observed only in the wake of the downstream cylinder, but the vortices appear different from those of a single cylinder, in addition to the different vortex formation and shedding mechanisms [115].

In the co-shedding regime, the downstream cylinder is located outside the vortex formation region of the upstream cylinder, and obvious vortex streets are observed behind both the upstream and downstream cylinders, meaning that they behave more like two single cylinders [92, 116]. The flow around the downstream cylinder is more complex since it experiences the periodic impingement of the shed vortex street from the upstream cylinder. The resulting vortex street of the downstream cylinder is larger but weaker than that in the extended-body and reattachment regimes. The vortices that comprise the vortex street weaken and dissipate more quickly, partially due to the vortex impingement process [92].

Many researchers have defined the ranges of the spacing ratio for each regime based on their own results; for example, the extended-body regime has been defined as corresponding to $1 < \lambda < 2$ [92] and to $1 < \lambda < 1.2 - 1.8$ [112]. However, the basic features of each regime are identical, and the spacing ratio strongly affects the flow around the cylinders when $\lambda < 5$.

### 2.5.2 Force coefficients and Strouhal number

In addition to the flow pattern, the hydraulic forces and vortex shedding frequency have also been studied. Typical results for the mean drag coefficient are shown in Fig. 2.15. For the upstream cylinder, the mean drag force is lower than that for a single cylinder in the extended-body and reattachment regimes. An obvious slow decrease is observed with increasing $L/D$ throughout the reattachment regime. A discontinuous jump then occurs for both cylinders as the flow transitions from the reattachment regime to the co-shedding regime. Subsequently, the relation between the drag force and the spacing distance is weak.

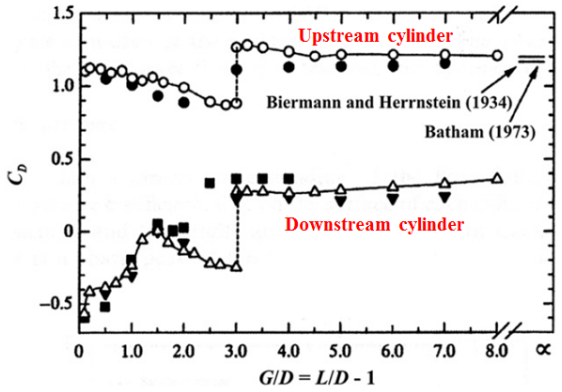


*Figure 2.15: Mean drag coefficient data for two tandem cylinders under CF conditions as a function of the spacing ratio at $R_e = 6.5 \times 10^4$; figure from [124].*

Previous researchers have also published Strouhal number data for tandem two cylinders with respect to the spacing ratio, and Fig. 2.16 shows typical results [93]. In general, most researchers believe that the two cylinders have the same Strouhal number at all spacing ratios. And it is slightly higher than that of a single cylinder but decreases rapidly with increasing $L/D$ when the cylinders are in the extended-body regime. The shorter vortex formation length when the cylinders are close to each other is the main reason for this phenomenon [125]. In the reattachment regime, $S_t$ decreases slowly as $L/D$ increases, and it is lower than that for a single cylinder. The stabilization of the flow field due to the splitter-plate function of the downstream cylinder is understood to be the main reason for this behavior. As the spacing distance continues to increase, the difference in $S_t$ between two cylinders and a single cylinder gradually disappears.

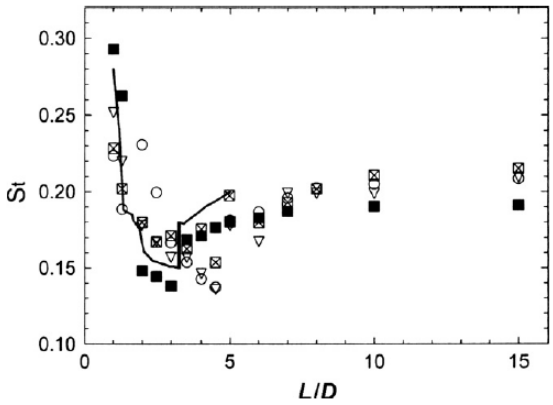


*Figure 2.16: Strouhal number data for tandem two cylinders in cross-flow as a function of spacing ratio, figure from [93].*

However, different findings have also been published. Two dominant frequencies have been reported for the case where the cylinders are configured at the boundary between the extended-body and reattachment regimes [94, 118]. The vortex shedding peaks in the power spectra have also been observed to be smaller and more wideband in nature in these regimes [126]. Moreover, studies have also reported a strong relation between $S_t$ and $R_e$. Complex behavior of $S_t$ with respect to $R_e$, including an extra $S_t$ and the results at a very high spacing ratio, has been summarized in a review [127].

Because of the complex flow pattern in the gap area and the strong relations with the spacing distance, flow velocity, etc., many of the phenomena related to the flow around two tandem cylinders remain unclear. These phenomena will affect the hydrodynamic forces on the cylinders in the stationary state. For free oscillation conditions, the problem is even more complicated. Few results are available on the interaction between the free oscillation and the flow patterns around tandem twin cylinders. The VIV phenomenon, as one of the most critical interactions for the load design of an SFT, should be addressed first.

### 2.5.3 VIV response

For the VIV features of tandem two cylinders, from oil and gas riser design problem, previous research paid more attention on the two unconnected cylinders, meaning that the two cylinders can oscillate individually. King and Johns [128] investigated the VIV characteristics of a cylinder placed downstream of another cylinder for a spacing ratio ranging from 3.5 to

7 and observed that synchronization of the downstream cylinder vibration coincided with that of the upstream cylinder. Bokaian and Geoola, Ruscheweyh [129–131] observed the vibration of a cylinder in the wake of the upstream cylinder and referred to the vibration as "wake galloping". Kim et al. [132], presented the results of an investigation on the flow-induced vibration characteristics of two circular cylinders in a tandem arrangement. The interactions of the up- and downstream cylinders on VIV were revealed in three different experimental conditions. Huera-Huarte and Bearman [133] conducted experiments of tandem twin cylinders with spacing ratio ranging from 2-4. In the range of 2-2.5, the upstream cylinder experienced a larger VIV than the downstream cylinder. The downstream cylinder displayed the feature of galloping vibration as the ratio ranging from 3 to 4. Larger spacing ratio 4-8 was further studied by Huera-Huarte and Gharib [134]. They found that upstream cylinder presented VIV features similar as that of a single cylinder and the downstream cylinder experienced a large amplitude response when $U_r$ beyond the classical lock-in region. More recently, Bin Qin et al. [135] studied the vortex-excited and galloping vibrations of two tandem cylinders with respect to the flow velocity (by $U_r$ ranging from 3.8 to 47.8) and spacing distance (by spacing ratio ranging from 1.2 to 6.0). They grouped the spacing distance into 4 regimes based on the response amplitude and frequency.

For the VIV of two flexible cylinders in tandem configuration, Chen et al [136] presented results obtained by numerical simulations. They found that the vortex street was suppressed between the cylinders and there was a reattachment of the shear layers to the downstream cylinder when $\lambda = 3$. However, as $\lambda = 4$, a vortex street started to appear in the gap with intermittent reattachment of shear layers on the downstream cylinder surface. Wang et al. [63] further studied the VIV response features and Fig. 2.17 shows the typical results. They found that the lift coefficient of the downstream cylinder is more sensitive to the spacing ratio than that of the upstream cylinder. The response amplitude of the downstream cylinder is larger than that of the upstream cylinder at large reduced velocity. The correlation lengths of the two cylinders roughly follows that of an elastically mounted rigid cylinder. Based on the flow pattern, at a small spacing ratio, the presence of the downstream cylinder is found to suppress the three dimensionality of the upstream flow, resulting in large correlation lengths of the upstream cylinder, and the subsequent weak turbulence intensity and three-dimensionality of the upstream flow consequently lead to high spanwise correlation of the downstream cylinder. Only two regions (initial and upper, defined by the relation between the response amplitude and reduced velocity) are observed

for the downstream cylinder (with low mass ratio) as the spacing ratio is 5 , different from single cylinder with three regions (initial, upper and lower).

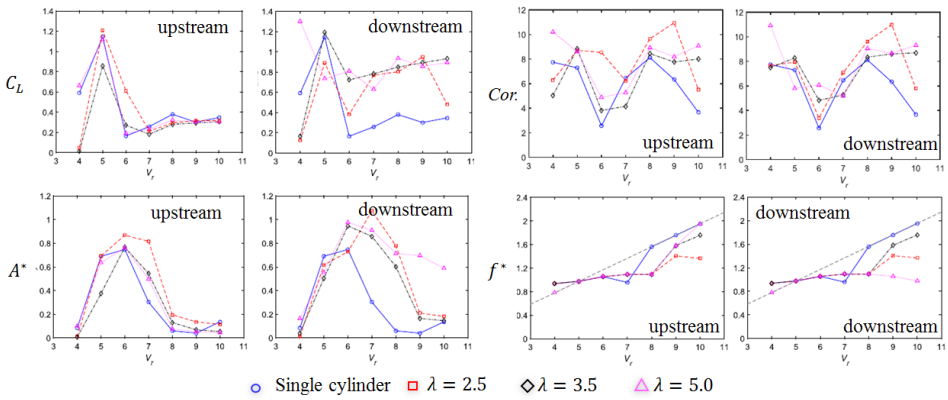


*Figure 2.17: VIV of two tandem flexible cylinders, lift coefficient, correlation length, response amplitude and frequency [63].*

Investigations of the VIV of rigidly connected tandem twin cylinders are scarce. In line with the available knowledge on single-cylinder VIV analysis, a series of self-oscillation tests are firstly needed to obtain a clear understanding of the effect of the spacing ratio on the VIV features and force coefficients.

# Chapter 3

# Experimental Study on a Twin-tube SFT Segment Model in Current

Self-oscillation experiment of a twin-tube SFT segment model with different spacing ratios in a towing tank is performed in the thesis. The model is designed as two rigidly connected cylinders in tandem arrangement. Details of the test apparatus, test matrix and data post-processing method will be introduced in the chapter.

## 3.1 Test set-up

The self-oscillation tests were conducted in the Marine Cybernetics Laboratory (MC-Lab) towing tank at Norwegian University of Science and Technology (NTNU), with a dimension of $40 \times 6.45 \times 1.5\ m$, as shown in Fig. 3.1. The maximum towing speed of the carriage is 2 $m/s$.

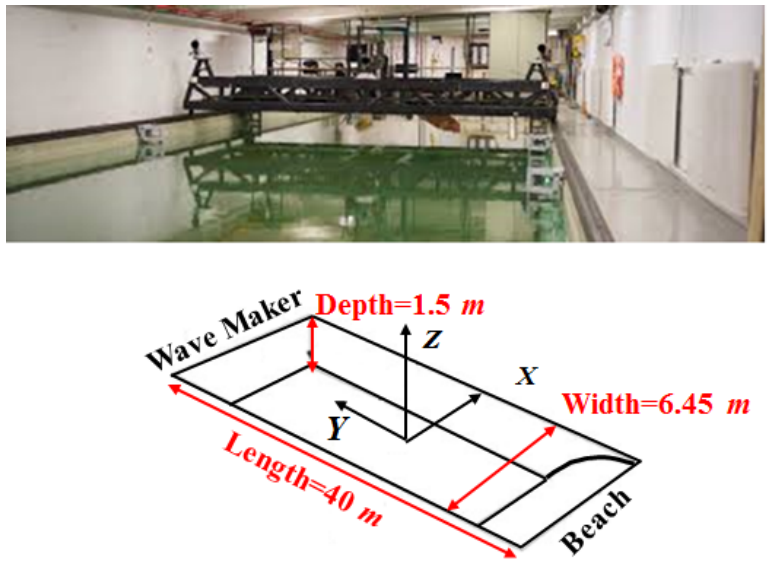


*Figure 3.1: MC-Lab towing tank at NTNU.*

### 3.1.1 Twin-tube SFT segment Model

The SFT segment model was constructed as a pair of aluminum circular cylinders in tandem arrangement with a length of 2.05 $m$ and a diameter of 0.1 $m$, as shown in Fig. 3.2. The horizontal bracings in the actual SFT were neglected, and the hydrodynamic damping and flow pattern influence due to them were also ignored. The center-to-center distance can be adjusted through the connection structures, shown in Fig. 3.3. The surface roughness of the two cylinders was measured at six random positions, as shown in Fig. 3.4, and the mean value is listed in Table 3.1. The mass of the cylinders and additional connection structures (oscillating simultaneously with the cylinders) were designed be equal to the displaced water mass to guarantee the mass ratio to be 1.0.

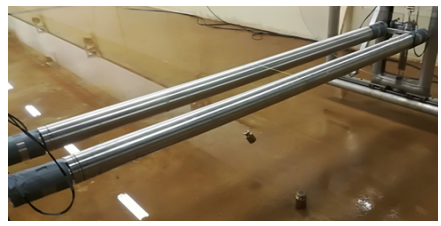

*Figure 3.2: Twin-tube SFT segment model in the self-oscillation tests.*

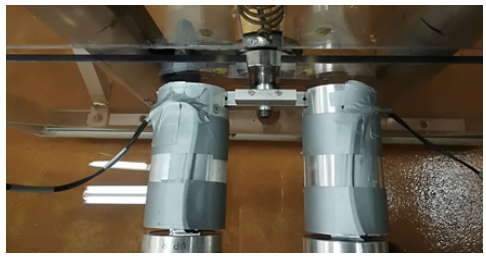

*Figure 3.3: Connection structure for adjusting the spacing distance.*

*Figure 3.4: Surface roughness measurement on the cylinder.*

*Table 3.1: Main parameters of the testing cylinder.*

| Parameter | Value | Units |
|---|---|---|
| Single cylinder mass ($m_0$) | 16.1 | $kg$ |
| Twin cylinder mass ($m$) | 32.2 | $kg$ |
| Roughness ratio ($k/D$) | $6 \times 10^{-6}$ | - |
| Aspect ratio ($l/D$) | 20 | - |
| Mass ratio ($m^*$) | 1 | - |

*where, mass ratio $m^*$ is defined as $m/\left(\rho\pi D^2 l/4\right)$. $D$ and $l$ are the cylinder diameter and length, respectively. $m$ is the mass of the oscillating system, including the cylinders, the sliders on the track, the connection structures between the twin cylinders and the sliders, the force sensors and the dummies.*

### 3.1.2 Test rig

The segment model was elastically mounted between two support frames which were suspended beneath the towing carriage, as shown in Figs. 3.5 and 3.6. Two groups of springs were equipped on the support frame to provide restoring forces for the model. A pair of low-friction tracks was

mounted on one side of each frame. Only VIV in CF direction was considered in the test. Calibration tests on the stiffness of the springs and the friction of the tracks are presented in Appendix A and B, respectively. A draw-wire displacement sensor and two single-component force sensors were installed at each end of the cylinders, as shown in Fig. 3.7. The oscillation motion in CF direction and the lift and drag forces acting on each cylinder were measured simultaneously and recorded in digital form with resolutions of $10^{-4}m$ and $0.01N$, respectively. The calibration of the sensors is also presented in Appendix A. Typical time series are listed in the Appendix C.

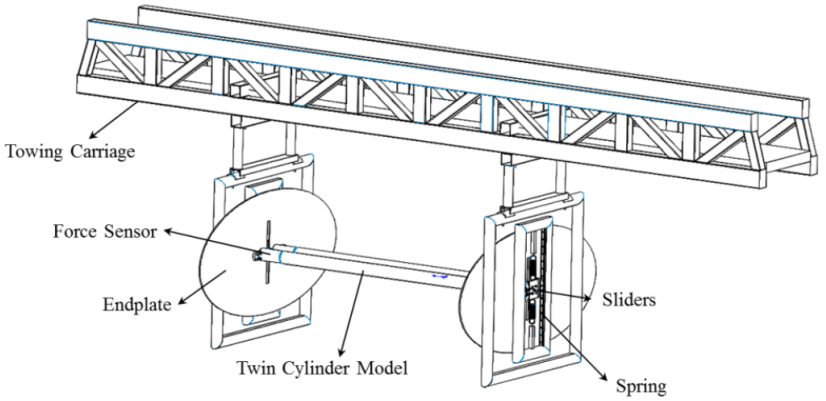


*Figure 3.5: Sketch of the test setup.*

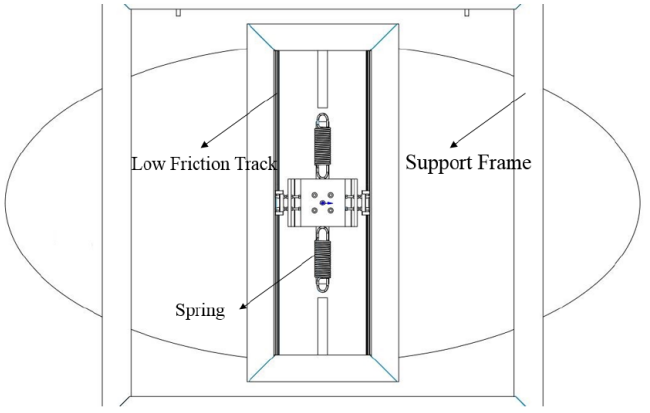


*Figure 3.6: Details of the track and springs arrangement.*

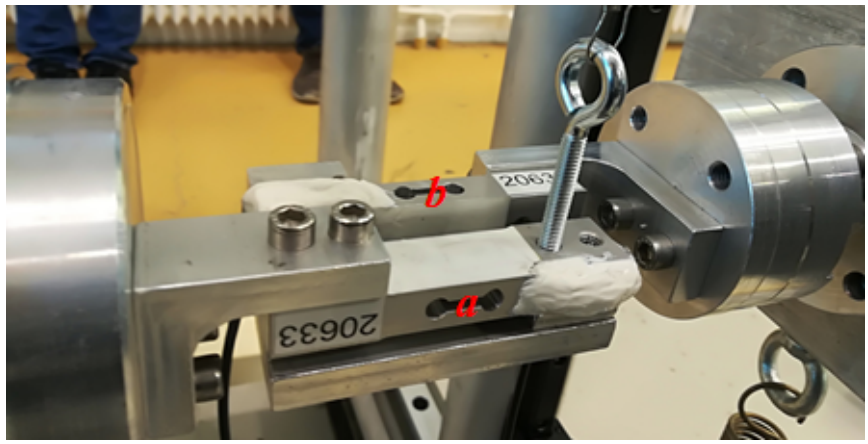


*Figure 3.7: Single-component force sensors at the end of the cylinder, (sensors (a) and (b) measure the CF lift force and the IL drag force, respectively).*

Free decay tests were first conducted in air and still water after the installation of the test setup to obtain the structural damping in air and the natural frequency in water. Fig. 3.8 and Fig. 3.9 show typical series from the corresponding decay tests. The natural frequency in still water is 1.004 Hz. The structural damping ratio in water $\zeta$ is written as $\zeta = \zeta_0 \Big/ \sqrt{(1 + m_A/m)}$. $m_A = C_A \rho D^2 l\pi/4$, which is found to be around 0.045. Here, $\zeta_0$ is the damping ratio in air and can be calculated by $\zeta_0 = \frac{1}{2n\pi} \ln\left(\frac{A_i}{A_{i+n}}\right)$ . $m_A$ is the added mass and can be written as $m_A = C_A \rho D^2 l\pi/4$. The assumption of added mass coefficient $C_A = 1$ is widely adopted in damping ratio normalization [54, 137]. The detailed test setup parameters are listed in Table 3.2.

*Table 3.2: Test setup parameters.*

| Parameter | Vaule | Unit |
|---|---|---|
| Structural damping ratio ($\zeta$) | 0.045 | - |
| Stiffness for single cylinder | 1270 | $N/m$ |
| Stiffness for twin cylinders | 2540 | $N/m$ |
| Natural frequency in still water ($f_N$) | 1 | $Hz$ |

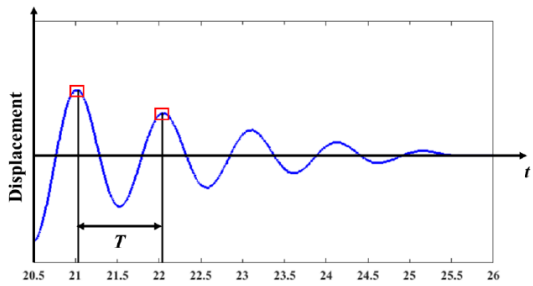


*Figure 3.8: Typical time series from a free decay test in the still water.*

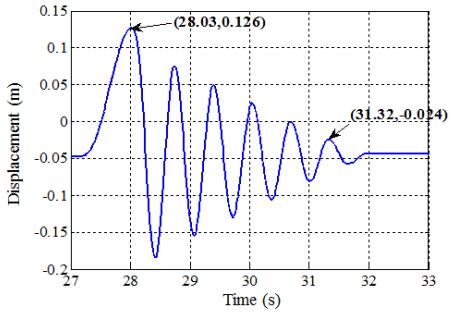


*Figure 3.9: Typical time series from a free decay test in the air.*

## 3.2 Test Matrix

In the self-oscillation tests, the varying parameters include the spacing ratio and submerged depth as well as the current velocity. The spacing ratio is defined as the center-to-center distance between the tandem twin cylinders divided by the model diameter, as shown in Fig. 3.10. The submerged depth is defined as the distance from the lower side of a cylinder to the free surface.

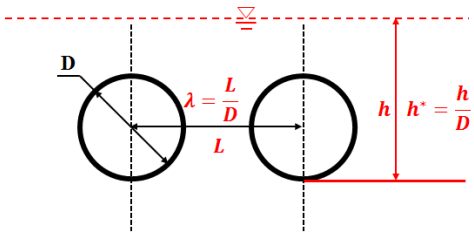


*Figure 3.10: Definition of the spacing and submergence ratios.*

During the experiments, the spacing ratio could be adjusted through the connecting apparatus, as shown in Fig. 3.11. To reveal the spacing ratio effect on the VIV features, experimental studies on a single cylinder and twin cylinders with spacing ratios ranging from 2 to 4 were conducted.

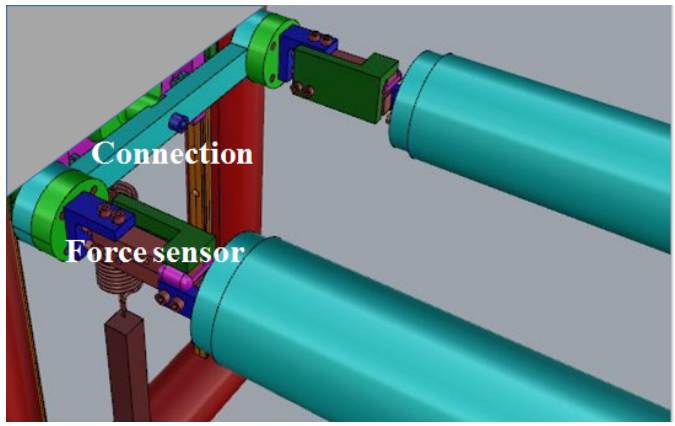


*Figure 3.11: Connecting apparatus.*

The first vertical eigenfrequency of the full-scale SFT is 0.044 $Hz$, and the maximum incident flow velocity can reach 2.2 $m/s$ [2,3], considering the surface current and wave-induced Stokes drift velocity. Hence, the maximum possible reduced velocity ($U_r = \frac{U}{f_n D}$) is 4.0. Moreover, previous researchers have reported that the largest VIV response for a single-cylinder system with a low mass ratio ($m^*$ ~1 as defined in Table 3.1) occurs at a reduced velocity of approximately 8 [54]. For these reasons, in the present tests, the range of the reduced velocity was varied from 2.0 to 9.0 to cover the possible reduced velocities of the floating tunnel in the fjord and the critical reduced velocity of a single cylinder. The detailed test matrix is shown in Table 3.3.

*Table 3.3: Test matrix.*

| Case | Towing velocity | Reduced velocity | Submergence |
|---|---|---|---|
| Single cylinder | 0.2:0.05:0.9 | 2:0.5:9 | - |
| Twin cylinders $\lambda = 2$ | 0.2:0.05:1.0 | 2:0.5:10 | - |
| Twin cylinders $\lambda = 3$ | 0.2:0.05:0.8 | 2:0.5:8 | - |
| Twin cylinders $\lambda = 4$ | 0.5:0.05:0.9 | 2:0.5:9 | 6.8, 5.6, 3.7, 2.7, 1.8 |

## 3.3 Experimental data post-processing

In these tests, 2-dimensional results, including the response amplitude and the drag and lift coefficients of the twin-cylinder cross section, were expected. To measure the 3-dimensional effects, force and displacement sensors were placed at both ends of the cylinders. The data from both ends were identical, revealing only weak 3-dimensional effects, as shown by the series presented in the Appendix C.

The oscillation displacement and the lift and drag forces were recorded by sensors with a sampling frequency of 200 $Hz$. The post-processing methods to achieve the lift and drag forces and corresponding force coefficients will be introduced here. The coordinate system is first defined in Fig. 3.12. The longitudinal axes of the twin cylinders lie along the x-axis. The direction of the flow is parallel to the y-axis, and the CF direction is along the z-axis

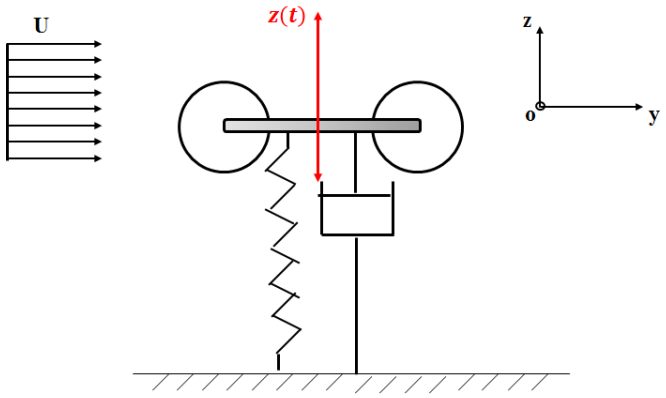


*Figure 3.12: Definition of the coordinate system in the tests.*

### 3.3.1 Stable stage selection

To obtain clear VIV features, a stable stage must be carefully selected based on the towing velocity. The velocity was increased from 0 to the required value, remained constant for some time and then decreased to 0, as shown in Fig. 3.13. Generally, the data obtained in the stable stage can be used for analysis. However, in these tests, the data from the first 1/3 of the stable stage were abandoned to avoid transient effects.

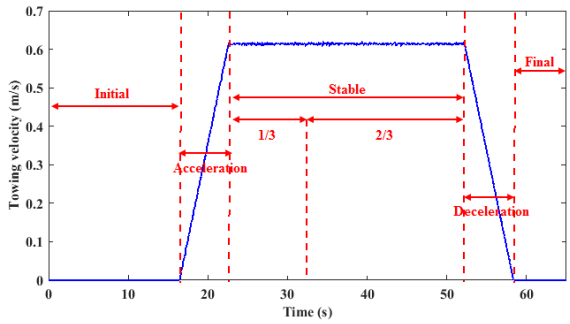


*Figure 3.13: Stable stage selection based on the towing velocity.*

### 3.3.2 Band-pass filter

In this study, only the stable VIV response and the corresponding vortex-induced forces at the dominant frequency were considered, thus, a bandpass filter was adopted to extract the VIV response and the forces at the dominant frequency from the original data. The passband of the filter was set based on the Strouhal number given by Zdravkovich [138].

### 3.3.3 Lift force acquisition

The lift force measured in a self-oscillation test includes only both a lift force and an inertial force due to the sensor arrangement, as shown in Fig. 3.14. According to Newton's second law, the relation among these forces can be expressed as

$$F_m(t) - F_L(t) = m\ddot{z} \tag{3.1}$$

where, $F_m(t)$ is the measured force, $F_L(t)$ is the lift force, and $m\ddot{z}$ is the inertial force.

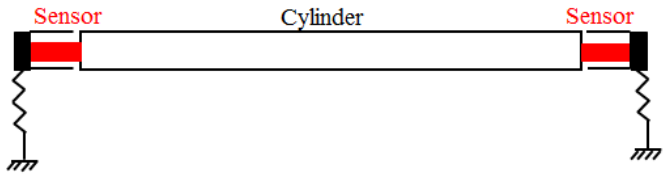


*Figure 3.14: Force measuring system.*

Fig. 3.15 shows the time histories of the measured force in CF direction and the identified lift force. To verify the identification procedure, the displacement response was recalculated based on the identified lift force by

solving the motion equation of a single degree of freedom system, as shown in Fig. 3.16. The recalculated displacement matches the measured displacement perfectly, thus proving the reliability of the lift force identification method

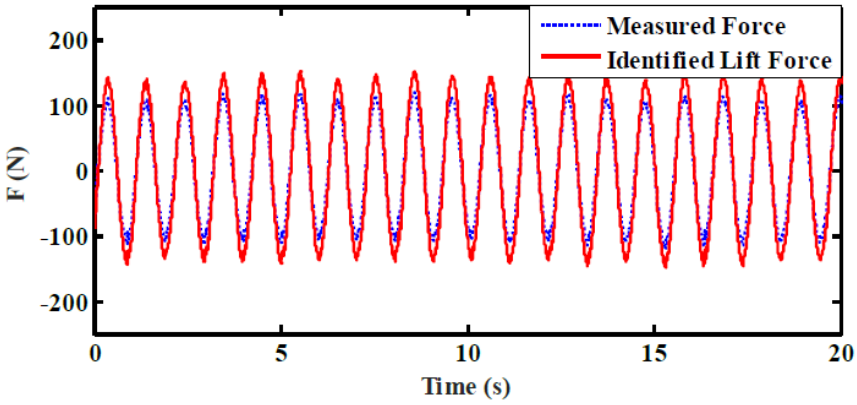


*Figure 3.15: Measured force ($F_m(t)$) and lift force ($F_L(t)$) for a single cylinder model ($U_r = 5$).*

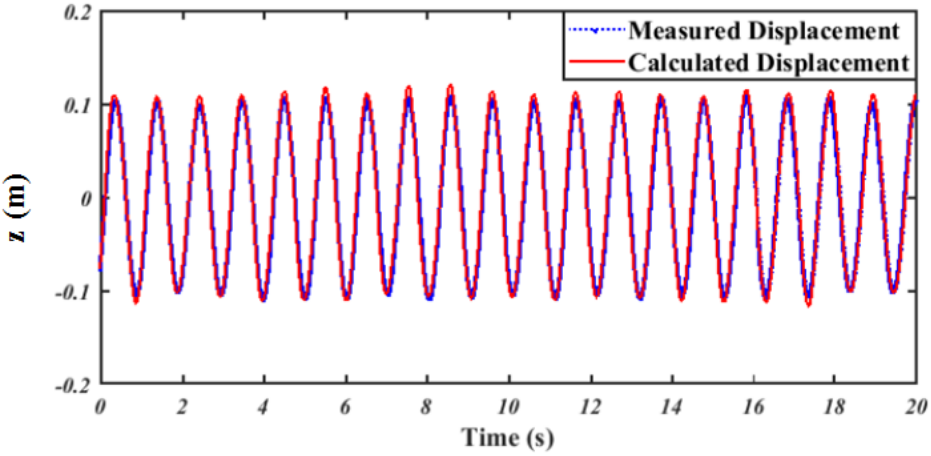


*Figure 3.16: Measured displacement and the displacement calculated based on the identified lift force for the single-cylinder model ($U_r = 5$).*

### 3.3.4 Lift and drag force coefficients from the test results

Lift and mean drag coefficients are obtained from the following equation,

$$\begin{cases} C_D = \frac{F_y}{\frac{1}{2}\rho D l U^2} \\ C_L = \frac{F_z}{\frac{1}{2}\rho D l U^2} \end{cases} \tag{3.2}$$

where $F_z$ is the peak value of the CF lift force $F_L(t)$. It is obtained by multiplying the root-mean-square (rms) value by $\sqrt{2}$, assuming the lift force series is with only one dominant frequency and zero mean value. $F_y$ is the time-average IL mean drag force extracted from the stable stage of the drag force series.

### 3.3.5 Least square method for excitation and added mass coefficients

As discussed in the former chapter, the CF lift force includes two components, i.e., an excitation force and an added mass force, representing the components in phase with the oscillation velocity and acceleration, respectively. In the lock-in state, the vibration and the lift force have the same frequency written as:

$$\begin{cases} z = z_0 \sin(\omega t) \\ F_L = F_z \sin(\omega t + \varphi) \end{cases} \tag{3.3}$$

Then the lift force per unit length of the cylinder can be re-written as,

$$\begin{cases} F_L = F_z \sin(\omega t + \varphi) = F_z \cos(\omega t) \sin\varphi - (-F_z \sin(\omega t) \cos\varphi) \\ F_z \cos(\omega t) \sin\varphi = \frac{1}{2}\rho D U^2 C_{Le} \frac{\dot{z}}{|\dot{z}|} \\ -F_z \sin(\omega t) \cos\varphi = \frac{1}{4}\rho\pi D^2 C_{La} \ddot{z} \end{cases} \tag{3.4}$$

where $C_{Le}$ and $C_{La}$ are the excitation coefficient and added mass coefficient, respectively. $\rho$, $U$, and $D$ denote the fluid density, flow velocity and cylinder diameter. In the stable stage of VIV, oscillation is normally dominated by one frequency, the oscillation velocity and excitation coefficient can be further re-written as,

$$\begin{cases} \dot{z} = \sqrt{2} \times rms(\dot{z}(t)) \cos(\omega t) \\ \frac{\dot{z}}{|\dot{z}|} = \frac{\dot{z}}{\sqrt{2} \times rms(\dot{z}(t))} \\ F_z \cos(\omega t) \sin\varphi = \frac{1}{2}\rho D U^2 C_{Le} \frac{\dot{z}}{\sqrt{2} \times rms(\dot{z}(t))} \end{cases} \tag{3.5}$$

To obtain the two coefficients $C_{Le}$ and $C_{La}$ from test result, a least square method was applied by minimizing the squared error between the measured

force and predicted force over a given time,

$$e^2 = \left[\frac{1}{2}\rho DU^2 C_{Le}\frac{\dot{z}}{\sqrt{2}\times rms\left(\dot{z}\left(t\right)\right)} - \frac{1}{4}\rho\pi D^2 C_{La}\ddot{z} - F_{L-m}\right]^2 \tag{3.6}$$

where $F_{L-m}$ is the lift force based on Eq. 3.1. The square error $e^2$ obtains the minimum in terms of the coefficients when,

$$\frac{\partial e^2}{\partial C_{Le}} = 0, \frac{\partial e^2}{\partial C_{La}} = 0 \tag{3.7}$$

The two coefficients can be finally addressed as,

$$\begin{aligned} C_{Le} &= \frac{\sqrt{2}\times rms(\dot{z}(t))}{\rho DU^2}\frac{a_2a_5 - a_3a_4}{a_2^2 - a_1a_4} \\ C_{La} &= \frac{4}{\rho\pi D^2}\frac{a_1a_5 - a_3a_2}{a_2^2 - a_1a_4} \end{aligned} \tag{3.8}$$

where $a_1 = \dot{z}^2, a_2 = \dot{z}\ddot{z}, a_3 = F_{L-m}\dot{y}, a_4 = \ddot{z}^2, a_5 = F_{L-m}\ddot{z}, a_6 = {F_{L-m}}^2$

## 3.4 Uncertainty analysis

### 3.4.1 Residual flow

Between each test circle, a 10-minute waiting was used to ensure the fluid at rest, since there were residual flows induced by the towing velocity. Ersdal [139] proposed an empirical equation to estimate the residual flow effects based on far wake theory:

$$\frac{u_1}{U_0} = 1.2\left(\frac{U_0 t}{C_D D}\right)^{-0.5} \tag{3.9}$$

Large residual flow could lead the relative flow velocity different from the designed one, which will further induce uncertainties on the VIV features and hydrodynamic coefficients.

### 3.4.2 Cylinder ends conditions

To avoid three-dimensional end effects of the cylinder stemming from the finite length of it, two methods were introduced to ensure two-dimensional flow. Firstly, two short dummy cylinders with the same diameter as the model were assembled at both ends. Secondly, two circular endplates were assembled outside the dummy cylinder to reduce the impact of other devices on the flow field. They were fixed on the support frame and do not oscillate with the twin-cylinder during test. The size of the plates were designed based on the Stansby's suggestion [140] , with at least extending $2.5D$ upstream, $4.5D$ downstream, and $5D$ in height.

### 3.4.3 Friction of track

A pair of low-friction tracks were mounted on one side of each frame to guide the CF motion. When the towing velocity changes from the positive to negative, the normal forces on the sliders (stemming from IL loads on the cylinders) slightly affect the frictions between the sliders and tracks. From the calibration test shown in Appendix B, when the normal force is positive (direct to the slider), the friction approximately remains constant regardless of the normal force value. During the test, positive normal force was ensured by the positive flow velocity.

### 3.4.4 Blockage effects

"Blockage" refers to the fact that the VIV features and force coefficients measured on the twin cylinders in a finite body of water is different from the values expected in an infinite stream due to tank walls and free surface.

Blockage ratio defined by the cylinder diameter dividing the water depth was normally used to measure the effect [138]. For the cases $R_e > 300$ and blockage ratio less than 1/10, the blockage effect can be neglected. In the present self-oscillation test, the blockage ratio is 1/16 and $R_e = 10^4$.

### 3.4.5 Towing tank length

The length of the stable stage in each test is limited by the length of the towing tank. The acceleration and deceleration stages have to be removed due to transient effects. The effective length of the MC-towing tank $L_T$ is about 20 $m$, which means the effective duration can be simply calculated as $L_T/U$. For the stable stage, the number of stable cycles ($N_{osc.}$) is:

$$N_{osc.} = \frac{L_T}{U} f_{osc} \tag{3.10}$$

where $f_{osc}$ is the VIV response frequency which is increased with the flow velocity. To obtain sufficient stable cycles, the maximum towing velocity is set to be 1.2 $m/s$.

# Chapter 4

# Summary of the Main Results

Experimental study on the features of the VIV response, and lift and drag force coefficients are firstly conducted and discussed in Paper I and II. Then, the obtained vortex induced force coefficients are used as input for the simulation of the dynamic response of the SFT in waves and currents, as presented in Paper III. The work serves as a basic reference for SFT design considering VIV effects.

## 4.1 Paper I: Experimental study of vortex-induced vibration of a twin-tube submerged floating tunnel segment model

The cross-flow vortex-induced vibration features of a submerged floating tunnel element, which is composed of two rigidly connected cylinders in a tandem configuration, were investigated via a self-oscillation model test in a steady flow. A new understanding on the VIV response, lift force and torsional moments is achieved

***(1) VIV amplitude and frequency of the twin-tube segment model in current***

The response amplitude and frequency of the twin cylinders are presented as functions of the reduced velocity and spacing ratio. As shown in Fig. 4.1, the results for a single cylinder are also provided as a reference.

There are obvious differences between the response amplitude and frequency of the twin cylinders and those of the single cylinder when the spacing ratio is 2 or 3. The differences are diminished when the spacing ratio

reaches 4. The initiation of VIV is observed at a larger reduced velocity for the twin cylinders ($U_r = 4.5$ for $\lambda = 2$) than for the single cylinder ($U_r = 2.5$). The response frequency of the twin cylinders when $\lambda = 2$ is lower than that of the single cylinder. Weak vortices causing the water in the gap area to oscillate with the twin cylinders might be the reason for this phenomenon, since a similar phenomenon is observed for a squared/elliptic cylinder [141, 142].

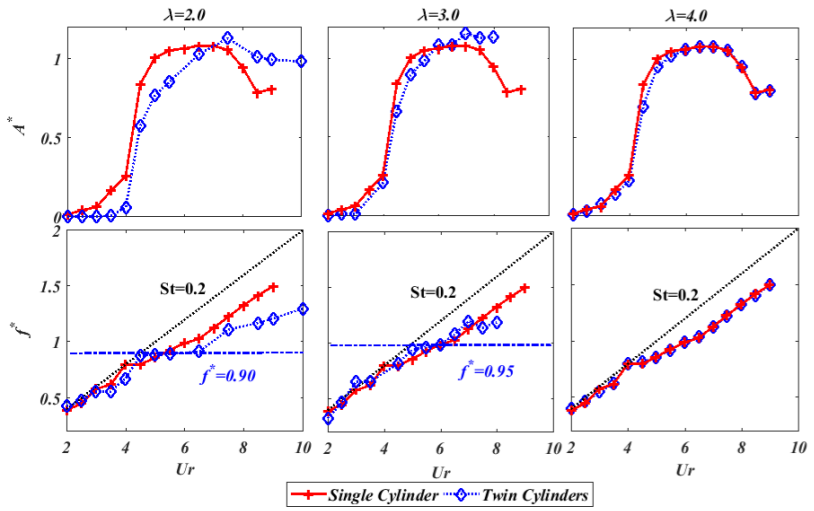


*Figure 4.1: Response amplitude and frequency under different spacing ratios, the red crosses represent the results for a single cylinder; the blue diamonds denote the results for twin cylinders.*

***(2) Lift forces on the twin-tube segment model in current***

The CF lift forces in VIV condition are further studied through a comparison with the stationary results for twin cylinders and the oscillation results for a single cylinder. Generally, VIV strongly amplifies the lift forces on both cylinders and modifies the relation between them. In the stationary results, the downstream cylinder is subject to a larger lift force than the upstream cylinder. An opposite relation is observed when a significant VIV is excited, as shown in Fig. 4.2. The lift coefficients in all cases are shown in Fig. 4.3. Similar to that of a single cylinder, the lift coefficients of both cylinders initially increase rapidly and then sharply decrease. However, their rates of change are different. Based on the difference between the lift coefficients, the curves in Fig. 4.2 can be divided into three regions:

- (I) Initial small difference region.

- (II) Significant difference region
- (III) Terminal constant difference region

The difference remains at a small constant value in region I. It then significantly increases in region II and finally drops to a small constant in region III. Region II is clearly observed in the cases of $\lambda = 2$ and 3, while it disappears when $\lambda = 4$.

***(3) Torsional moments on the twin-tube segment model in current***

The corresponding lift difference induces an extra torsional moment on the structure:

$$T = |F_{L\_D} - F_{L\_U}| \, L/2 \tag{4.1}$$

where $F_{L\_U}$ and $F_{L\_D}$ denote the lift forces on the upstream and downstream cylinders, respectively, and $L$ is the spacing distance. The torsion can also be expressed as a sinusoidal function with only one dominant frequency. Moreover, for each spacing ratio, the torsional moment is approximately quadratic in the flow velocity; thus, a torsional coefficient can be proposed:

$$C_T = \frac{T}{\frac{1}{4}\rho D U^2 l L} \tag{4.2}$$

where $U$, $D$, $\rho$ and $l$ are the flow velocity, cylinder diameter, fluid density and cylinder length, respectively. Fig. 4.4 shows the torsional coefficient versus the reduced velocity for the different spacing ratios. The torsional coefficient increases sharply in region II, especially at smaller spacing ratios. In regions I and III, for all spacing ratios, stable variation of the coefficient can be observed. From the perspective of the torsional moment, a spacing ratio of 2 is not a good choice due to the sharp increase near $U_r$=4.

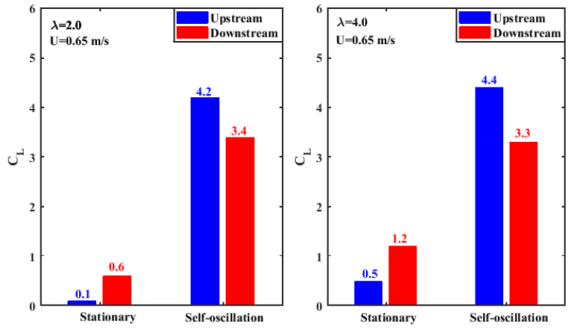


*Figure 4.2: Lift coefficient comparison between the stationary results and self-oscillation results.*

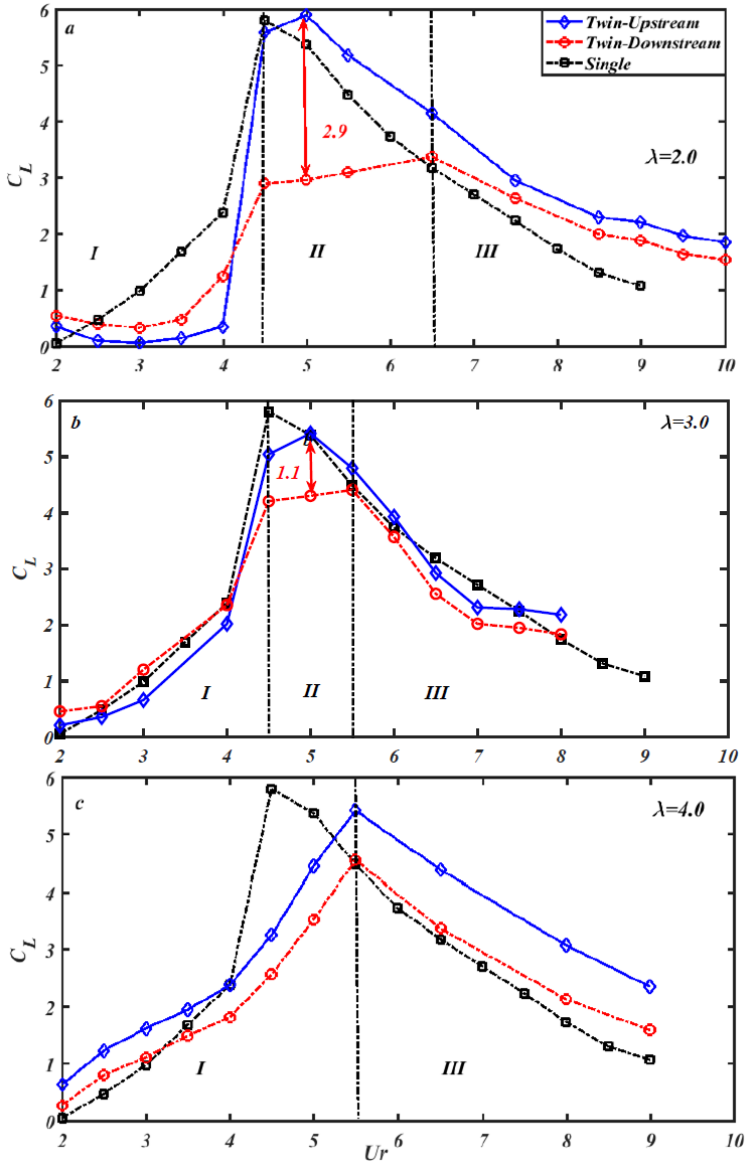


*Figure 4.3: Lift coefficients as a function of the reduced velocity and spacing ratio.*

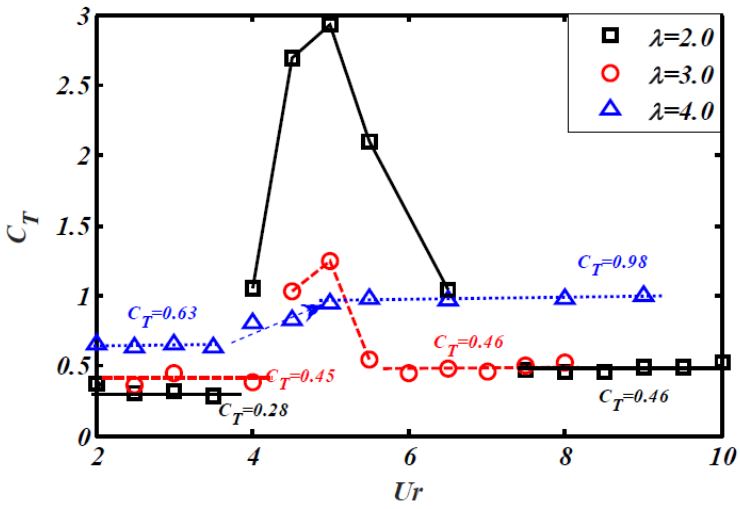


*Figure 4.4: Torsional coefficient of the rigidly connected tandem twin cylinders.*

## 4.2 Paper II: Experimental study on the drag forces on a twin-tube submerged floating tunnel segment model in current

The drag forces on a rigid segment of a twin-tube SFT under various $R_e$ number and submergence are investigated in this paper. The effects of the spacing distance between two cylinders and VIV response on the drag forces are also analyzed through stationary and self-oscillation towing tests.

***(1) Drag forces in stationary model test***

The mean drag forces on the upstream and downstream cylinders in stationary test are briefly shown in Fig. 4.5 along with the results for a single cylinder as a reference. The drag forces on the upstream cylinder are much larger than those on the downstream cylinder, and the forces on the two cylinders are in opposite directions when the spacing ratio is 2 and 3. To provide a basic reference for tunnel design, the total drag force and the difference in the drag forces are presented in the form of the corresponding coefficients:

$$\begin{cases} F_{D\_U} + F_{D\_D} = \frac{1}{2}\rho C_{D\_T} DlU^2 \\ F_{D\_U} - F_{D\_D} = \frac{1}{2}\rho C_{D\_\delta} DlU^2 \end{cases} \tag{4.3}$$

where $F_{D\_U}$ and $F_{D\_D}$ are the mean drag forces on the upstream and downstream cylinders, respectively, $C_{D\_T}$ and $C_{D\_\delta}$ denote the coefficients of the

total drag force and the drag force difference, respectively. For small spacing ratios such as 2 and 3, the total drag force is close to that on a single cylinder, while the drag force difference is slightly smaller. The former is useful for global strength calculations, while the latter can be used in the design of local structures, such as the horizontal bracings between the two tubes.

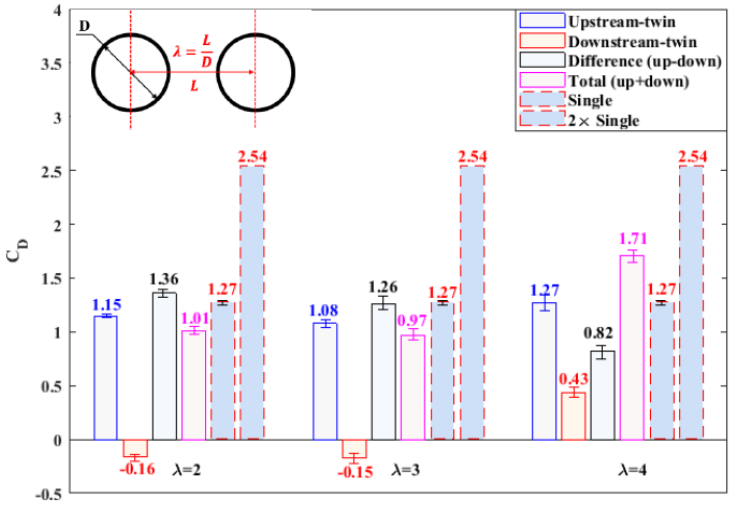


*Figure 4.5: Mean drag coefficients of a single cylinder and twin cylinders with various spacing ratios.*

### *(2) VIV effects on drag forces*

The VIV-amplified mean drag forces on the twin cylinders are shown in Fig. 4.6, along with that for a single cylinder. In contrast to the stationary results, the drag forces are in the same direction when the VIV is excited. The relative velocity is not horizontal because the CF vibration is the main reason for this phenomenon. The change in the drag force with the reduced velocity is strongly related to the response amplitude, i.e., the drag forces increase with increasing amplitude and vice versa. Compared with that on a single cylinder, the drag forces on the twin cylinders are smaller, especially for the downstream cylinder.

The previously defined total drag force and drag force difference (in Eq. 4.3) are also discussed. A novel phenomenon is observed: the maximum total drag force and drag force difference are both linear in the spacing ratio and the maximum drag force on a single cylinder under VIV conditions, as

follows:

$$\begin{cases} C_{D\_T} = (1+\lambda)\, C_D^s \\ C_{D\_\delta} = \frac{7}{40}\lambda C_D^s \end{cases} \tag{4.4}$$

where $\lambda$ is the spacing ratio and $C_D^s$ is the maximum drag coefficient on a single cylinder under VIV conditions. It should be noted here that these drag coefficients are mostly obtained for the case of $U_r = 6$, and these relations could be conservatively adopted in the IL load design of an SFT.

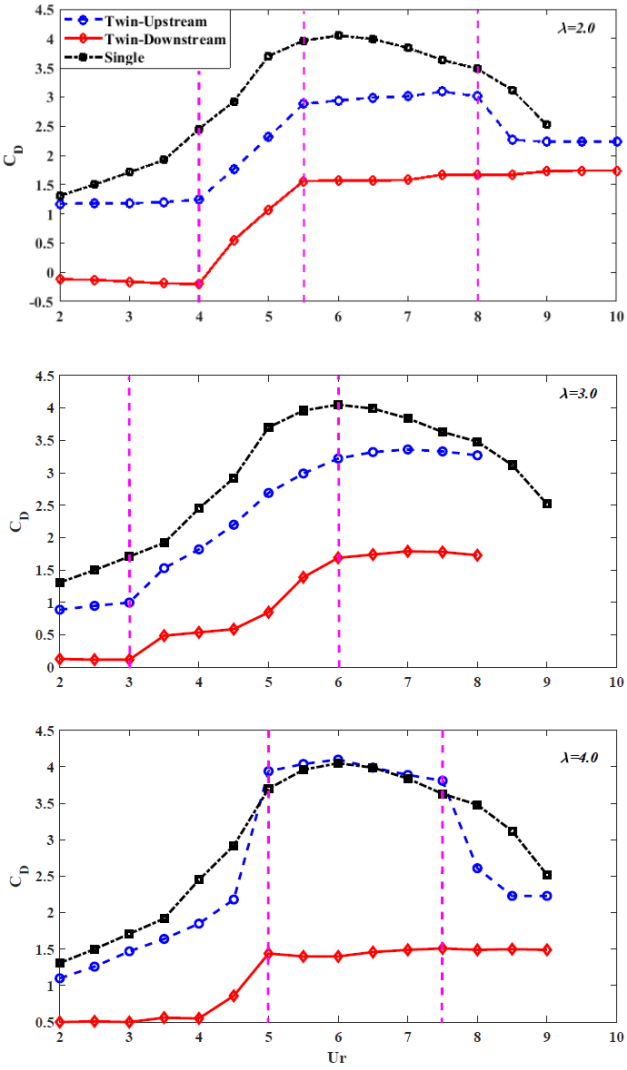


*Figure 4.6: VIV-amplified mean drag coefficients of the up- and downstream cylinders with various spacing ratios.*

***(3) Submerged depth effect on drag forces***

The effect of the free surface on the drag forces is studied to provide a reference for the selection of the submergence of the SFT in the design. The mean drag force on the upstream cylinder is presented as a function of the reduced velocity and submergence in Fig. 4.7. Three critical reduced velocities, $U_r = 6.5, 4.5$ and $3.0$, are observed for submerged depth ratios of 3.7, 2.7 and 1.8, respectively. The Froude number ($F_n = \frac{U}{\sqrt{gh}}$, where $h$ and $g$ are the submerged depth and gravitational acceleration, respectively) is usually used to describe the effect of submergence. However, no critical $F_n$ is observed to separate the regions in which the free surface effect should or should not be taken into account in this experimental study.

Inspired by the reduced velocity, which is widely used to assess the likelihood of lock-in in VIV analysis, a nondimensional submerged depth is proposed,

$$h' = \frac{f_n h}{U} \tag{4.5}$$

where $h$ is the distance between the initial free surface and the lower side of the cylinder. Fig. 4.8 shows the drag force on the upstream cylinder as a function of the newly defined nondimensional depth. The dashed line indicates the critical value of $h'$. The drag coefficients are independent of the submergence as $h' > h'_{cri}$.

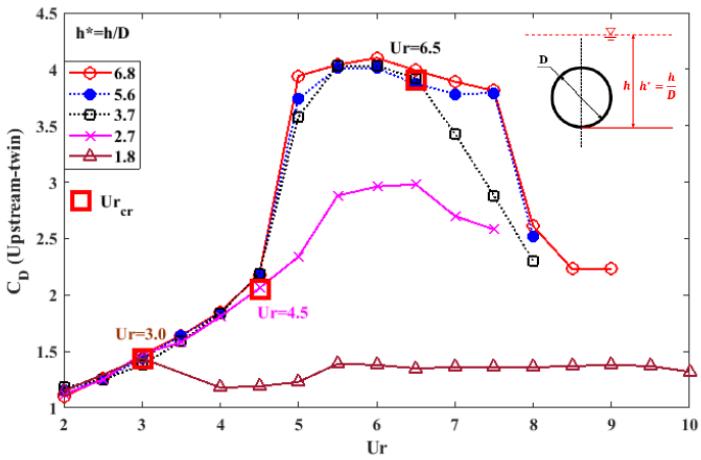


*Figure 4.7: Mean drag coefficient of the upstream cylinder under various submergences.*

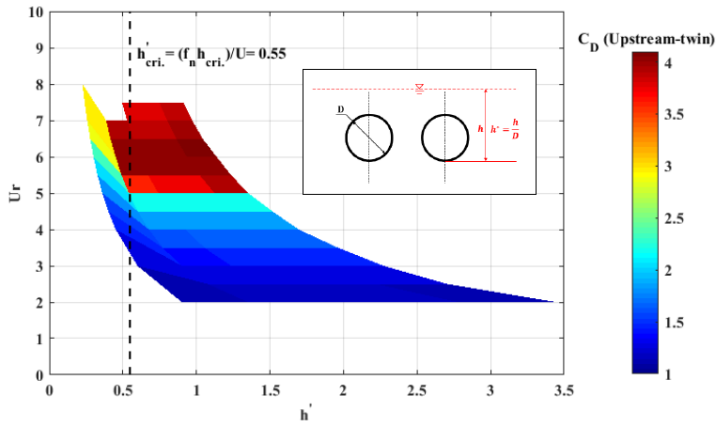


*Figure 4.8: Mean drag coefficient of the upstream cylinder versus the newly defined submerged depth.*

## 4.3 Paper III: Numerical simulation of wave-induced hydroelasticity and flow-induced vibration of a twin-tube submerged floating tunnel

Numerical simulation of wave-induced hydroelastic motions and flow-induced vibrations of the twin-tube SFT are discussed in this paper, the short-crested waves, second order wave loads, vortex-induced vibration (VIV) and VIV-amplified inline drag forces are taken into consideration.

***(1) Eigenfrequencies and eigenmodes of the SFT***

The numerical model of the pontoon-supported curved SFT is shown in Fig. 4.9. It consists of two identical tubes in tandem configuration, which connected by large diameter horizontal bracings, supported by 16 pontoons and submerged 12 $m$ below the mean sea level. The spacing ratio of the tunnel is 3 in the design.

Eigenvalue analysis was conducted firstly to obtain the eigenfrequency and mode shape. The added mass of pontoons at infinite frequency were adopted. The first three eigenmodes are listed in Table. 4.1 and shown in Fig. 4.10.

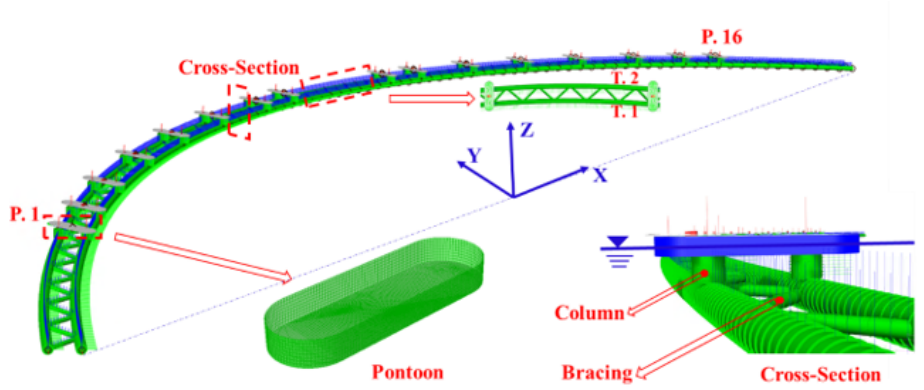


*Figure 4.9: Numerical model of the pontoon-supported curved SFT in SIMA.*

*Table 4.1: The first three eigenmodes of the SFT.*

| Mode | Period | Frequency | Dominating Motion | |
|---|---|---|---|---|
| | [s] | [rad/s] | Primary | Secondary |
| 1 | 50.25 | 0.125 | Y | - |
| 2 | 27.25 | 0.231 | Y | - |
| 3 | 21.37 | 0.294 | Z | - |

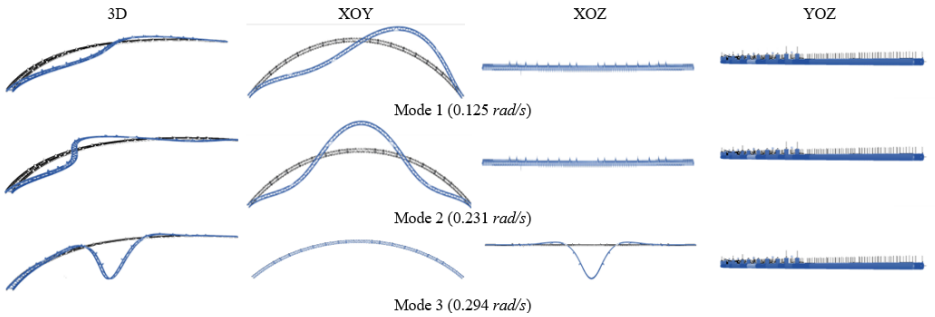


*Figure 4.10: First three eigenmodes of the SFT.*

The flow velocity in the fjord is considered to consist of two components in the case study, i.e., surface current velocity and Stokes drift velocity. From a conservative view of the load modeling, the former with a return period of 1000 years is used here, which is approximately 1.6 $m/s$. The

Stokes drift velocity can reach 0.6 $m/s$ as $H_s$=2.4 $m$, $T_P$=5.9 $s$. Hence, the equivalent flow velocity is 2.2 $m/s$.

In this extreme condition, the reduced velocity ($U_r = \frac{U}{f_n D}$) for the first order vertical natural mode, corresponding to the third order natural mode, is about 3.8. According to the experimental results discussed in Section. 4.1, this mode can be excited by vortex induced forces due to the corresponding reduced velocity is approximately located at the lower threshold of the critical range.

***(2) Wave induced hydroelastic response of the SFT***

The wave loads acting on the floating pontoons are calculated by the panel method, whereas the loads on the tunnel tubes, horizontal bracings, and columns are calculated using the Morison equation. A wave field modelled by JONSWAP spectrum with $H_s$=2.4 $m$, $T_P$=5.9 $s$ and the main direction $270^o$ is considered in the case study.

The STD of the lateral and vertical motion and the corresponding bending moments of Tube 1 are presented in Fig. 4.11 and 4.12. It is found that the $2^{nd}$ order wave force substantially increases the lateral motion by exciting $1^{st}$ and $2^{nd}$ order low frequency eigenmodes and makes very few difference on the vertical motion, as expected. For the lateral bending moment $M_z$, the long-crest waves induced nearly twice larger value than short-crest waves if only first order wave force is considered. If the second order force is also included, the short-crest waves lead to a large $M_z$ due to that it can excite both the $1^{st}$ and $2^{nd}$ natural modes in lateral direction.

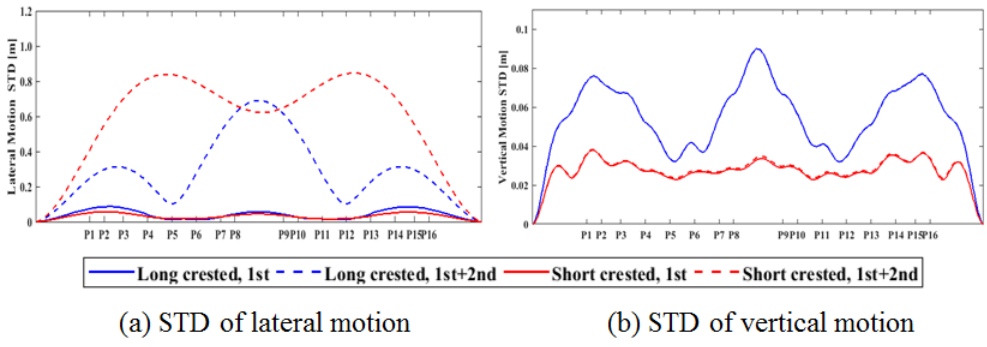


*Figure 4.11: Standard deviation of lateral (a) and vertical (b) motions in wave loads.*

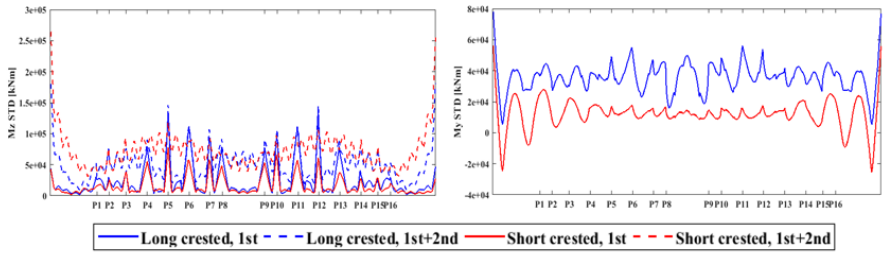


(a) STD of lateral bending moment $M_z$ (a) STD of vertical bending moment $M_y$

*Figure 4.12: Standard deviation of lateral (a) and vertical (b) bending moment in wave loads.*

***(3) Vortex induced vibration of the SFT***

A simplified VIV prediction method was proposed based on the test result in Section.4.1 and 4.2. The governing motion equation of the tunnel element can be represented as follows

$$M_T\ddot{z} + C_T\dot{z} + K_T z = F_{hyd\_CF\_T.i}\,(i = 1, 2) \tag{4.6}$$

where $\ddot{z}$, $\dot{z}$ and $z$ are the acceleration, velocity and displacement matrix of the node in CF direction, respectively; $M_T$, $C_T$ and $K_T$ are the structural mass, damping and stiffness matrix of the tunnel, respectively. The subscript $T.i \quad (i = 1, 2)$ refers to the down- and upstream cylinder, respectively. $F_{hyd\_CF\_T.i}$ denotes the hydrodynamic force in the crossflow direction, which could be modeled by,

$$\begin{aligned} dF_{hyd\_CF\_T.i} = {} & \tfrac{1}{2}\rho D\sqrt{U^2 + \dot{z}^2}\,UC_{L-T.i}\sin\left(\phi_{T.i}\left(t\right)\right)dl - \\ & \tfrac{1}{2}\rho DC_{D-T.i}\sqrt{U^2 + \dot{z}^2}\,\dot{z}dl - \left(C_M - 1\right)\rho\tfrac{\pi D^2}{4}dl \end{aligned} \tag{4.7}$$

where $\phi_{T.i}\left(t\right)$ is the instantaneous phase of the lift force and is simplified to $\omega_{T.i}t + \varphi_{T.i}\left(x\right)$. $\omega_{T.i}t$ is the oscillation frequency of the lift force. It is assumed to be locked to the frequency of the natural mode that is excited by the vortex shedding, as expressed as: $\omega_{T.1} = \omega_{T.2} = \omega_n$, where $\omega_n$ is the frequency of the excited mode in still water. $\varphi_{T.i}\left(x\right)$ is the initial phase of the lift force along the tunnel, which are set to be either 0 or $\pi$ based on the mode shape, as shown in Fig.2.7. $C_{L-T.i}$ and $C_{D-T.i}$ are the lift and drag coefficients based on the self-oscillation test. The inertial coefficient $C_M$ is set to be 2. A comparison between the prediction and experimental results shows the reasonable of the simplified VIV prediction method for a flexible cylinder in a constant flow system.

The vortex-induced vertical motion and the corresponding bending moment $M_y$ of the two tubes are shown in Fig. 4.13 and Fig. 4.14. The maximum vertical motion ($STD/D \approx 0.31$) observed in the middle is due to the extra long span between pontoons. It is approximately 50 times larger than that induced by long-crested waves, which however, is very small due to the low wave condition in the fjord. Adding extra supporting structures (such as pontoons and pretensioned tethers) along the navigational span in the middle part can be a possible way to decrease the VIV amplitude to some extent by providing a larger hydrostatic stiffness in vertical direction. While traditionally, VIV is normally considered as a source of the fatigue damage, it might be important for the ultimate limit state design of SFTs.

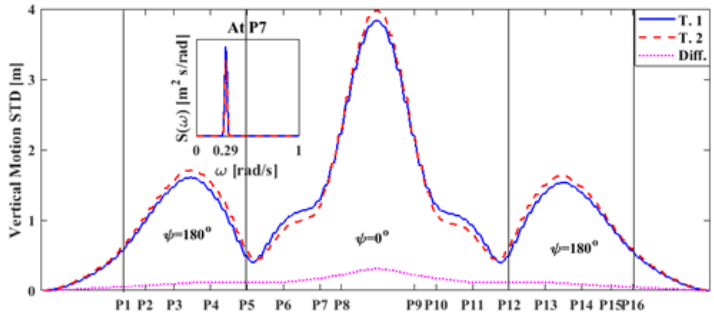


*Figure 4.13: Standard deviation of vertical motion along the tunnel tubes and the difference between T. 1 and T. 2, as well as power spectra density of vertical motion at tube node P7.*

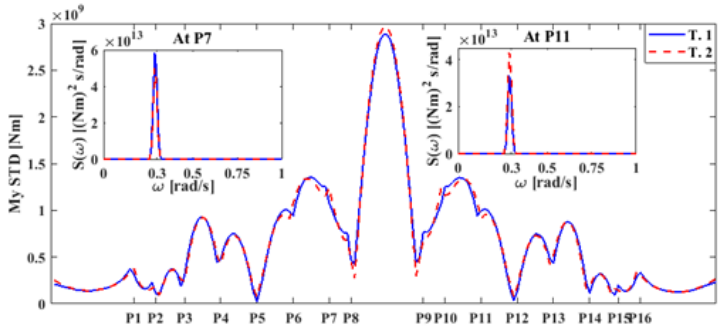


*Figure 4.14: Standard deviation of $M_y$ along T.1 and T. 2, as well as the power spectra density of $M_y$ at tube nodes P7 and P11.*

# Chapter 5

# Conclusions and Recommendations for Future Work

Two main concepts were addressed in this study. First, a series of self-oscillation tests were conducted to obtain the vortex-induced vibration (VIV) features of a rigidly connected tandem twin-cylinder model with respect to the spacing distance, flow velocity and submergence. Based on the test results and a simplified time-domain VIV prediction method, VIV features of a full scale SFT was then illustrated. Moreover, the effects of wave loads were investigated, including the second-order wave forces and short-crested waves.

In this chapter, the conclusion will first be summarized, followed by an outline of original contributions, limitations of the model tests and numerical simulations, which could inspire future work on the improvement of the hydrodynamic response calculation of an SFT.

## 5.1 Conclusions

### 5.1.1 Experimental study of VIV features of a twin-tube SFT

VIV of a submerged floating tunnel has been preliminarily investigated through a self-oscillation test of elastically supported tandem twin rigid cylinders with small mass ratio in CF direction in a steady flow. The influence of spacing ratio on VIV response, lift coefficient, torsional coefficient and mean drag coefficient were mainly studied.

**(1) On the VIV response, lift coefficient and torsional coefficient of twin cylinders (paper I)**

For a twin-tube SFT, the VIV features would be more complex than that of a single cylinder owing to the interaction between the two identical tubes arranged in tandem, especially at a small spacing ratio. The conventional knowledge based on the single cylinder test are not suitable.

From the twin-cylinder model test, the differences in VIV between the single- and twin-cylinder models are observed until the spacing ratio ($L/D$) reaches 4. Twin-cylinder has smaller critical reduced velocity (corresponding to the initiation of VIV) and dominant frequency than that of a single cylinder, but a little larger maximum response amplitude.

The lift forces on the twin cylinders were presented as a function of reduced velocity and spacing ratio, respectively. They have a similar trend with the reduced velocity but the dependence ratios are different. The different lift forces acting on the up- and down-stream cylinders induce a torsional moment, which is quadratic to the reduced velocity in the initial small difference region and terminal constant difference region (the regions are defined by the difference between lift coefficients of upstream and downstream cylinders). A sharp increase in the torsional moment and torsional coefficient is observed at the small reduced velocity as $\lambda = 2$. In the range $2 < U_r < 4$, the torsional coefficient for $\lambda = 3$ is much smaller than that for $\lambda = 4$. This fact suggests that $\lambda = 3$ is favourable for the tunnel design based on the present experimental results.

**(2) On the drag coefficient of twin cylinders (paper II)**

In addition to the lift force and torsional moment, VIV amplified-drag forces on the two cylinders are further discussed with respect to the spacing ratio and tunnel submergence. The drag coefficients of two cylinders under VIV condition were presented as a function of reduced velocity and spacing ratio, respectively. The maximum drag coefficients are coincidently observed at the reduced velocity with the maximum response amplitude. A measure for the submergence when the free surface effect is taken into account, is established by introducing a new non-dimensional submerged depth ($h'=\frac{hf_n}{U}$). When $h'$ is 0.55 (i.e. $h_{cri}$'), it is found that both the VIV response amplitude and the drag forces are independent of the submergence as $h' > h'_{cri}$.

### 5.1.2 Numerical study of wave-induced hydroelasticity and flow-induced vibration features of a full-scale SFT (paper III).

Dynamic features of the full scale SFT were studied considering wave-induced hydroelastic response and flow-induced vibrations, separately. In the former case, the $2^{nd}$ order wave forces on the pontoons and short-crested waves were considered. In the latter case, in a conservative manner, the flow velocity was determined as the sum of the 1000-year return current and Stokes drift velocity. In the selection of the vortex-induced force coefficients, the lift force coefficient was selected from the self-oscillation test (shown in paper I and II) using the reduced velocity and spacing ratio as the criteria.

**(1) On the features of wave-induced hydroelasticity of the SFT**

For the wave-induced hydroelastic response, the $2^{nd}$ order wave force substantially increases the lateral motion by exciting the $1^{st}$ and $2^{nd}$ order low frequency eigenmodes, but has a small effect on the vertical motion. The long-crested waves induce a larger $M_z$ than short-crest waves if only $1^{st}$ order wave force is considered. The short-crested waves lead to a large $M_z$ due to that it can excite both the $1^{st}$ and $2^{nd}$ natural modes in lateral direction when the $2^{nd}$ order wave forces are also included.

**(2) On the features of flow-induced vibration of the SFT**

In the VIV analysis, the effects of lift force and VIV-amplified IL drag force were evaluated. According to the numerical simulation results, the maximum STD of the vortex-induced vertical motion ($STD/D \approx 0.31$) and the corresponding bending moment $M_z$ at the middle part of the SFT are much larger than those induced by long-crested waves. However, the wave-induced responses are very small in an absolute sense. Except for the central long span between pontoons, the effect of VIV is moderate. Therefore, by providing extra supporting structures (such as pontoons and pretensioned tethers) along the navigational span in the middle part could reduce the VIV amplitude by providing a larger hydrostatic stiffness in the vertical direction.

## 5.2 Original contributions

The list below summarizes all the original contributions in this thesis:

- Very few studies on the VIV of a twin-tube submerged floating tunnels

have been carried out before. Most previous investigations focused on a single cylinder or two unconnected cylinders (two cylinders oscillate individually). In this thesis, a free oscillation experiment of two rigidly connected cylinders in tandem arrangement is conducted and yields a new understanding on the VIV response and vortex-induced loads of the twin-tube SFT model.

- The previous research on the VIV is mainly on the responses and loads in CF and IL directions. The load in the torsional direction derived from the vortex-induced lift force difference are first observed and analyzed for the twin-tube structure in the thesis. A torsional coefficient is further proposed and its variation with the spacing ratio is estimated, which provides an essential reference for the design of the SFT.

- The selection of the submerged depth of the SFT is a key part during the design. Hence, the effect of the submerged depth on the vortex-induced loads is investigated. It is found that there exists no case-independent Froude number (a widely used parameter to represent the free surface effect) that can divide the regions whether or not we should consider the free surface effect on the drag forces of the twin-tube structure. A novel non-dimensional submerged depth is proposed in the thesis. It is shown to capture the features observed in all experimental cases studies to determine whether or not to consider the free surface effect.

- In the VIV study of an SFT, previous studies mainly focused on the supporting anchor cables, and the VIV of the tubes have never been studied, especially for the twin-tube structure. A simplified time domain method combined with the free oscillation experiment data is proposed to predict the VIV of the SFT. A benchmark study of VIV prediction of a single flexible cylinder under uniform current was firstly done to verify the accuracy of the method. Then, the method is applied to predict the VIV of a full-scale SFT. It is found that the maximum vortex-induced vertical motion and the corresponding bending moment at the middle part of the SFT are much larger than those induced by the waves. It means that the VIV could be important also for the ultimate limit state design and not only a source of fatigue damage for an SFT.

## 5.3 Limitations

In this study, VIV of a submerged floating tunnel has been preliminarily investigated through a self-oscillation test of elastically supported tandem twin rigid cylinders with small mass ratio in CF direction in a steady flow. In the design of the test model, the horizontal bracings in the actual SFT were, as a starting point, neglected, and their effect of the hydrodynamic damping and flow pattern in the gap area were not included. VIV responses in inline and torsional direction, which could be very important for the VIV features, are not in the scope of the study. From the test result of VIV responses and mean drag forces with different submergences but a fixed spacing ratio of 4, a nondimensional submerged depth is proposed to give a suggestion on whether or not to consider the free-surface effect at a specific submergence and flow velocity. The effects of the cylinder diameter, natural frequency and spacing ratio, which could challenge the generality of the proposed nondimensional submerged depth are not assessed in the twin cylinders model test.

In the numerical simulation, to simplify the model construction process, the submerged depth of the SFT was set as a constant along the tunnel, the anisotropic concrete tube was replaced by an isotropic concrete tube, and the ballast water in the tube and pontoons were also neglected, but their mass was considered.

In the numerical wave-induced hydroelastic and flow-induced vibration analysis, the wave and flow field are assumed to be homogeneous and constant, respectively. In reality, the conditions along the tunnel will exhibit some inhomogeneity. The curved configuration induced different normal flow velocities along the tunnel, and this feature was also neglected in the VIV prediction process.

In the determination of the vortex-induced force coefficients in the flow-induced vibration analysis, due to a lack of experimental data on the twin-tube system, the lift force coefficient is selected from our self-oscillation test using the reduced velocity and spacing ratio as the criteria. The relations between the lift force coefficient and oscillation amplitude/frequency in the sophisticated simulations are neglected

## 5.4 Recommendations for future work

### 5.4.1 Forced oscillation test

In the present VIV prediction method, the lift coefficients of the twin-cylinder were selected from the self-oscillation test results using the reduced

velocity and spacing ratio as the criteria. However, to obtain the lift coefficient which is dependent on the oscillation amplitude at each frequency ratio, forced oscillation tests of a twin-cylinder model are suggested.

### 5.4.2 Computational fluid dynamics (CFD) simulation and particle image velocimetry (PIV) experiment

In this study a series self-oscillation tests were conducted to obtain the VIV features and force coefficients of twin cylinders. Due to the lack of information about the flow pattern, most phenomena can only be qualitatively described without a deep explanation. Therefore, a CFD simulation or a model test using PIV techniques are suggested to obtain flow pattern in the gap area and the wake of the downstream cylinder.

### 5.4.3 Numerical simulation of the dynamic response of the SFT under combined wave and current

In the present study, the wave-induced hydroelastic response and flow-induced vibration are discussed separately, except that the effect of low frequency oscillatory wave loads on the VIV is briefly mentioned. VIV of a slender structure can be affected by the wave-induced and forced motion from floating facilities-induced (wave-induced motion of the floating pontoons in an SFT) oscillatory flow as the $KC$ number is larger than the critical value [143]. The 'amplitude modulation' and 'mode transition' in the wave-affected VIV makes it very different from that induced by a constant flow. Therefore, the phenomenon needs to be studied experimentally and numerically.

# References


[1] Xiang X, Minoretti A, Eidem ME, Belsvik KH, Aasland TE, Vodolazkin M. Simplified hydrodynamic design procedure of a submerged floating tube bridge across the digernessund of norway. *International Conference on Offshore Mechanics and Arctic Engineering*, vol. 57779, American Society of Mechanical Engineers, 2017; V009T12A007.

[2] Lothe A, Musch O. Bjørnafjorden submerged floating tube bridge: sea state simulations. *Norconsult AS, Trondheim, Norway* 2015; .

[3] Fjeld A, Søreide T, Haugerud S. Feasibility study for crossing the sognefjord submerged floating tunnel. *SFT design for crossing of Sognefjorden at Lavik* 2012; .

[4] Moan T, Eidem ME. Floating bridges and submerged tunnels in norway—the history and future outlook. *WCFS2019*. Springer, 2020; 81–111.

[5] Xiang Y, Yang Y. Challenge in design and construction of submerged floating tunnel and state-of-art. *Procedia engineering* 2016; **166**:53–60.

[6] Jakobsen B. Design of the submerged floating tunnel operating under various conditions. *Procedia Engineering* 2010; **4**:71–79.

[7] Lie H, Fu S, Fylling I, Fredriksen AG, Bonnemaire B, Kjersem GL. Numerical modelling of floating and submerged bridges subjected to wave, current and wind. *International Conference on Offshore Mechanics and Arctic Engineering*, vol. 49989, American Society of Mechanical Engineers, 2016; V007T06A075.

[8] Fu S, Moan T, Chen X, Cui W. Hydroelastic analysis of flexible floating interconnected structures. *Ocean engineering* 2007; **34**(11-12):1516–1531.

[9] Michailides C, Loukogeorgaki E, Angelides DC. Response analysis and optimum configuration of a modular floating structure with flexible connectors. *Applied Ocean Research* 2013; **43**:112–130.

[10] Kashiwagi M. A time-domain mode-expansion method for calculating transient elastic responses of a pontoon-type vlfs. *Journal of marine science and technology* 2000; **5**(2):89–100.

[11] Wei W, Fu S, Moan T, Lu Z, Deng S. A discrete-modules-based frequency domain hydroelasticity method for floating structures in inhomogeneous sea conditions. *Journal of Fluids and Structures* 2017; **74**:321–339.

[12] Wei W, Fu S, Moan T, Song C, Ren T. A time-domain method for hydroelasticity of very large floating structures in inhomogeneous sea conditions. *Marine structures* 2018; **57**:180–192.

[13] Wu Y. Hydroelasticity of floating bodies. PhD Thesis, University of Brunel 1984.

[14] Bishop RED, Price WG, Wu Y. A general linear hydroelasticity theory of floating structures moving in a seaway. *Philosophical Transactions of the Royal Society of London. Series A, Mathematical and Physical Sciences* 1986; **316**(1538):375–426.

[15] Kvåle KA, Sigbjörnsson R, Øiseth O. Modelling the stochastic dynamic behaviour of a pontoon bridge: a case study. *Computers & Structures* 2016; **165**:123–135.

[16] Wang S, Ertekin R, van Stiphout A, Ferier P, *et al.*. Hydroelastic-response analysis of a box-like floating airport of shallow draft. *The Fifth International Offshore and Polar Engineering Conference*, International Society of Offshore and Polar Engineers, 1995.

[17] Seif MS, Inoue Y. Dynamic analysis of floating bridges. *Marine structures* 1998; **11**(1-2):29–46.

[18] Li S, Fu S, Wei W, Moan T. A comparison study on the hydroelasticity of two types of floating bridges in inhomogeneous wave conditions. *International Conference on Offshore Mechanics and Arctic Engineering*, vol. 51265, American Society of Mechanical Engineers, 2018; V07AT06A045.

[19] Wei W, Fu S, Moan T, Song C, Deng S, Lie H. A time-domain method for hydroelasticity of a curved floating bridge in inhomogeneous waves. *Journal of Offshore Mechanics and Arctic Engineering* 2019; **141**(1).

[20] Cheng Z, Gao Z, Moan T. Wave load effect analysis of a floating bridge in a fjord considering inhomogeneous wave conditions. *Engineering Structures* 2018; **163**:197–214.

[21] Cheng Z, Gao Z, Moan T. Hydrodynamic load modeling and analysis of a floating bridge in homogeneous wave conditions. *Marine Structures* 2018; **59**:122–141.

[22] Kunisu H. Evaluation of wave force acting on submerged floating tunnels. *Procedia Engineering* 2010; **4**:99–105.

[23] Kunisu H, Mizuno S, Mizuno Y, Saeki H, *et al.*. Study on submerged floating tunnel characteristics under the wave condition. *The Fourth International Offshore and Polar Engineering Conference*, International Society of Offshore and Polar Engineers, 1994.

[24] Chen Z, Xiang Y, Lin H, Yang Y. Coupled vibration analysis of submerged floating tunnel system in wave and current. *Applied Sciences* 2018; **8**(8):1311.

[25] Wu X, Ge F, Hong Y. Effect of travelling wave on vortex-induced vibrations of submerged floating tunnel tethers. *Procedia Engineering* 2010; **4**:153–160.

[26] Fei G, Man-sheng D, Lei H, You-shi H. Vortex-induced vibration of submerged floating tunnel tethers under wave and current effects [j]. *Engineering Mechanics* 2006; **23**(S1):217–221.

[27] Yiqiang X, Chunfeng C. Vortex-induced dynamic response analysis for the submerged floating tunnel system under the effect of currents. *Journal of waterway, port, coastal, and ocean engineering* 2013; **139**(3):183–189.

[28] Cheng Z, Svangstu E, Gao Z, Moan T. Field measurements of inhomogeneous wave conditions in bjørnafjorden. *Journal of Waterway, Port, Coastal, and Ocean Engineering* 2019; **145**(1):05018 008.

[29] Veritas DN. Dnv-rp-c205 environmental conditions and environmental loads. *Det Norske Veritas: Oslo, Norway* 2010; .

[30] SVV. Design basis metocean. *Norway:Statens Vegnesen* 2016; .

[31] Deng S, Fu S, Moan T, Wei W, Gao Z. Hydro-elastic analysis of a floating bridge in waves considering the effect of the hydrodynamic coupling and the shore sides. *International Conference on Offshore Mechanics and Arctic Engineering*, vol. 51203, American Society of Mechanical Engineers, 2018; V001T01A039.

[32] DNV G. Enviromental conditions and enviromental loads (dnv-rp-c205). *Det Norske Veritas AS, Oslo, Norway* 2014; **600**.

[33] Fredsoe J, Sumer BM. *Hydrodynamics around cylindrical structures*, vol. 12. World Scientific, 1997.

[34] Gerrard J. The mechanics of the formation region of vortices behind bluff bodies. *Journal of fluid mechanics* 1966; **25**(2):401–413.

[35] Williamson C. Oblique and parallel modes of vortex shedding in the wake of a circular cylinder at low reynolds numbers. *Technical Report*, CALIFORNIA INST OF TECH PASADENA GRADUATE AERONAUTICAL LABS 1989.

[36] Lucor D, Foo J, Karniadakis G. Vortex mode selection of a rigid cylinder subject to viv at low mass-damping. *Journal of Fluids and Structures* 2005; **20**(4):483–503.

[37] Blevins RD. Flow-induced vibration. *vnr* 1977; .

[38] Achenbach E, Heinecke E. On vortex shedding from smooth and rough cylinders in the range of reynolds numbers 6× 10 3 to 5× 10 6. *Journal of fluid mechanics* 1981; **109**:239–251.

[39] Roshko A. Experiments on the flow past a circular cylinder at very high reynolds number. *Journal of fluid mechanics* 1961; **10**(3):345–356.

[40] Schewe G. On the force fluctuations acting on a circular cylinder in crossflow from subcritical up to transcritical reynolds numbers. *Journal of fluid mechanics* 1983; **133**:265–285.

[41] Hallam M, Heaf N, Wootton LR. Dynamics of marine structures: methods of calculating the dynamic response of fixed structures subject to wave and current action. *Technical Report* 1977.

[42] Williamson C, Govardhan R. A brief review of recent results in vortex-induced vibrations. *Journal of Wind engineering and industrial Aerodynamics* 2008; **96**(6-7):713–735.

[43] Sarpkaya T. A critical review of the intrinsic nature of vortex-induced vibrations. *Journal of fluids and structures* 2004; **19**(4):389–447.

[44] Griffin O, Ramberg S. Some recent studies of vortex shedding with application to marine tubulars and risers 1982; .

[45] Khalak A, Williamson CH. Investigation of relative effects of mass and damping in vortex-induced vibration of a circular cylinder. *Journal of Wind Engineering and Industrial Aerodynamics* 1997; **69**:341–350.

[46] Brika D, Laneville A. Vortex-induced vibrations of a long flexible circular cylinder. *Journal of Fluid Mechanics* 1993; **250**:481–481.

[47] Brika D, Laneville A. An experimental study of the aeolian vibrations of a flexible circular cylinder at different incidences. *Journal of fluids and structures* 1995; **9**(4):371–391.

[48] Lighthill J, *et al.*. Waves and hydrodynamic loading 1979; .

[49] Lighthill J, *et al.*. Fundamentals concerning wave loading on offshore structures. *Journal of Fluid Mechanics* 1986; **173**(667-681):71.

[50] Sarpkaya T. Vortex-induced oscillations: a selective review 1979; .

[51] Bearman PW. Vortex shedding from oscillating bluff bodies. *AnRFM* 1984; **16**:195–222.

[52] Blevins R. Flow-induced vibrations van nostrand reinhold. *New York* 1990; .

[53] Lu Z, Fu S, Zhang M, Ren H, Song L. A non-iterative method for vortex induced vibration prediction of marine risers. *International Conference on Offshore Mechanics and Arctic Engineering*, vol. 57649, American Society of Mechanical Engineers, 2017; V002T08A028.

[54] Govardhan R, Williamson C. Modes of vortex formation and frequency response of a freely vibrating cylinder. *Journal of Fluid Mechanics* 2000; **420**:85–130.

[55] Vikestad K. *Multi-frequency response of a cylinder subjected to vortex shedding and support motions*. Norwegian University of Science and Technology Trondheim, 1998.

[56] Vickery B, Watkins R. Flow-induced vibrations of cylindrical structures. *Hydraulics and Fluid Mechanics*. Elsevier, 1964; 213–241.

[57] Skop RA, Griffin OM, *et al.*. An heuristic model for determining flow-induced vibration of offshore structure. *Offshore Technology Conference*, Offshore Technology Conference, 1973.

[58] Griffin OM, Ramberg SE. The vortex-street wakes of vibrating cylinders. *Journal of Fluid Mechanics* 1974; **66**(3):553–576.

[59] Sarpkaya T. Fluid forces on oscillating cylinders. *STIA* 1978; **104**:275–290.

[60] Sarpkaya T. Offshore hydrodynamics 1993; .

[61] Griffin O. Vortex-excited cross-flow vibrations of a single cylindrical tube 1980; .

[62] Griffin OM, Skop RA, Ramberg SE, *et al.*. The resonant, vortex-excited vibrations of structures and cable systems. *Offshore Technology Conference*, Offshore Technology Conference, 1975.

[63] Wang E, Xiao Q, Zhu Q, Incecik A. The effect of spacing on the vortex-induced vibrations of two tandem flexible cylinders. *Physics of Fluids* 2017; **29**(7):077 103.

[64] White F, Mechanics F. Chapter 6: Viscous flow in ducts. *Fluid Mechanics* 2008; **382391**.

[65] Guilmineau E, Queutey P. Numerical simulation in vortex-induced vibrations at low mass-damping. *15th AIAA Computational Fluid Dynamics Conference*, 2001; 2852.

[66] Michelassi V, Wissink J, Frohlich J, Rodi W. Large-eddy simulation of flow around low-pressure turbine blade with incoming wakes. *AIAA journal* 2003; **41**(11):2143–2156.

[67] Grinstein FF, Karniadakis GE. Alternative les and hybrid rans/les for turbulent flows. *J. Fluids Eng.* 2002; **124**(4):821–822.

[68] Travin A, Shur M, Strelets M, Spalart P. Detached-eddy simulations past a circular cylinder. *Flow, turbulence and combustion* 2000; **63**(1-4):293–313.

[69] Constantinides Y, Oakley Jr OH. Numerical prediction of bare and straked cylinder viv. *International Conference on Offshore Mechanics and Arctic Engineering*, vol. 47497, 2006; 745–753.

[70] Versteeg HK, Malalasekera W. *An introduction to computational fluid dynamics: the finite volume method*. Pearson education, 2007.

[71] Lucor D, Foo J, Karniadakis G. Correlation length and force phasing of a rigid cylinder subject to viv. *IUTAM Symposium on Integrated Modeling of Fully Coupled Fluid Structure Interactions Using Analysis, Computations and Experiments*, Springer, 2003; 187–199.

[72] Bishop RED, Hassan A. The lift and drag forces on a circular cylinder oscillating in a flowing fluid. *Proceedings of the Royal Society of London. Series A. Mathematical and Physical Sciences* 1964; **277**(1368):51–75.

[73] Gopalkrishnan R. Vortex-induced forces on oscillating bluff cylinders. *Technical Report*, WOODS HOLE OCEANOGRAPHIC INSTITUTION MA 1993.

[74] Hover F, Miller S, Triantafyllou M. Vortex-induced vibration of marine cables: experiments using force feedback. *Journal of fluids and structures* 1997; **11**(3):307–326.

[75] Hover F, Techet A, Triantafyllou M. Forces on oscillating uniform and tapered cylinders in a crossflow 1998; .

[76] Carberry J, Sheridan J, Rockwell D. Controlled oscillations of a cylinder: forces and wake modes. *Journal of Fluid Mechanics* 2005; **538**:31.

[77] Triantafyllou M, Triantafyllou G, Tein Y, Ambrose BD, *et al.*. Pragmatic riser viv analysis. *Offshore technology conference*, Offshore Technology Conference, 1999.

[78] Vandiver J, Li L. Shear7 program theory manual. *Department of Ocean Engineering, MIT, Boston, USA* 1999; .

[79] Larsen CM, Vikestad K, Yttervik R, Passano E, Baarholm G. Vivana theory manual. *Marintek, Trondheim, Norway* 2001; .

[80] Zhang M, Fu S, Ren H, Li R, Song L. A time domain prediction method for vortex-induced vibrations of a flexible pipe with time-varying tension. *International Conference on Offshore Mechanics and*

*Arctic Engineering*, vol. 51210, American Society of Mechanical Engineers, 2018; V002T08A054.

[81] Venugopal M. Damping and response prediction of a flexible cylinder in a current. PhD Thesis, Massachusetts Institute of Technology 1996.

[82] Thorsen MJ, Sævik S, Larsen CM. A simplified method for time domain simulation of cross-flow vortex-induced vibrations. *Journal of Fluids and Structures* 2014; **49**:135–148.

[83] Thorsen MJ, Sævik S, Larsen CM. Time domain simulation of vortex-induced vibrations in stationary and oscillating flows. *Journal of Fluids and Structures* 2016; **61**:1–19.

[84] Ulveseter JV, Sævik S, Larsen CM. Time domain model for calculation of pure in-line vortex-induced vibrations. *Journal of Fluids and Structures* 2017; **68**:158–173.

[85] Thorsen MJ, Sævik S, Larsen CM. Non-linear time domain analysis of cross-flow vortex-induced vibrations. *Marine Structures* 2017; **51**:134–151.

[86] Lu Z, Fu S, Zhang M, Ren H, Song L. A modal space based direct method for vortex-induced vibration prediction of flexible risers. *Ocean Engineering* 2018; **152**:191–202.

[87] Ulveseter JV, Thorsen MJ, Sævik S, Larsen CM. Time domain simulation of riser viv in current and irregular waves. *Marine Structures* 2018; **60**:241–260.

[88] Mainçon P. A wiener-laguerre model of viv forces given recent cylinder velocities. *Mathematical Problems in Engineering* 2011; **2011**.

[89] Mainc̦on P, Larsen CM. Towards a time-domain finite element analysis of vortex induced vibrations. *International Conference on Offshore Mechanics and Arctic Engineering*, vol. 44397, 2011; 415–425.

[90] Facchinetti ML, De Langre E, Biolley F. Coupling of structure and wake oscillators in vortex-induced vibrations. *Journal of Fluids and structures* 2004; **19**(2):123–140.

[91] Igarashi T. Characteristics of the flow around two circular cylinders arranged in tandem: 2nd report, unique phenomenon at small spacing. *Bulletin of JSME* 1984; **27**(233):2380–2387.

[92] Zhou Y, Yiu M. Flow structure, momentum and heat transport in a two-tandem-cylinder wake. *Journal of Fluid Mechanics* 2006; **548**:17–48.

[93] Xu G, Zhou Y. Strouhal numbers in the wake of two inline cylinders. *Experiments in Fluids* 2004; **37**(2):248–256.

[94] Igarashi T. Characteristics of the flow around two circular cylinders arranged in tandem: 1st report. *Bulletin of JSME* 1981; **24**(188):323–331.

[95] Fu S, Wang J, Baarholm R, Wu J, Larsen C. Features of vortex-induced vibration in oscillatory flow. *Journal of Offshore Mechanics and Arctic Engineering* 2014; **136**(1).

[96] Voie P, Wu J, Larsen C, Resvanis T, Vandiver J, Triantafyllou M. Consolidated guideline on analysis of vortex-induced vibrations in risers and umbilicals. *ASME Paper No. OMAE2017-61362* 2017; .

[97] Jung-Chi L. Vortex-induced vibration of slender structures in unsteady flow. *Cambridge, USA: Massachusetts Institute of Technology* 2002; .

[98] Chang SHM, Isherwood M, *et al.*. Vortex-induced vibrations of steel catenary risers and steel offloading lines due to platform heave motions. *Offshore technology conference*, Offshore Technology Conference, 2003.

[99] Wang J, Fu S, Baarholm R. Evaluation of vortex-induced vibration of a steel catenary riser in steady current and vessel motion-induced oscillatory current. *Journal of Fluids and Structures* 2018; **82**:412–431.

[100] Ren H, Cheng J, Zhang M, Cao P, Fu S. Experimental investigation on the hydrodynamic responses and coefficients of straked flexible pipe in oscillatory flow. *International Conference on Offshore Mechanics and Arctic Engineering*, vol. 51210, American Society of Mechanical Engineers, 2018; V002T08A059.

[101] Fu S, Xu Y, Hu K, Zhang Y. Experimental investigation on hydrodynamics of floating cylinder in oscillatory and steady flows by forced oscillation test. *Marine structures* 2013; **34**:41–55.

[102] Wang J, Fu S, Wang J, Li H, Ong MC. Experimental investigation on vortex-induced vibration of a free-hanging riser under vessel motion and uniform current. *Journal of Offshore Mechanics and Arctic Engineering* 2017; **139**(4).

[103] Lee T, Basu S. Nonintrusive measurements of the boundary layer developing on a single and two circular cylinders. *Experiments in fluids* 1997; **23**(3):187–192.

[104] Kostić ŽG, Oka S. Fluid flow and heat transfer with two cylinders in cross flow. *International journal of heat and mass transfer* 1972; **15**(2):279–299.

[105] Aiba S, Yamazaki Y. An experimental investigation of heat transfer around a tube in a bank 1976; .

[106] Hiwada M, Mabuchi I, Yanagihara H. Fluid flow and heat transfer around two circular cylinders. *Bulletin of JSME* 1982; **25**(209):1737–1745.

[107] Nishimura T, Ohori Y, Kawamura Y. Flow pattern and rate of mass transfer around two cylinders in tandem. *Int. Chem. Eng.* 1986; **26**(1):123–129.

[108] Sharman B, Lien FS, Davidson L, Norberg C. Numerical predictions of low reynolds number flows over two tandem circular cylinders. *International Journal for Numerical Methods in Fluids* 2005; **47**(5):423–447.

[109] Farrant T, Tan M, Price W. A cell boundary element method applied to laminar vortex-shedding from arrays of cylinders in various arrangements. *Journal of Fluids and Structures* 2000; **14**(3):375–402.

[110] Papaioannou GV, Yue DK, Triantafyllou MS, Karniadakis GE. Three-dimensionality effects in flow around two tandem cylinders. *Journal of Fluid Mechanics* 2006; **558**:387–413.

[111] Kitagawa T, Ohta H. Numerical investigation on flow around circular cylinders in tandem arrangement at a subcritical reynolds number. *Journal of Fluids and Structures* 2008; **24**(5):680–699.

[112] Zdravkovich M. The effects of interference between circular cylinders in cross flow. *Journal of fluids and structures* 1987; **1**(2):239–261.

[113] Carmo B, Meneghini J, Sherwin S. Possible states in the flow around two circular cylinders in tandem with separations in the vicinity of the drag inversion spacing. *Physics of Fluids* 2010; **22**(5):054 101.

[114] Carmo BS, Meneghini JR, Sherwin SJ, *et al.*. Secondary instabilities in the flow around two circular cylinders in tandem. *Journal of Fluid Mechanics* 2010; **644**(1):395–431.

[115] Lin JC, Yang Y, Rockwell D. Flow past two cylinders in tandem: instantaneous and averaged flow structure. *Journal of Fluids and Structures* 2002; **16**(8):1059–1071.

[116] Ishigai S, Nishikawa E, Nishimura K, Cho K. Experimental study on structure of gas flow in tube banks with tube axes normal to flow: Part 1, karman vortex flow from two tubes at various spacings. *Bulletin of JSME* 1972; **15**(86):949–956.

[117] Alam MM, Zhou Y. Phase lag between vortex shedding from two tandem bluff bodies. *Journal of fluids and structures* 2007; **23**(2):339–347.

[118] Ljungkrona L, Norberg C, Sunden B. Free-stream turbulence and tube spacing effects on surface pressure fluctuations for two tubes in an in-line arrangement. *Journal of Fluids and Structures* 1991; **5**(6):701–727.

[119] Zdravkovich M. Flow induced oscillations of two interfering circular cylinders. *Journal of Sound and Vibration* 1985; **101**(4):511–521.

[120] Hetz A, Dhaubhadel M, Telionis D. Vortex shedding over five in-line cylinders cylinders. *Journal of fluids and structures* 1991; **5**(3):243–257.

[121] Meneghini J, Saltara F, Siqueira C, Ferrari J. Numerical simulation of flow interference between two circular cylinders in tandem and side-by-side arrangements. *Journal of fluids and structures* 2001; **15**(2):327–350.

[122] Ljungkrona L, Sundén B. Flow visualization and surface pressure measurement on two tubes in an inline arrangement. *Experimental thermal and fluid science* 1993; **6**(1):15–27.

[123] Lee T, Panagakos A. Investigation of boundary layer behavior on single and tandem cylinders. *International Symposium on Fluid-Structure Interactions, Aeroelasticity, Flow-Induced Vibration and Noise, 4 th, Dallas, TX*, 1997; 103–112.

[124] Alam MM, Moriya M, Takai K, Sakamoto H. Fluctuating fluid forces acting on two circular cylinders in a tandem arrangement at a subcritical reynolds number. *Journal of Wind Engineering and Industrial Aerodynamics* 2003; **91**(1-2):139–154.

[125] Zdravkovich M. Review of flow interference between two circular cylinders in various arrangements 1977; .

[126] Kiya M, Arie M, Tamura H, Mori H. Vortex shedding from two circular cylinders in staggered arrangement 1980; .

[127] Ohya Y. Wake interference and vortex shedding. *Ency. Fluid Mech.* 1989; :323–389.

[128] King R, Johns D. Wake interaction experiments with two flexible circular cylinders in flowing water. *Journal of Sound and Vibration* 1976; **45**(2):259–283.

[129] Bokaian A, Geoola F. Proximity-induced galloping of two interfering circular cylinders. *Journal of Fluid Mechanics* 1984; **146**:417–449.

[130] Bokaian A, Geoola F. Wake-induced galloping of two interfering circular cylinders. *Journal of Fluid Mechanics* 1984; **146**:383–415.

[131] Ruscheweyh H. Aeroelastic interference effects between slender structures. *Journal of Wind Engineering and Industrial Aerodynamics* 1983; **14**(1-3):129–140.

[132] Kim S, Alam MM, Sakamoto H, Zhou Y. Flow-induced vibrations of two circular cylinders in tandem arrangement. part 1: Characteristics of vibration. *Journal of Wind Engineering and Industrial Aerodynamics* 2009; **97**(5-6):304–311.

[133] Huera-Huarte F, Bearman P. Vortex and wake-induced vibrations of a tandem arrangement of two flexible circular cylinders with near wake interference. *Journal of Fluids and Structures* 2011; **27**(2):193–211.

[134] Huera-Huarte F, Gharib M. Vortex-and wake-induced vibrations of a tandem arrangement of two flexible circular cylinders with far wake interference. *Journal of Fluids and Structures* 2011; **27**(5-6):824–828.

[135] Qin B, Alam MM, Zhou Y. Free vibrations of two tandem elastically mounted cylinders in crossflow. *Journal of Fluid Mechanics* 2019; **861**:349–381.

[136] Chen HC, Chen CR, Huang K, *et al.*. Cfd simulation of vortex-induced and wake-induced vibrations of dual vertical risers. *The Twenty-third International Offshore and Polar Engineering Conference*, International Society of Offshore and Polar Engineers, 2013.

[137] Leonard A, Roshko A. Aspects of flow-induced vibration. *Journal of Fluids and Structures* 2001; **15**(3-4):415–425.

[138] Zdravkovich MM. *Flow around circular cylinders: Volume 2: Applications*, vol. 2. Oxford university press, 1997.

[139] Ersdal S. An experimental study of hydrodynamic forces on cylinders and cables in near axial flow 2004; .

[140] Stansby P. The effects of end plates on the base pressure coefficient of a circular cylinder. *The Aeronautical Journal* 1974; **78**(757):36–37.

[141] Zhao J, Leontini JS, Jacono DL, Sheridan J. Fluid–structure interaction of a square cylinder at different angles of attack. *Journal of Fluid Mechanics* 2014; **747**:688–721.

[142] Vijay K, Srinil N, Zhu H, Bao Y, Zhou D, Han Z. Flow-induced transverse vibration of an elliptical cylinder with different aspect ratios. *Ocean Engineering* 2020; **214**:107 831.

[143] Wang J, Fu S, Baarholm R, Wu J, Larsen CM. Fatigue damage induced by vortex-induced vibrations in oscillatory flow. *Marine Structures* 2015; **40**:73–91.

# Appendix A

# Calibration of force sensors and springs

## A.1 Calibration of force sensor

In the self-oscillation test, two single component force sensors were set up at each end of the two cylinders, as shown in Fig. A.1. They were calibrated in CF and IL directions, respectively. Fig. A.2 shows the calibration methods. Several given mass were used, as Table. A.1 and A.2 shown. The factors I and II (gradient of the trending line between 'Weight' and 'Data of Sensor') were used to get the forces in the test.

In this force sensor calibration, the IL or CF forces were applied at the middle point of the cylinders and the sum of the forces measured at the two ends ($F_I + F_{II}$) representing the total force. Moreover, by the sensor arrangement, the force variation along the cylinder could be initially discussed. The identical measured force at the two ends represent a even variation of the drag/lift force along the cylinder, vice verse. To obtain 2-dimensional results of VIV features, the force difference between the two ends of the cylinder should be checked in the post-processing.

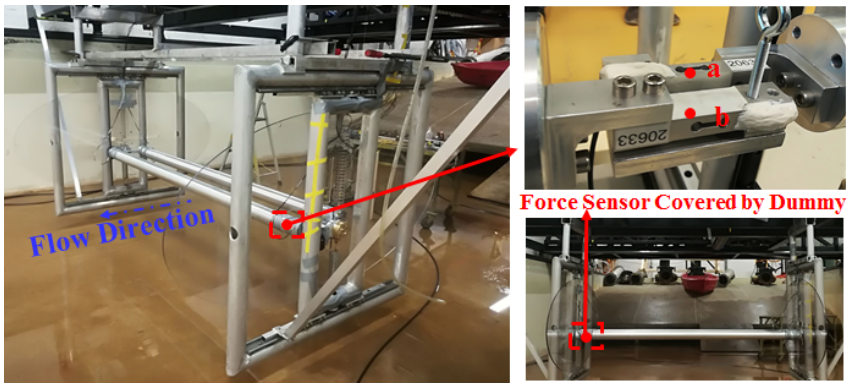


*Figure A.1: Force sensor arrangement at both ends of the each cylinder, (a) is for IL drag force, (b) is for CF lift force.*

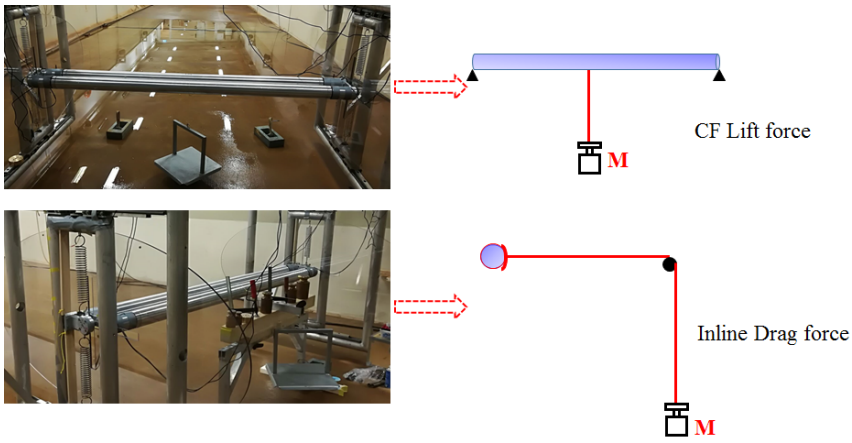


*Figure A.2: Calibration methods for IL drag and CF lift forces.*

*Table A.1: Calibration result for CF lift force.*

| Given Mass [$kg$[ | Weight [$N$] | Data of Sensor (I) [-] | Data of Sensor (II) [-] | Factor I [-] | Factor II [-] |
|---|---|---|---|---|---|
| 2 | 9.8 | 0.5209 | 0.4290 | | |
| 5 | 49 | 0.7866 | 0.7068 | | |
| 20 | 196 | 1.7851 | 1.7530 | 147 | 140.85 |
| 25 | 245 | 2.1225 | 2.0946 | | |
| 40 | 392 | 3.1200 | 3.1435 | | |

*Table A.2: Calibration result for IL drag force.*

| Given mass $[kg]$ | Weight $[N]$ | Data of sensor (I) [-] | Data of sensor (II) [-] | Factor I | Factor II |
|---|---|---|---|---|---|
| 1 | 9.8 | 0.4625 | 0.5186 | 147.84 | 147.21 |
| 5 | 49 | 0.7302 | 0.7911 | | |
| 20 | 196 | 1.7252 | 1.7831 | | |
| 25 | 245 | 2.0544 | 2.1204 | | |

## A.2 Calibration of spring

In the self-oscillation test, two groups of the springs were equipped on the support frame to provide the restoring force for the cylinder model, as shown in Fig. 3.5 and 3.6. The stiffness of the springs were tested before setup, as shown in Fig. A.3 and Table. A.3.

Two types of springs were used to provide the restoring force for single- and twin-cylinder model.

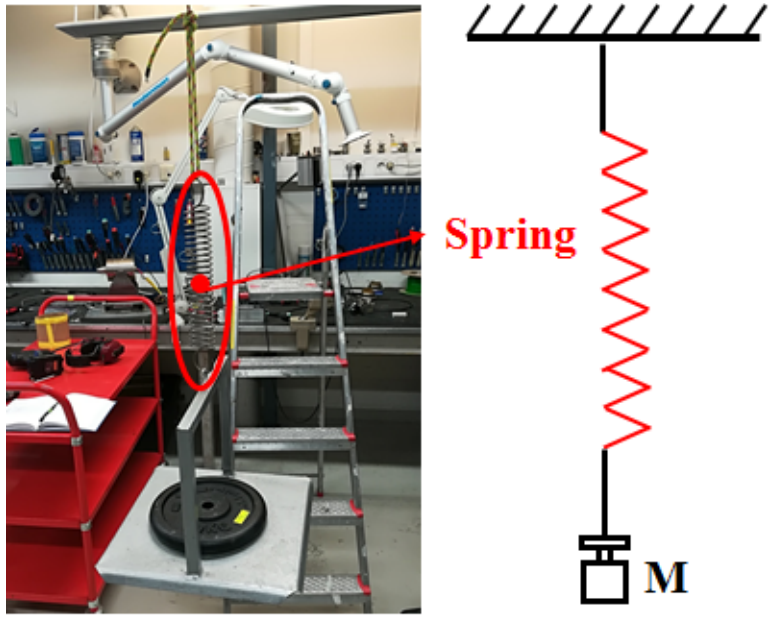


*Figure A.3: Calibration of the spring.*

*Table A.3: Calibration result for springs.*

| | | | | | | | |
|---|---|---|---|---|---|---|---|
| Type I | Mass [kg] | 0 | 1 | 5 | 20 | 25 | 40 |
| | Length [m] | 0.15 | 0.181 | 0.304 | 0.767 | 0.922 | 1.395 |
| | Stiffness [N/m] | k1=317.5 | | | | | |
| Type II | Mass [kg] | 0 | 1 | 5 | 20 | 25 | 40 |
| | Length [m] | 0.1 | 0.116 | 0.180 | 0.420 | 0.500 | 0.740 |
| | Stiffness [N/m] | k2=612.5 | | | | | |

# Appendix B

# Measurement of friction damping induced by the crossflow motion guiding tracks

In the self-oscillation test, the twin-cylinder model was mounted between two support frames, and a pair of low-friction tracks was mounted on one side of each frame to guide the crossflow motion, shown in Fig. B.1. During the test, the frames were towed in the tank with various speeds to get our designed reduced velocity. Besides CF lift force, the IL drag force could be different from case to case by the towing velocities as termed in Eq. B.1.

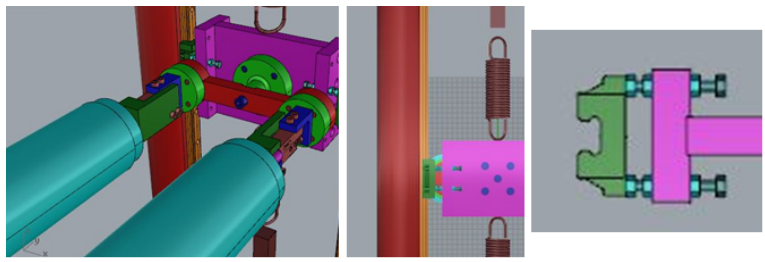

*Figure B.1: Low-friction track on the frame, and it is connected to the oscillation system by a slider.*

$$F_D = \frac{1}{2}\rho C_D D l U^2 \tag{B.1}$$

where $\rho$, $C_D$, $D$ and $l$ are the fluid density, drag coefficient, cylinder diameter and length; $U$ is the flow velocity, ranging from $0.1 - 1m/s$ in the test. Different IL drag forces acing on the cylinders induced various normal forces on the sliders, which might affect the friction and structural damping of the test setup. Therefore, before self-oscillation test, a series of tack friction tests were conduced in terms of the normal force, as shown in Fig B.2. During the test, a $weight(M)$ was used to drive the slider moving along the track under different normal forces. Motion of the slider was recorded by a draw-wire displacement sensor with the resolution of $10^{-4}m$ and sampling frequency of $50Hz$.

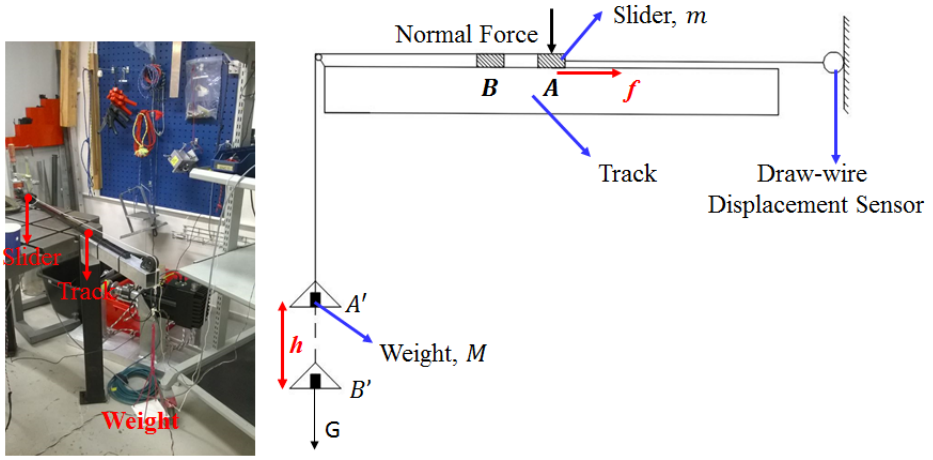


*Figure B.2: Test setup for measuring track friction.*

Two typical methods were adopted here to manage the friction, i.e.'mechanical method' and 'energy method'.

In the mechanical method, three positions $P_1, P_2, P_3$ and the the time step $dt = \frac{1}{50Hz} = 0.02s$ were required. Two distance and the corresponding velocities, acceleration can be obtained by,

$$\begin{cases} s_1 = P_2 - P_1 \\ s_2 = P_3 - P_2 \\ v_1 = s_1/dt \\ v_2 = s_2/dt \\ a = \frac{v_2 - v_1}{dt} \end{cases} \tag{B.2}$$

Then the friction force of the track-slider system ($f$) can be easily calculated,

$$f = Mg - (M + m)\, a \tag{B.3}$$

where $M$ is the mass of *weight* driving the motion, $m$ is the mass of the slider, as shown in Fig. B.2.

For the energy method, the energy provided by the gravity of the *weight* during a test period is,

$$E_G = Mgh \tag{B.4}$$

The corresponding momentum increase of the *slider* and *weight* can be obtained by,

$$E_M = \frac{1}{2}(M+m)\left(v_1^2 - v_0^2\right) \tag{B.5}$$

$v_0$ and $v_1$ are the velocities at the initial and terminal positions. Then, the friction can be obtained based on the energy conservation,

$$f = \frac{E_G - E_M}{h} = Mg - \frac{1}{2h}(M+m)\left(v_1^2 - v_0^2\right) \tag{B.6}$$

Normal force on the slider was provided by given mass. Firstly, the reliability of the friction measuring procedure was discussed by the above two methods and a given mass of $2kg$. Table. B.1 shows the comparison result, and the small difference reveals the reliability of the friction testing method.

Results with several given mass (different normal forces on the slider) are listed in Table. B.2, it illustrates that the friction has weak relation with the normal force and the structural damping in the self-oscillation test are constant when the positive normal force is provided by the cylinder drag.

In the self-oscillation test, IL drag force acting on the cylinders are time-various. In this fraction test, constant normal forces are applied, however, the mean drag force is predominant and the present result could be a reference on the structural damping of the oscillation system.

*Table B.1: Friction obtained by different methods.*

| Mechanical Method | M | m | a | $f$ | Difference |
|---|---|---|---|---|---|
| | $[kg]$ | $[kg]$ | $[m/s]$ | $[N]$ | $\frac{\lvert f_M - f_E \rvert}{f_M}$ |
| | 2 | 0.5 | 1.8397 | 15.17 | |
| | v0 | v1 | h | $f$ | |
| Energy Method | $[m/s]$ | $[m/s]$ | $[m]$ | $[N]$ | 1.4% |
| | 0.2980 | 0.9235 | 0.215775 | 15.33 | |

*Table B.2: Friction with normal forces.*

| Mass $[kg]$ | 2 | 4 | 6 | 8 | 10 | 15 |
|---|---|---|---|---|---|---|
| $f$ $[N]$ | 15.17 | 15.68 | 15.69 | 15.82 | 15.58 | 15.91 |

# Appendix C

# Typical time series of the forces and oscillations in self-oscillation test

Oscillation displacement was measured by a draw-wire displacement sensor at each end of single cylinder or twin-cylinder model, similar as the force measurement discussed in Appendix.A.

Typical time series of the oscillation displacement and the measured CF lift forces are presented in this part. All the data shown here are the original records, meaning that the lift force includes the vortex-induced and inertial components. Fig. C.1 and C.2 show the result of a single cylinder, while Fig. C.3, C.4, C.5, C.5, C.7 and C.8 represent the oscillations and forces for twin cylinders with $\lambda = 2$ $U_r = 4.5$, $\lambda = 3$ $U_r = 5.5$ and $\lambda = 4$ $U_r = 4.5$.

It is clearly seen that the measured oscillation displacements and CF lift forces at the two ends are identical to each other. This phenomenon illustrates that this self-oscillation test is 2-dimensional and each cross-section of the cylinder is independent from the adjacent ones.

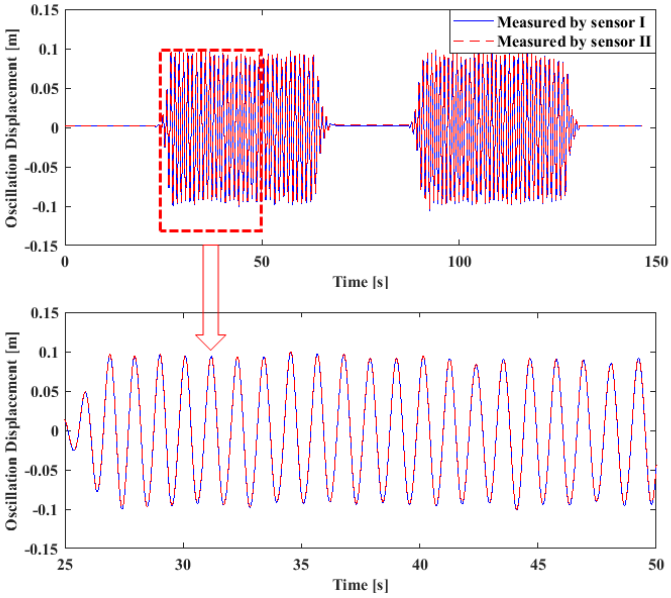


*Figure C.1: Time series of oscillation displacement for a single cylinder* $U_r = 5.0$

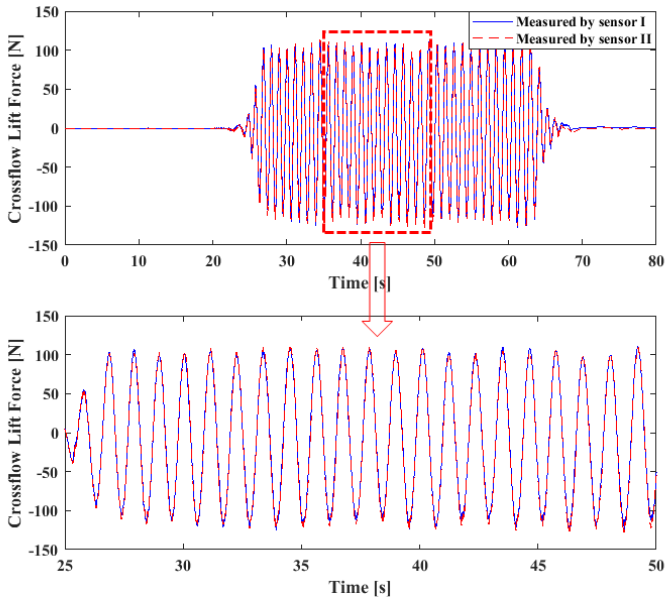


*Figure C.2: Time series of crossflow lift force for a single cylinder* $U_r = 5.0$

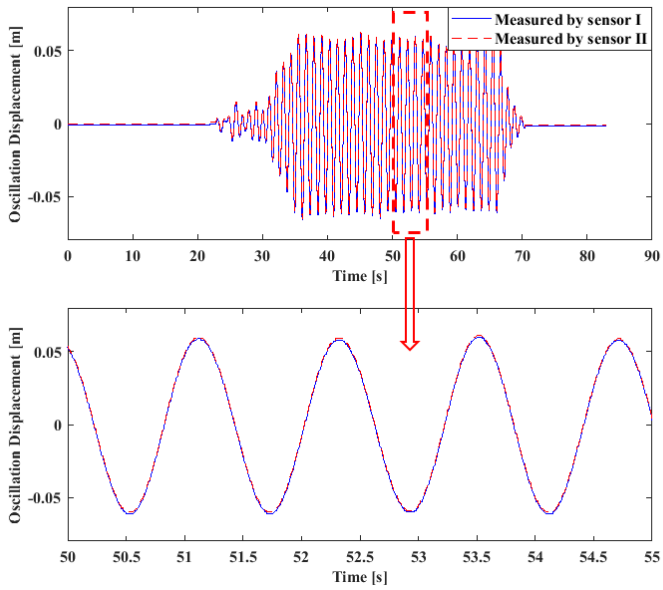


*Figure C.3: Time series of oscillation displacement for a Twin-cylinder,* $\lambda = 2.0$ *and* $U_r = 4.5$

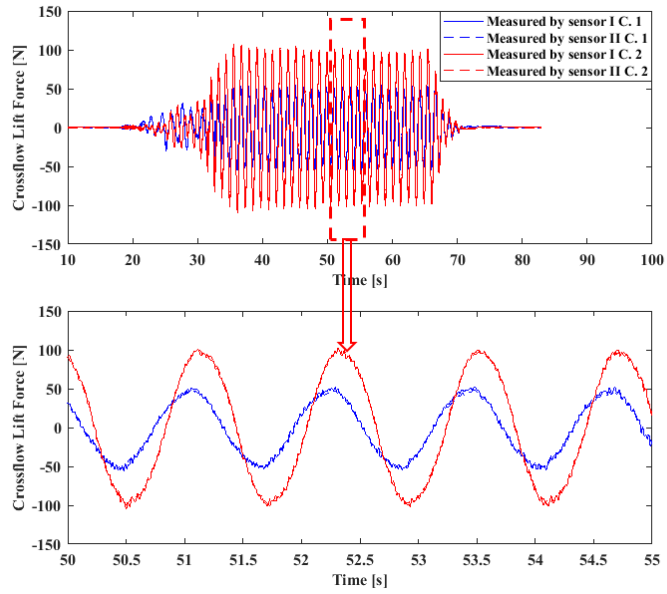


*Figure C.4: Time series of crossflow lift force for a Twin-cylinder,* $\lambda = 2.0$ *and* $U_r = 4.5$

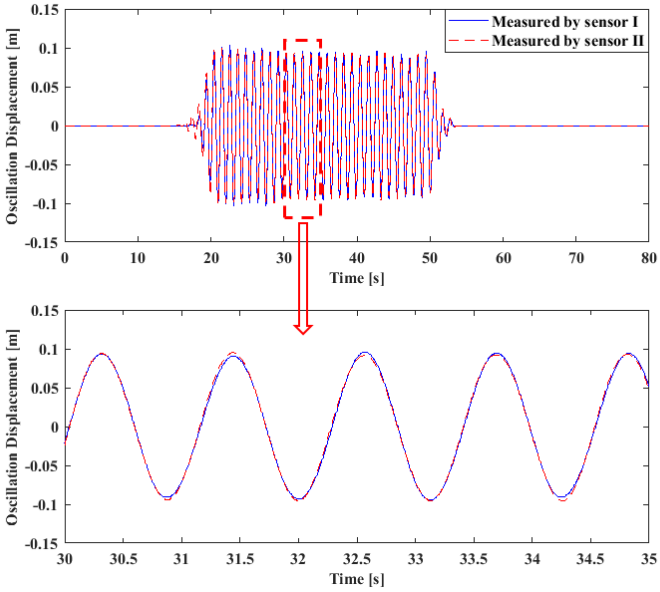


*Figure C.5: Time series of oscillation displacement for a Twin-cylinder,* $\lambda = 3.0$ *and* $U_r = 5.5$

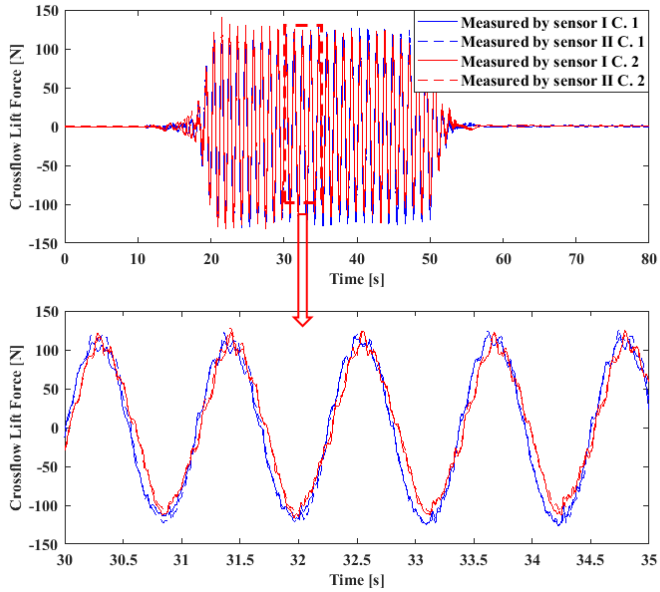


*Figure C.6: Time series of crossflow lift force for a Twin-cylinder,* $\lambda = 3.0$ *and* $U_r = 5.5$

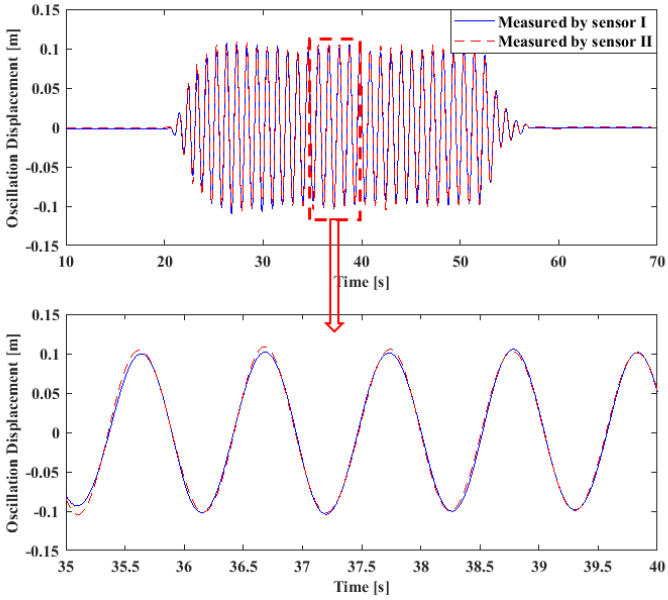


*Figure C.7: Time series of oscillation displacement for a Twin-cylinder,* $\lambda = 4.0$ *and* $U_r = 4.5$

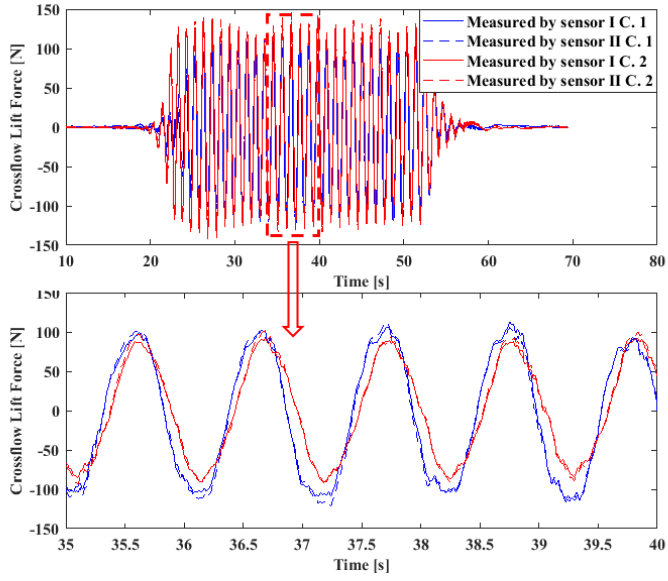


*Figure C.8: Time series of crossflow lift force for a Twin-cylinder,* $\lambda = 4.0$ *and* $U_r = 4.5$

# Appendix D

# Appended Papers

## D.1 Paper 1

**Paper 1:**
Deng S, Ren H, Xu Y, Fu S, Moan T, Gao Z. Experimental Study of Vortex-Induced Vibration of a Twin-tube Submerged Floating Tunnel Segment Model.*Journal of Fluids and Structures* 2020; **94**(3):102908.

Journal of Fluids and Structures 94 (2020) 102908

Contents lists available at ScienceDirect

Journal of Fluids and Structures

journal homepage: www.elsevier.com/locate/jfs

# Experimental study of vortex-induced vibration of a twin-tube submerged floating tunnel segment model

Shi Deng [a], Haojie Ren [b,c], Yuwang Xu [b,c,*], Shixiao Fu [a,b,c], Torgeir Moan [a,d], Zhen Gao [a,d]

[a] Department of Marine Technology, NTNU, NO-7491 Trondheim, Norway
[b] State Key Laboratory of Ocean Engineering, Shanghai Jiao Tong University, Shanghai, 200030, China
[c] Collaborative Innovation Centre for Advanced Ship and Deep-Sea Exploration, Shanghai, 200240, China
[d] Centre for Ships and Ocean Structures, NTNU, Marine Technology Centre, NO-7491 Trondheim, Norway

ARTICLE INFO

*Article history:*
Received 14 May 2019
Received in revised form 23 January 2020
Accepted 6 February 2020
Available online 26 February 2020

*Keywords:*
Submerged floating tunnel
Vortex-induced vibration
Response amplitude
Lift force
Torsional moment

ABSTRACT

The cross-flow vortex-induced vibration features of a submerged floating tunnel element, which is composed of two rigidly connected cylinders in a tandem configuration, were investigated via a self-oscillation model test in a steady flow. The Reynolds number ranged from $2\times10^4$ to $9\times10^4$, and the ratio of the center-to-center distance between the two cylinders and cylinder diameter varied within a range of 2-4. The vortex induced vibration responses and lift forces on the up- and downstream cylinders were studied under different spacing ratios and compared with those on a single cylinder. The results show that the spacing ratio plays an important role in VIV until the ratio reaches 4. For a small spacing ratio, a significant difference between the lift forces on the up- and downstream cylinders appears and induces a large torsional moment. For the convenience of engineering application, a torsional coefficient was proposed. The maximum torsional coefficient can reach 2.9, 1.2 and 0.98 for spacing ratios of 2, 3 and 4 at the reduced velocity of 5, respectively. Considering the vortex induced vibration responses as well as the torsional moment, a spacing ratio of 3 was recommended for tandem floating tunnel design.



## 1. Introduction

The Norwegian Public Road Administration (NPRA) is planning to upgrade the Coastal Highway E39 main road located at the west coast of Norway by replacing the ferry connections with bridges or tunnels. Due to the relatively large crossing distance 5–6 km and water depth of 500 m or more shown in Fig. 1, the traditional subsea tunnel and cable-supported bridge concept may not be suitable. One concept considered, namely a submerged floating tunnel (SFT) bridge, is shown in Fig. 2. The submerged structure is composed of two identical concrete tubes with a diameter of approximately 12.6 m in a tandem configuration and suspended 25–30 of meters below the water surface. However, under the action of the ocean currents, vortices are generated and alternately shed from the sides of the tunnel and, subsequently, induce periodic forces in both transverse (cross-flow) and horizontal (in-line) directions. If the frequency of the vortex-induced force synchronizes with one of the eigenfrequencies of the vibrations of the tunnel, large-amplitude transverse and in-line

* Corresponding author at: State Key Laboratory of Ocean Engineering, Shanghai Jiao Tong University, Shanghai, 200030, China.
*E-mail addresses:* shi.deng@ntnu.no (S. Deng), rhaojie@163.com (H. Ren), xuyuwang@sjtu.edu.cn (Y. Xu), shixiao.fu@sjtu.edu.cn (S. Fu), torgeir.moan@ntnu.no (T. Moan), zhen.gao@ntnu.no (Z. Gao).

https://doi.org/10.1016/j.jfluidstructs.2020.102908
0889-9746/

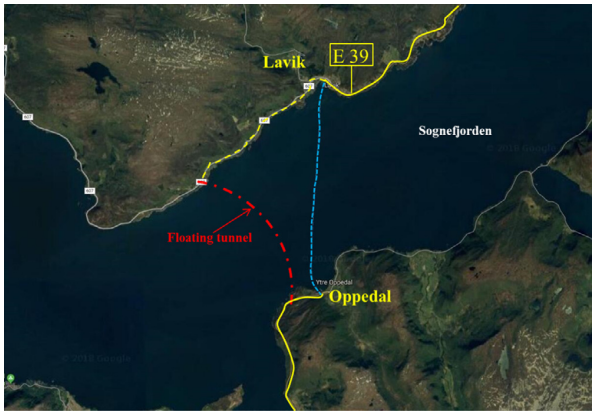


**Fig. 1.** Possible location of floating tunnel in the Sognefjord (Norwegian Public Road Administration (NPRA), 2012).

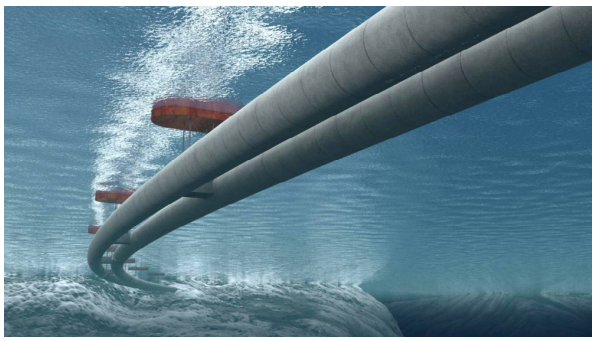

**Fig. 2.** Illustration of a submerged floating tunnel (Norwegian Public Road Administration (NPRA), 2012).

oscillations would be induced. This phenomenon is normally termed as vortex-induced vibration (VIV). VIV leads to severe fatigue damage and decreases the structure lifetime. Therefore, it is important to consider VIV in the design of submerged floating tunnels.

To reveal the mechanics of VIV of slender structures, a typical rigid segment supported by springs with designed mass, geometry, and natural frequency is widely adopted. Most researchers were focused on VIV of marine risers by using a rigid single cylinder. From a series of stationary model towing experiments, researchers have found that the changes in the vortex-induced force, Strouhal number, and wake patterns were a function of Reynolds number (Hallam and Wignall, 1997; Schewe, 1983; Schlichting and Truckenbrodt, 1979; Williamson, 1989). These results offered a basic understanding of the hydrodynamic forces on the single cylinder. Self-oscillation tests were further conducted (Feng, 1968; Govardhan and Williamson, 2000, 2006) to study the amplitude, frequency response, the vortex mode and the lift force. With respect to reduced velocity, three branches, i.e., initial, upper and lower branches, were defined based on the amplitude of the VIV response. The amplitude changes were deeply revealed by observing the vortex mode changes. The vortex mode modification in the transition region between initial and upper branch leads to an abrupt increase of amplitude response and lift coefficient occurring simultaneously (Khalak and Williamson, 1999). In addition, Govardhan and Williamson (2000) presented the influences of system parameters such as mass ratio and damping ratio on the VIV response. These efforts have led to an understanding of the features and mechanisms of VIV on a single cylinder and can serve as a good reference for test matrix design in the tandem twin rigid cylinders experiment.

The floating tunnel is composed of two identical tubes that are rigidly connected through a truss element. Few studies of VIV on this tunnel structure are available. Ljungkrona et al. (1991), Ljungkrona and Sundén (1993), Xu and Zhou (2004) and Zhou and Yiu (2006) presented stationary experiments on tandem twin cylinders, and the influence of spacing ratio on vortex shedding was preliminarily investigated. Based on the flow pattern in the gap between the up- and downstream cylinders, three basic regimes were subdivided, namely, "extended body", "reattachment" and "co-shedding" (Sumner, 2010). Alam et al. (2003a), Arie et al. (1983), and Carmo et al. (2010a,b) further presented the mean drag coefficients, fluctuating drag and lift coefficients, and the Strouhal numbers of the up- and downstream cylinders under different spacing ratios. A critical spacing ratio of 3 for coefficient mutation was observed. To further study the

VIV features under the interaction of the up- and downstream cylinders, King and Johns (1976) investigated the VIV characteristics of a cylinder placed downstream of another cylinder for a spacing ratio ranging from 3.5 to 7 and observed that synchronization of the downstream cylinder vibration coincided with that of the upstream cylinder. Bokaian and Geoola (1984a,b) and Ruscheweyh (1983) observed the vibration of a cylinder in the wake of the upstream cylinder and referred to the vibration as "wake galloping". Kim et al. (2009) presented the results of an investigation on the flow-induced vibration characteristics of two circular cylinders in a tandem arrangement. The interactions of the up- and downstream cylinders on VIV were revealed in three different experimental conditions.

Most of the above investigations on rigid twin cylinders in tandem have been conducted in static or unconnected (two cylinders oscillate individually) conditions. Investigations on the rigidly connected twin cylinders of the tunnel structures are scarce. The VIV features, the lift forces on the up- and downstream cylinders, and the influence of spacing ratio on the vibration and force is still unclear and require further research.

In this study, the floating tunnel element is simplified as a rigidly coupled tandem twin-cylinder model. Free oscillation tests of the two-dimensional twin cylinder model with different spacing ratios in the crossflow (CF) direction is conducted to initially study the VIV features of the SFT. The amplitude responses and lift forces are measured by linear displacement sensors and force transducers, respectively. The reliability of the experimental setup was firstly validated by comparing the experimental results of a stationary twin cylinders model in tandem and an elastically supported single cylinder in steady current with published data in the literature. Compared with the results of the single cylinder, the VIV response, lift forces on the up- and downstream cylinders and torsion derived from the lift force difference under different spacing ratios are further summarized and studied. Selected suggestions are finally proposed for the rigidly coupled floating tunnel designs.

## 2. Experimental description

### 2.1. Model test

A rigidly connected twin-cylinder, as cross-section model of the SFT, is experimentally studied in this paper. The towing experiments were conducted in the Marine Cybernetics Laboratory towing tank at the Norwegian University of Science and Technology with dimensions of 40 $\times$ 6.45 $\times$ 1.5 m. The cylinder model was elastically mounted between the two support frames that were suspended beneath the towing carriage, as shown in Figs. 3 and 4. Two groups of springs were equipped on the support frame to provide the restoring forces for the cylinder model. A pair of low-friction tracks was mounted on one side of each frame. Only VIV in CF direction was considered in the test. A draw-wire displacement sensor and two single-component force sensors were set up at each end of the cylinder. The CF displacement response, lift and drag forces acting on each cylinder were measured simultaneously, and recorded in digital form with the resolution of $10^{-4}$ m and 0.01 N, respectively.

The polished aluminum rigid cylinder with roughness ratio of $6 \times 10^{-6}$ was constructed using hollow tubes and sealed with organic glue to prevent leak of water during the tests. Considering that the gravity of the SFT has been designed close to its buoyance given by the floating tunnel feasibility study (Norwegian Public Road Administration (NPRA), 2012), the mass ratio is set to be 1 in the model test. The dimensions of the cross-section model, the stiffness of the springs and the towing speed are mainly determined based on one of the key concerned non-dimensional parameters, i.e., reduced velocity ($U_r = U/f_nD$, where $U, f_n$ and $D$ refer to the flow velocity, natural frequency in water and diameters, respectively).

The first vertical eigen-frequency of the full scaled SFT is 0.044 Hz, and the incident flow velocity can reach 2.2 m/s (Norwegian Public Road Administration (NPRA), 2012, 2016). Hence, the possible maximum reduced velocity is 4. Moreover, previous researchers have also illustrated that the largest VIV response for a single cylinder system with low mass ratio ($m^*\sim1$, which is defined in Table 1) occurs at a reduced velocity of about 8 (Govardhan and Williamson, 2000). By these reasons, in the present test, the range of the reduced velocity varies from 2.0 to 9.0 to cover the possible reduced velocity of the floating tunnel and the critical reduced velocity of the single cylinder. The key parameters of the test setup are shown in Table 1.

To avoid three-dimensional effects at the two ends stemming from the finite length of the cylinder, two methods were introduced to ensure two-dimensional flow. Firstly, two short dummy cylinders with the same diameter as the model were assembled at both ends. Secondly, two circular endplates were assembled outside the dummy cylinder to reduce the impact of other devices on the flow field. They were fixed on the support frame and do not oscillate with the twin-cylinder during test.

After the apparatus was installed, the structural damping of the system was tested. Fig. 5 shows the time history of the free oscillation test in air, and the damping ratio of the system $\zeta_0$ can be calculated by the following,

$$\zeta_0 = \frac{\delta}{2\pi} = \frac{1}{2\pi} \ln \frac{A_i}{A_{i+1}} \tag{1}$$

where $\delta$ is the logarithmic decrement ratio, $A_i$ and $A_{i+1}$ are the amplitude at the $i$th and $(i+1)$th period, respectively. A set of relevant nondimensional parameters in this problem were selected and presented in Table 2.

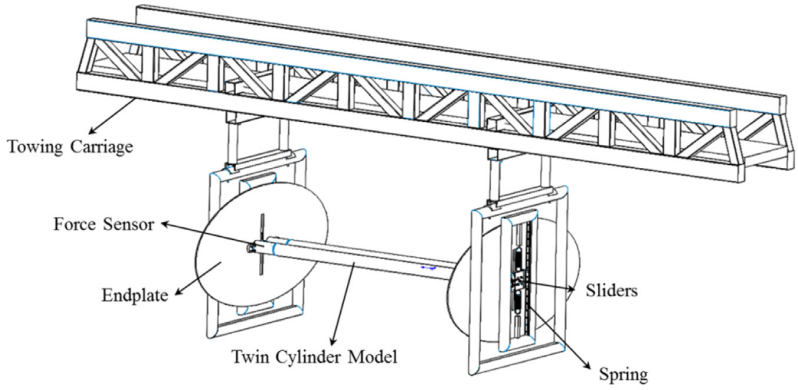


(a) Sketch of the test setup

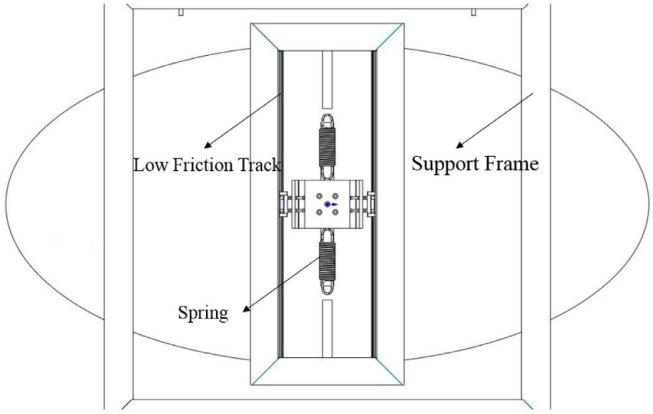


(b) Details of the track and springs arrangement

**Fig. 3.** Design of the experimental apparatus.

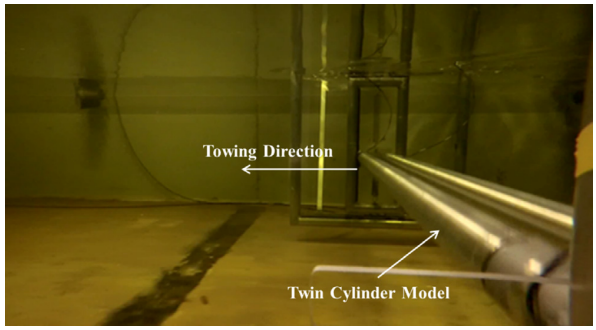


**Fig. 4.** Picture of experimental apparatus underwater.

**Table 1**
Experimental test parameters.

| Parameter | Value | Units |
|---|---|---|
| Single cylinder mass ($m_0$) | 16.1 | kg |
| Twin cylinder mass ($m$) | 32.2 | kg |
| Mass ratio ($m^*$) | 1 | – |
| Structural damping ratio ($\zeta$) | 0.045 | – |
| Roughness ratio ($k/D$) | $6 \times 10^{-6}$ | – |
| Aspect ratio ($L/D$) | 20 | – |
| Stiffness for single cylinder in CF direction provided by the springs | 1270 | N/m |
| Stiffness for twin-cylinder in CF direction provided by the springs | 2540 | N/m |
| Natural frequency in still water ($f_N$) | 1.00 | Hz |

Notes for the test parameters
(i) Mass ratio $m^*$ is defined by $m/(\pi\rho D^2 L/4)$. $D$ and $L$ are the cylinder diameter and length, respectively. The mass $m$ represents the system mass including all components oscillating with the cylinder, i.e. sliders on the track, connection structure between the twin-cylinder and the slides, force sensors and dummies.
(ii) Structural damping ratio $\zeta$ is defined by $\zeta_0/\sqrt{(1+m_A/m)}$ (Govardhan and Williamson, 2006). $\zeta_0$ is the structural damping ratio tested in air. $m_A = C_A\rho D^2 L\pi/4$ is the added mass and $C_A$ is the added mass coefficient, which is only used to normalize the structural damping. The assumption of $C_A = 1$ is widely used in the damping ratio normalization (Govardhan and Williamson, 2000).
(iii) Natural frequency in still water ($f_N$) is obtained by the free decay oscillation test in the still water. The mean value from 5 independent tests is used here.

**Table 2**
Nondimensional parameters.

| Item | Symbols | Expression |
|---|---|---|
| Reduced velocity | $Ur$ | $U/(f_N D)$ |
| Amplitude ratio | $A^*$ | $A/D$ |
| Frequency ratio | $f^*$ | $f/f_N$ |
| Lift coefficient | $C_L$ | $F_L/(1/2\rho DLU^2)$ |
| Mean drag coefficient | $C_D$ | $F_D/(1/2\rho DLU^2)$ |

Notes for the nondimensional parameters in Table 2:
(i) Authors choose here to use the $f_N$ as the natural frequency in water. The frequency $f$, used in $f^*$ is the actual body oscillating frequency during induced vibration.
(ii) Peak values of the oscillation displacement $A$ and the lift force $F_L$ are used to calculate the amplitude ratio and the lift coefficient, respectively. They are obtained by multiplying the root-mean-square ($RMS$) value by $\sqrt{2}$, assuming the displacement and lift force series are with only one dominant frequency and zero mean value, respectively.

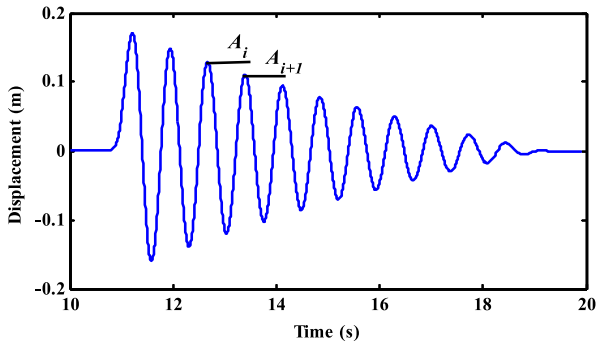


**Fig. 5.** Time history of the free decay oscillation test in air.

## 2.2. Test matrix

In this study, the key test parameter is the spacing ratio which is the center-to-center distance $G$ of the tandem twin cylinders divided by the model diameter $D$, as shown in Fig. 6. It is expressed as:

$$\lambda = \frac{G}{D}. \tag{2}$$

**Table 3**
Test matrix.

| Case | Towing velocity (m/s) | Reduced velocity |
|---|---|---|
| Single cylinder | 0.2:0.05:0.9 | 2:0.5:9 |
| Twin cylinders $\lambda = 2$ | 0.2:0.05:0.9 | 2:0.5:10 |
| Twin cylinders $\lambda = 3$ | 0.2:0.05:0.8 | 2:0.5:8 |
| Twin cylinders $\lambda = 4$ | 0.2:0.05:0.9 | 2:0.5:9 |

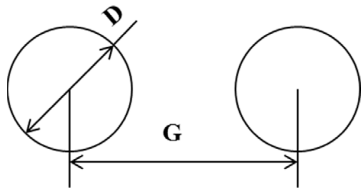


**Fig. 6.** Sketch of the geometry of tandem twin cylinders.

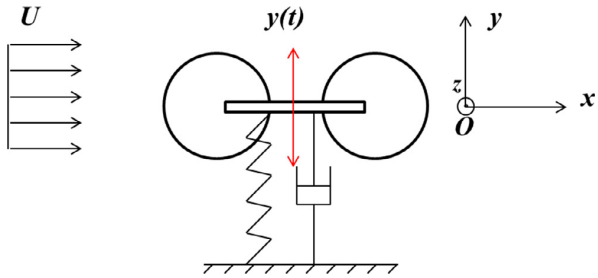


**Fig. 7.** Schematic of self-excited oscillation test and coordinate system definition for rigidly coupled tandem twin cylinders.

During the experiments, the spacing ratio can be adjusted via the connecting apparatus between the cylinders. To reveal the spacing ratio effect on the VIV features, experiment studies on a single cylinder and twin cylinders with spacing ratios ranging from 2 to 4 were conducted. The test matrix is listed in Table 3.

## 3. Preprocessing

The coordinate system and a sketch of the experimental set-up are shown in Fig. 7. Both of the longitudinal axes of the twin cylinders lie in the $z$-axis. The direction of the flow is parallel to the $x$-axis, and the cross-flow direction is along the $y$-axis.

During induced vibration, the forces are measured by the force sensors. However, the measured forces are not all of the lift forces. These forces also include the inertial forces. According to Newton's second law, the relationship among the forces can be expressed by the following,

$$F_m(t) - F_L(t) = m\ddot{y} \tag{3}$$

where $F_m(t)$ is the measured force, $F_L(t)$ is the lift force, and $\ddot{y}(t)$ is the acceleration response.

Fig. 8 presents the time histories of the measured force and the lift force. To verify this identification procedure, the displacement response is recalculated based on the calculated lift force. As presented in Fig. 9, the recalculated displacement response matches well with the measured displacement which proves that the lift force after preprocessing is reliable.

## 4. Results and discussions

### 4.1. Benchmark experiment results

To verify the reliability of the towing carriage and the force transducers, a stationary towing test was conducted firstly on a cylinder and the tandem twin cylinders. The mean drag coefficients and fluctuating lift coefficients of the twin cylinders are shown in Fig. 10. The mean value of the drag coefficient and peak value of the lift force coefficient are presented in the figure, the latter is calculated by multiplying the *RMS* value by $\sqrt{2}$. The lift coefficients of the upstream

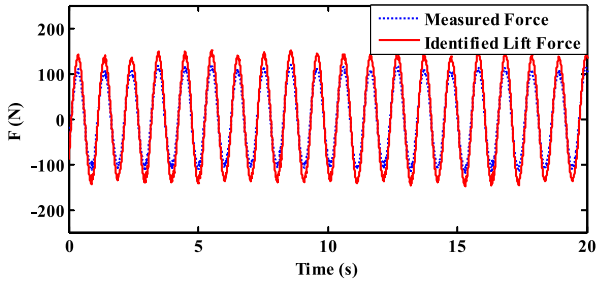


**Fig. 8.** Measured force ($F_m(t)$) and lift force ($F_L(t)$) for the single-cylinder model ($Ur = 5.5$).

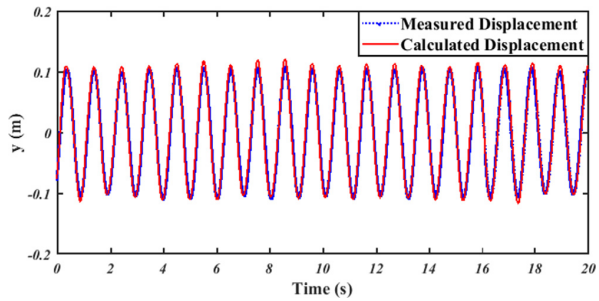


**Fig. 9.** Measured and calculated displacement based on hydrodynamic force for the single-cylinder model ($Ur = 5.5$).

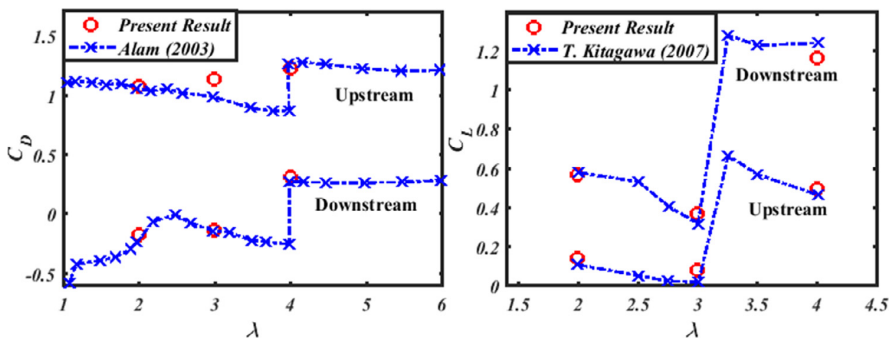


**Fig. 10.** Mean drag force coefficient and fluctuating lift force coefficient for tandem twin cylinders with respect to spacing ratio. The Reynolds number is $6.5 \times 10^4$.

cylinder are smaller than those of the downstream cylinder in the cases studied. The results match well with those reported by Alam et al. (2003b) and Kitagawa and Ohta (2008).

The reliability of the elastic supporting system was then investigated through a self-excited oscillation test of an elastically supported single cylinder. A comparison of the amplitude and frequency with those reported by Govardhan and Williamson (2000) is presented in Fig. 11. The peak value of the response amplitude is calculated in a same way with lift force coefficient. The current result is consistent with the published result at the initial branch. Slightly larger amplitude is observed at the upper branch because the mass ratio adopted in our experiment is smaller. This observation is consistent with Williamson's findings that the smaller mass ratio could lead to a larger amplitude (Govardhan and Williamson, 2000). From the above comparison of drag, lift coefficient and oscillation amplitude and frequency, the test setup is proved to be reliable in both the stationary towing and vibration states.

### *4.2. Amplitude and frequency responses of tandem twin cylinders*

To present the spacing ratio effect on the VIV response, Figs. 12 and 13 display the time histories of the oscillation displacement with different spacing ratios ($\lambda = 2$ and 4) and the corresponding frequency spectra under $Ur = 4.0$ and 6.5,

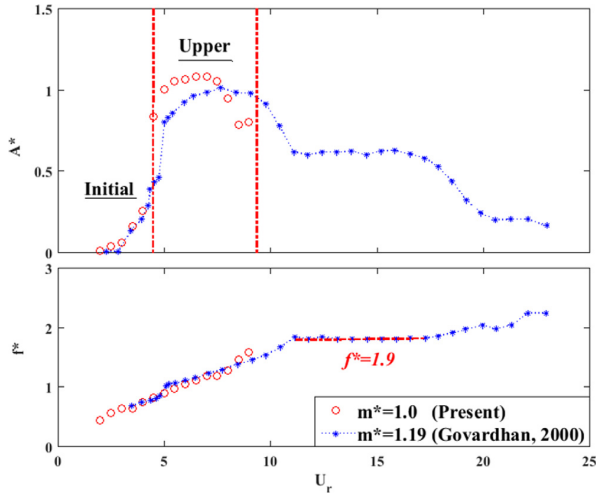


**Fig. 11.** Amplitude and frequency response as a function of reduced velocity for a single cylinder.

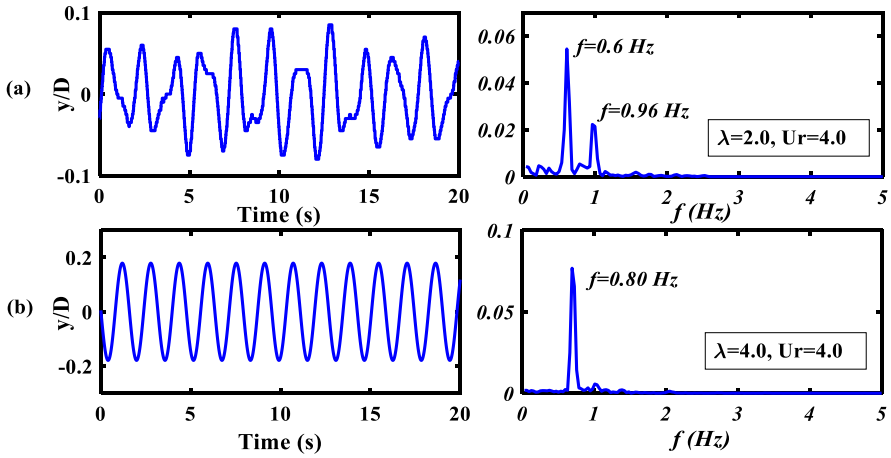


**Fig. 12.** Time history and frequency spectra of the transverse displacements for twin cylinders with $Ur = 4.0$, $\lambda$ is defined in the Eq. (2) and Fig. 6.

respectively. For the small spacing ratio case ($\lambda = 2$), strong amplitude modulation is observed under the low reduced velocity $Ur = 4.0$, whereas this modulation disappears when $\lambda = 4$, and the vibration is stable and regular. It indicates that the critical reduced velocity, which is defined as the minimum reduced velocity that VIV occurs, heavily relies on the spacing ratio.

Via the frequency spectra analysis, two components corresponding to frequencies of 0.6 and 0.96 Hz contribute to the response when $\lambda = 2$. Only one frequency dominates the VIV response when the spacing ratio increases to 4. To further study the difference, the lift force time histories of the up- and downstream cylinders with $\lambda = 2$ are presented in Fig. 14. The lift forces acting on the up- and down-stream cylinders are dominated by the natural frequency (0.96 Hz) and the Strouhal frequency (0.6 Hz), respectively. The bi-component total lift force induces the response modulation in the case with small spacing ratio of 2 under $Ur = 4$.

When the reduced velocity increases to 6.5, a stable time history and one peak frequency spectrum can be observed for all spacing ratios, as shown in Fig. 13. The nondimensional amplitudes for the cases of $\lambda = 2$ and $\lambda = 4$ approach 1.0.

The amplitude and dominant frequency response for all test cases are summarized in Fig. 15 for further analysis. The obvious trend is that the differences in the amplitude and frequency response between the single cylinder and the twin cylinders gradually fade away as the distance ratio increases. Obvious differences are observed in the case of twin cylinders with $\lambda = 2$, whereas the responses of $\lambda = 4$ are almost the same as those of the single cylinder. The critical reduced velocity of the VIV initiation decreases as the distance ratio increases, which means that the twin cylinders with smaller

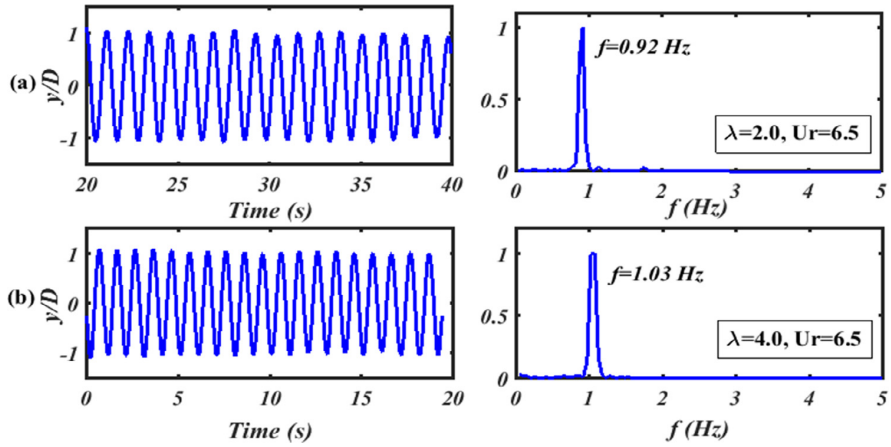


**Fig. 13.** Time histories and frequency spectra of the transverse displacement for twin cylinders with $Ur = 6.5$, $\lambda$ is defined in the Eq. (2) and Fig. 6.

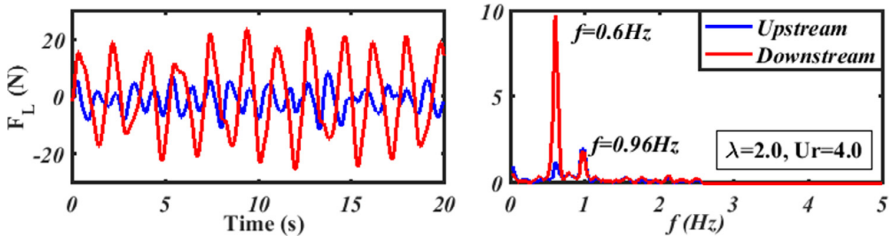


**Fig. 14.** Time history and frequency spectra of lift forces on the twin cylinders, $\lambda$ is defined in the Eq. (2) and Fig. 6.

spacing ratio requires larger flow velocity to excite VIV. In this study, the critical reduced velocities are 4, 3.5 and 2 for the spacing ratios of 2, 3 and 4, respectively. A larger maximum amplitude of the VIV response is observed in the twin cylinders with a smaller distance ratio ($\lambda = 2, 3$), which can reach 1.1.

Compared with the frequency response of the single cylinder, the frequency of the twin cylinders with a smaller spacing ratio is obviously lower than that of the single cylinder. Furthermore, we surprisingly find that a constant frequency ratio exists in the twin cylinders with spacing ratios $\lambda = 2$, $f^* = 0.9$ under the reduced velocity ranging from 4.5 to 6.5. For $\lambda = 3$, $f^* = 0.95$ when the reduced velocity ranges from 5 to 6. The primary reason for the feature of the frequency response might be the vortex interaction between the up- and downstream cylinders. For twin cylinders with a small spacing ratio ($\lambda = 2$ and 3), the weak vortex in the gap area prevents the water from easily escaping from this area (Zhou and Yiu, 2006), and thus, it is speculated that the water in this gap oscillates with the twin cylinders. The circular twin cylinders can be considered as a single ellipse/square cylinder. The VIV frequency response of the square cylinder is obviously lower than that of the circular cylinder (Nemes et al., 2012), which is similar to the current result for twin cylinders with a small spacing ratio. More insightful experiments and CFD simulations will be performed to further reveal this interesting phenomenon.

### 4.3. Lift forces on tandem twin cylinders

The test twin-cylinder model was rigidly connected in this experiment. The interaction between the up- and downstream cylinder cannot be directly reflected by the amplitude response. Furthermore, the time histories of the lift coefficients and the corresponding frequency spectra undergoing VIV for different spacing ratios ($\lambda = 2, 4$) are shown in Fig. 16. Contrary to the stationary towing result, the lift on the upstream cylinder is larger than that on the downstream cylinder. In the stationary test of twin cylinders under a flow velocity $U = 0.65$ m/s, the lift coefficients are 0.1 and 0.5 on the upstream cylinder for $\lambda = 2$ and 4, respectively, and correspondingly, these values of the downstream cylinder are 0. 6 and 1.2. For the self-oscillation test with the same flow velocity, the lift coefficients on the upstream cylinder increase to 4.2 and 4.4 for $\lambda = 2$ and 4, respectively, and the corresponding coefficients of the downstream cylinder are 3.4 and 3.3 as Fig. 17 shown. In addition, the lift frequencies of the up- and downstream cylinders are identical, and the value slightly increases with the spacing ratio. The frequency changes from 0.92 Hz to 1.03 Hz when the spacing ratio increases from 2 to 4.

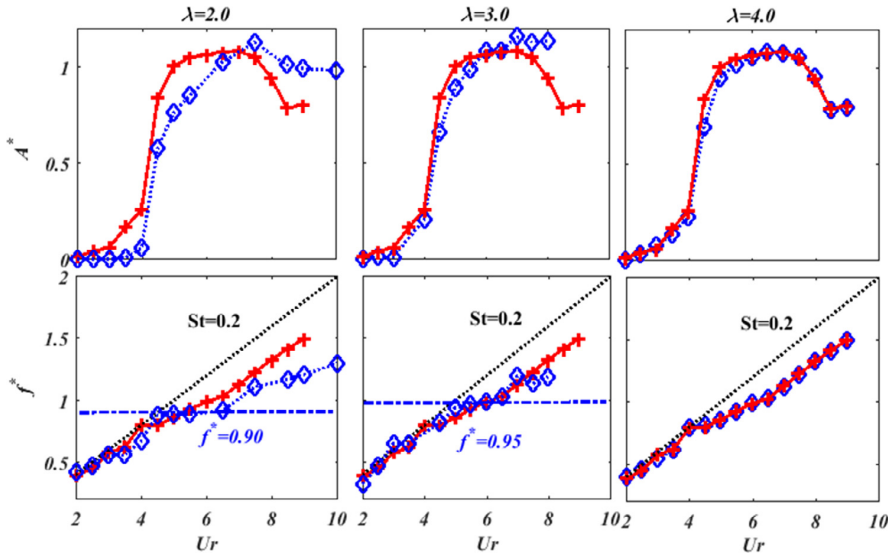


**Fig. 15.** Response amplitude and frequency under different spacing ratios (+ represents the results of a single cylinder; ◇ denotes the results of twin cylinders).

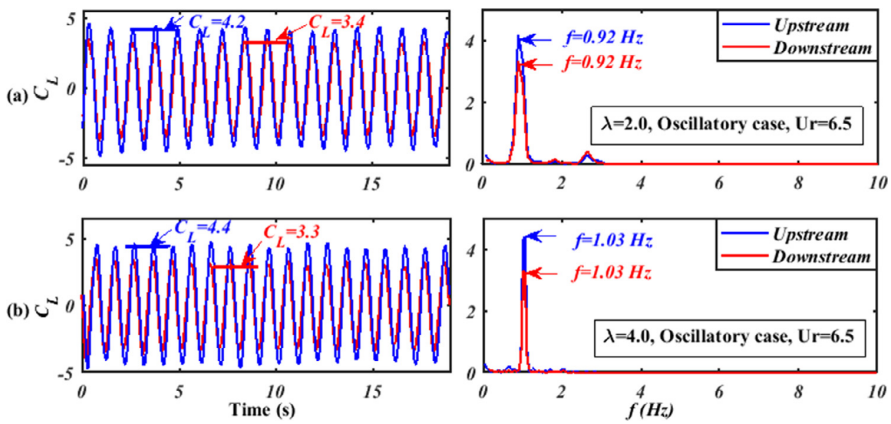


**Fig. 16.** Time histories and frequency spectra of the lift coefficient on the up- and downstream cylinder in the self-oscillation test, λ is defined in the Eq. (2) and Fig. 6.

The effects of the vibration in the cross-flow direction on the vortex shedding are assumed as the main reason for the above phenomenon. In the stationary towing test, the vortex street cannot shed freely from the upstream cylinder when the gap is small, e.g., $\lambda = 2$, which leads to a lift force of almost zero on the upstream cylinder, as illustrated in Fig. 18(a). However, the twin cylinders move perpendicular to the flow when VIV occurs. Thus, the direction of the actual incident flow velocity is no longer parallel to the towing direction, as shown in Fig. 18(b) (d). It is speculated that the vortex of the upstream cylinder can alternatively shed along the actual velocity direction (Govardhan and Williamson, 2000; Ljungkrona et al., 1991), and hence, the lift forces on the upstream cylinder increase. In addition, VIV enhances the intensity of the shear layer alternation behind the downstream cylinder, which leads to a larger lift force than that in the stationary towing test. Due to the shielding effect of the upstream cylinder, the actual incident flow velocity of the downstream cylinder is lower than the towing speed. Thus, the lift force on the downstream cylinder is smaller than that on the upstream cylinder.

To analyze the spacing ratio effect, the lift coefficients of all cases are shown in Fig. 19. It is clearly observed that both lift coefficients of the twin cylinders have the same trend as the single cylinder. The rapid increasing trend of the lift coefficient is observed before the decreasing trend. However, the change rates of the lift coefficients on the up- and downstream cylinders are different. Based on the difference between lift coefficients of upstream and downstream cylinders, the curves

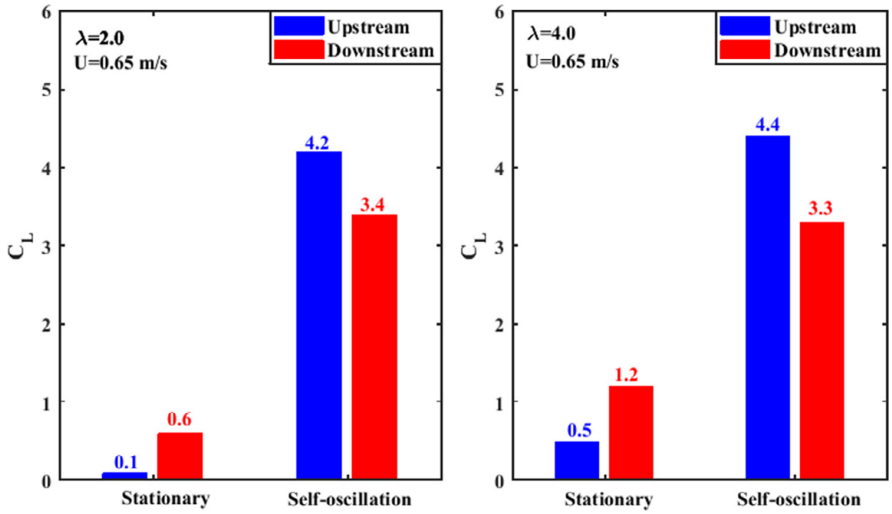


**Fig. 17.** Comparison of lift coefficient between stationary and self-oscillation tandem twin cylinders, λ is defined in the Eq. (2) and Fig. 6.

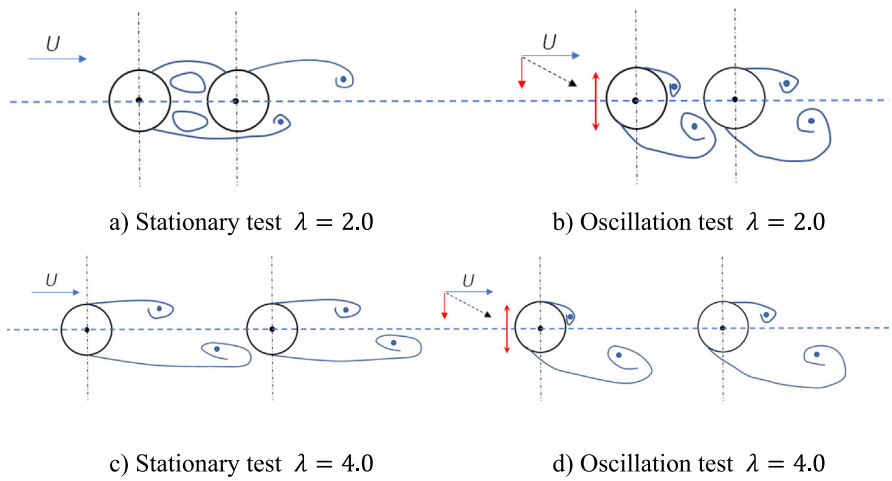


**Fig. 18.** Illustration of the flow past twin cylinders in the stationary and self-excited oscillation test (Govardhan and Williamson, 2000; Ljungkrona et al., 1991).

in Fig. 19 are divided into three regions: (I) initial small difference region, (II) significant difference region and (III) terminal constant difference region. The difference of the lift coefficient remains a small constant value in region I. It is significantly amplified in region II, and then drops to a small constant in region III. Region II is observed in the cases of $\lambda = 2, 3$, while it disappears when $\lambda = 4$. Weak vortex street in the gap area between two cylinders for the cases with small gap ratios is assumed as the main reason for the above phenomenon.

In region (I), the lift coefficient on the upstream cylinder is slightly smaller than that on the downstream cylinder for $\lambda = 2$ because the system remains nearly static. This is consistent with the stationary test. As the spacing ratio increases, the lift coefficient of the upstream cylinder gradually increases and is larger than that of the downstream cylinder when $\lambda = 4$. They reach the maximum values of 5.2 and 4.6 at the end of this region of $U_r = 5.5$, for up- and downstream cylinders in the case of $\lambda = 4$, respectively. The main reason can be attributed to the VIV effect on vortex shedding, as discussed in Section 4.2.

In region (II), the lift force on the upstream cylinder is much larger than that on the downstream cylinder. The lift coefficients of both cylinders reach the peak values in this region. The $C_L$ of the upstream cylinder reaches the maximum values at $Ur = 5$ for $\lambda = 2$ and 3. Correspondingly, the maximum values of $C_L$ in the downstream cylinder occur at

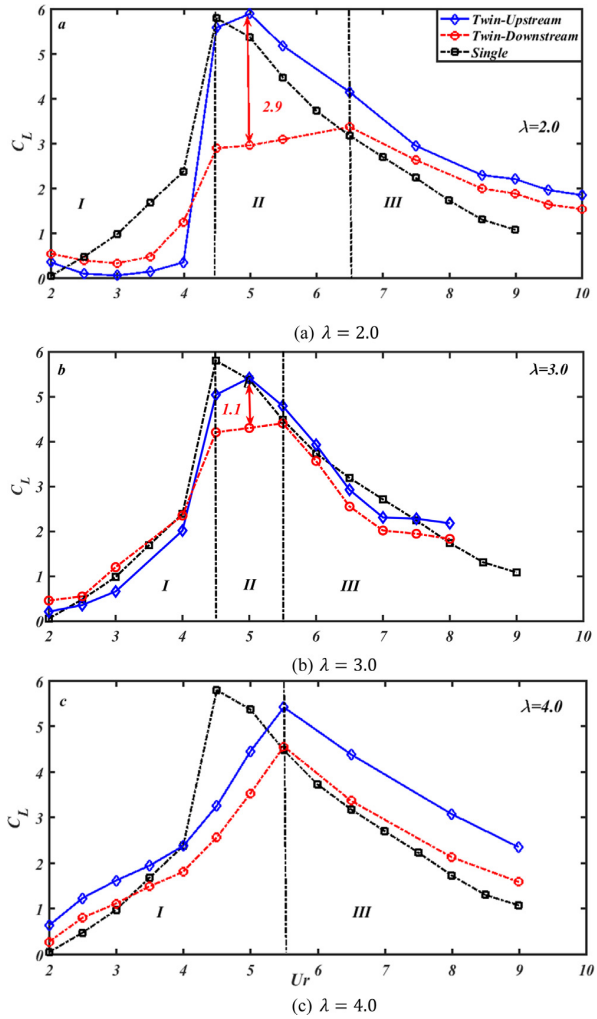


**Fig. 19.** Lift coefficients in self-excited oscillation test. (*I, II and III* are the initial small difference region, significant difference region and terminal constant difference region).

$U_r = 6.5$ and 5.5. The downtrend of the coefficients is found on the upstream cylinder, whereas the downstream cylinder coefficients increase significantly as the spacing ratio increases. The different trends on the two cylinders lead to a decrease in the lift difference with the spacing ratio.

In region (III), the lift forces on upstream and downstream cylinder have similar values. Compared with $\lambda = 2$ and 3, a more significant lift difference is observed for $\lambda = 4$. This might be because the vortex shedding from the downstream cylinder captures that from the upstream cylinder. The two vortices cancel each other, which leads to a smaller lift force on the downstream cylinder for the case of $\lambda = 4$. These results are consistent with the findings published by Zhao (2013).

Overall, there is a difference between the lift forces on the up- and downstream cylinders when the model undergoes VIV. Such a lift difference induces a torsional moment, which might be a new challenge in floating tunnel design. Thus, the feature of this torsional moment under the VIV condition is discussed in the following section.

### *4.4. Torsional moment on tandem twin cylinders*

The torsional moments derived from the lift force difference are defined as follows,

$$T = |F_{L\_D} - F_{L\_U}|\, G/2 \tag{4}$$

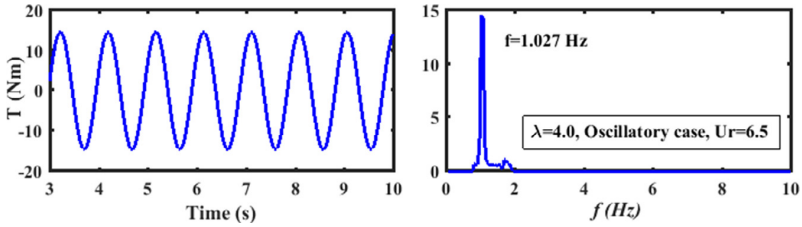


**Fig. 20.** Time histories and frequency spectra of torsional moment.

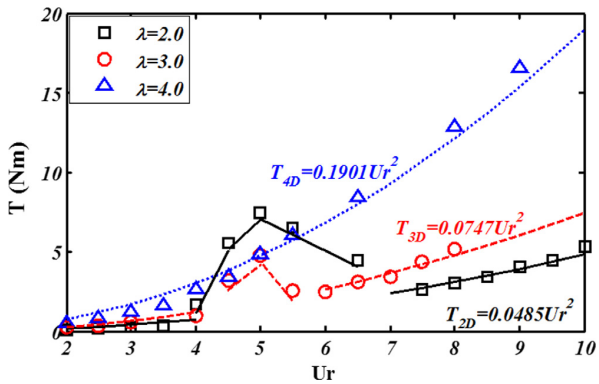


**Fig. 21.** Torsional moment as a function of reduced velocity with respect to spacing ratio.

where $F_{L\_U}$ and $F_{L\_D}$ denote the lift forces on the up- and downstream cylinders, respectively. Fig. 20 presents a typical time history of the torsional moment and the corresponding frequency spectrum for $\lambda = 4$ under $Ur = 6.5$. The torsional moment harmonically vibrates with one dominant frequency.

To study the torsional moment with respect to reduced velocity in different spacing ratio cases, the amplitudes of torsional moments calculated by Eq. (4) are summarized in Fig. 21. The results show that the torsional moment is quadratic to the reduced velocity (flow velocity) for the cases with spacing ratio of 4. Similar relationships for $\lambda = 2$ and 3 can also be found in region (I) and (III). However, the torsional moment for a smaller spacing ratio is no longer quadratic with the reduced velocity and is obviously amplified in region (II), especially for $\lambda = 2$. This significant magnification of the torsional moment for twin cylinders with a smaller spacing ratio should be considered in floating tunnel design.

Based on the discussion in Section 4.3, the lift forces on two cylinders can be viewed as a harmonic vibration. Therefore, we assume that the lift forces on the up- and downstream cylinders can be expressed as follows,

$$\begin{aligned} F_{L\_U} &= \frac{1}{2}\rho C_{L\_U} D U^2 L \sin(\omega t + \phi_1) \\ F_{L\_D} &= \frac{1}{2}\rho C_{L\_D} D U^2 L \sin(\omega t + \phi_2) \end{aligned} \tag{5}$$

where $C_{L\_U}$ and $C_{L\_D}$ are the lift coefficients of the up- and downstream cylinders, and $\phi_1$ and $\phi_2$ denote the phase angles, respectively. Substituting Eq. (5) into Eq. (4), the torsional moment can be further expressed as:

$$T = \frac{1}{2}\rho D U^2 L \cdot \frac{G}{2} \cdot \left| C_{L\_D} \sin(\omega t + \phi_1) - C_{L\_U} \sin(\omega t + \phi_2) \right| \tag{6}$$

From Eq. (6), it is clear that the differences in the lift force amplitude and phase angles between the two cylinders are the two main sources for the torsional moment of the rigidly coupled tandem twin cylinders. As Fig. 19 shows, the lift force amplitude difference increases sharply in region (II), which is the key reason for the abrupt jump of the torsional moment. To study the contribution of phase difference to the torsional moment, the lift phase difference $\theta = |\phi_1 - \phi_2|$ can be expressed as:

$$\theta = \frac{|t_1 - t_0|}{T} \times 360\,(^\circ) \tag{7}$$

where $t_1$ and $t_0$ are the zero-up-crossing time of the lift forces on the up- and downstream cylinders, respectively, as shown in Fig. 22. $T$ is the period of the lift force.

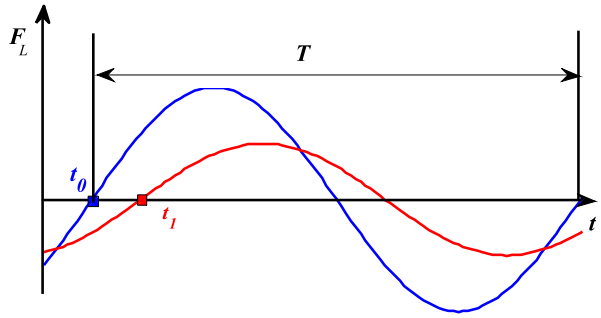


**Fig. 22.** Phase difference between two lift forces.

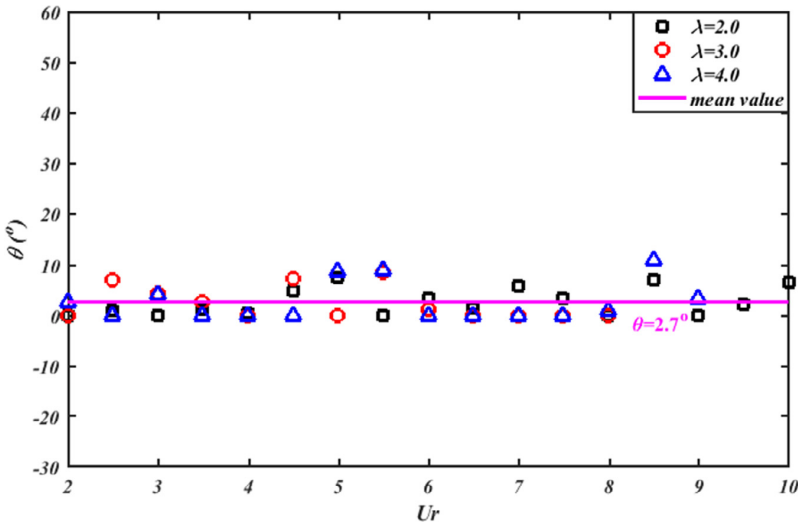


**Fig. 23.** Variation of the phase difference with respect to reduced velocity for different spacing ratios.

Using Eq. (7), the phase differences for all cases are calculated and presented in Fig. 23. The lift forces of the two cylinders are nearly in phase under the VIV condition for all cases, with a phase difference around 2.7° in most cases. The maximum phase difference reaches 10° at the $Ur = 8.5$, but there is not sharply changing of the torsion. Therefore, the abrupt increase of the torsional moment in Fig. 21 mainly depends on the increase of the lift force amplitude difference and has a minor relationship with phase difference.

For the convenience of rigidly coupled floating tunnel design, by combining with Eq. (6), the torsional coefficients are further defined as follows,

$$C_T = \frac{T}{\frac{1}{4}\rho D U^2 L G} \tag{8}$$

Fig. 24 illustrates the torsional coefficients under VIV condition versus reduced velocity for all concerned spacing ratios. In the stationary model test, the torsional coefficients keep almost constant, which are 0.64, 0.42 and 0.77 corresponding to the spacing ratios 2, 3 and 4 (Deng et al., 2020). However, the torsional coefficient under VIV condition increases sharply in region (II), especially for smaller spacing ratios, which reach 2.9 and 1.24 for $\lambda = 2$ and 3. It indicates that the VIV can amplify the torsional coefficients significantly. In region (I) and (III) for all spacing ratios, a stable variation of the coefficient can be found, and a larger coefficient occurs as $\lambda = 4$.

Based on the torsional moment under different spacing ratios in our study, the spacing ratio of 2 is not a good choice since there is a sharp increase for the torsional coefficient near $Ur = 4$. In the range $2 < Ur < 4$, the torsional coefficient as $\lambda = 3$ is much smaller than that as $\lambda = 4$. In addition, from the view of lift and mean drag coefficients in stationary result, as shown in Fig. 10. In the range of $2 < \lambda < 4$, the lift coefficient decreases at the beginning and then increases, the minimum coefficient is achieved at $\lambda = 3$. Therefore, $\lambda = 3$ is preliminarily recommended for the tunnel design based on the presented experimental results.

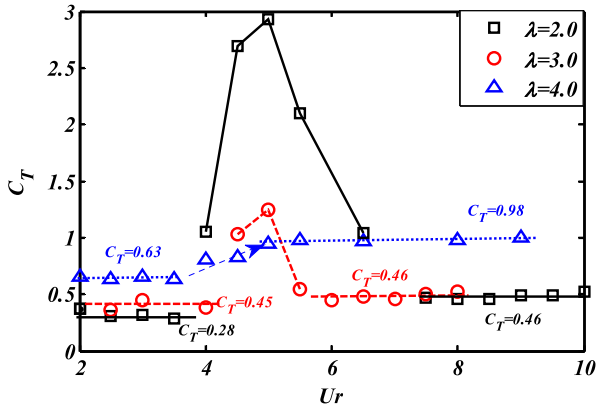


**Fig. 24.** Torsional coefficient of rigidly coupled tandem cylinders with respect to spacing ratio and reduced velocity under self-oscillation condition.

## 5. Conclusions

In this paper, VIV of a submerged floating tunnel has been preliminarily investigated through a self-oscillation test of elastically supported tandem twin rigid cylinders with small mass ratio in CF direction in steady flow. VIV responses in in-line and torsional direction are not in the scope of the study. The influence of spacing ratio on VIV response, lift coefficient and torsional coefficient were mainly studied. The main conclusions are drawn as follows:

(1) Differences in VIV between the single- and twin-cylinder models are observed until the spacing ratio reaches 4. The critical reduced velocity of VIV initiation decreases with the spacing ratio. A lower dominant frequency and slightly larger response amplitude of VIV are found for smaller spacing ratios ($\lambda = 2, 3$), and the maximum response amplitude can reach 1.1 D.

(2) Both VIV response and spacing ratio significantly affect the lift coefficients on the twin cylinders. The lift force acting on the oscillating upstream cylinder model is almost 40 times of that on the stationary model as the spacing ratio is small. Besides, the lift force on the upstream cylinder is obviously larger than that on the downstream cylinder when the twin cylinders undergo significant VIV, which is exactly different from that for the twin cylinders under the stationary state. The lift coefficient difference decreases with spacing ratio.

(3) The torsion moments derived from the lift force difference are first observed and analyzed in our experiments. The quadratic relationship between the torsion moment and the reduced velocity appears in the region I and III. In the region II, a sharp increase in the torsion moment and coefficients occurs. The maximum torsion coefficients can reach 2.9, 1.2 and 0.98 for spacing ratios of 2, 3 and 4, respectively, whereas it is only about 0.64, 0.42 and 0.77 in the stationary test.

## Declaration of competing interest

The authors declare that they have no known competing financial interests or personal relationships that could have appeared to influence the work reported in this paper.

## CRediT authorship contribution statement

**Shi Deng:** Writing - original draft. **Haojie Ren:** Writing - original draft. **Yuwang Xu:** Validation. **Shixiao Fu:** Supervision. **Torgeir Moan:** Supervision. **Zhen Gao:** Supervision.

## Acknowledgments

The authors gratefully acknowledge the financial supports from Norwegian Public Roads Administration and the Research Council of Norway. Thanks are extended to the support from the Centre for Ships and Ocean Structures (CeSOS) and Centre for Autonomous Marine Operations and Systems (AMOS), at the Department of Marine Technology, NTNU, Trondheim, Norway. The supports from the national Science Fund for Distinguished Young Scholars of China (No. 51825903), Shanghai Science and Technology Program (No. 19XD1402000), The 13th Five-Year National Science and Technology Major Project of China (2016ZX05028-001) and Ub-project of the Important National Science & Technology Specific Projects of China (No. 2016ZX05028-002-004).

## References


Alam, M.M., Moriya, M., Takai, K., Sakamoto, H., 2003a. Fluctuating fluid forces acting on two circular cylinders in a tandem arrangement at a subcritical Reynolds number. J. Wind Eng. Ind. Aerodyn. 91, 139–154.

Alam, M.M., Moriya, M., Takai, K., Sakamoto, H., 2003b. Fluctuating fluid forces acting on two circular cylinders in a tandem arrangement at a subcritical Reynolds number. J. Wind Eng. Ind. Aerodyn. 91, 139–154.

Arie, M., Kiya, M., Moriya, M., Mori, H., 1983. Pressure fluctuations on the surface of two circular cylinders in tandem arrangement. J. Fluids Eng. 105, 161–166.

Bokaian, A., Geoola, F., 1984a. Proximity-induced galloping of two interfering circular cylinders. J. Fluid Mech. 146, 417–449.

Bokaian, A., Geoola, F., 1984b. Wake-induced galloping of two interfering circular cylinders. J. Fluid Mech. 146, 383–415.

Carmo, B.S., Meneghini, J.R., Sherwin, S.J., 2010a. Possible states in the flow around two circular cylinders in tandem with separations in the vicinity of the drag inversion spacing. Phys. Fluids 22, 054101.

Carmo, B.S., Meneghini, J.R., Sherwin, S.J., 2010b. Secondary instabilities in the flow around two circular cylinders in tandem. J. Fluid Mech. 644, 395–431.

Deng, S., Ren, H., Fu, S., Moan, T., Gao, Z., 2020. Numerical study on the dynamic response of a submerged floating tunnel under current loads based on the segment model towing test results. ISOPE. Submitted for possible publication.

Feng, C., 1968. The Measurement of Vortex Induced Effects in Flow Past Stationary and Oscillating Circular and D-Section Cylinders (Doctoral thesis). University of British Columbia.

Govardhan, R., Williamson, C., 2000. Modes of vortex formation and frequency response of a freely vibrating cylinder. J. Fluid Mech. 420, 85–130.

Govardhan, R., Williamson, C., 2006. Defining the 'modified Griffin plot'in vortex-induced vibration: revealing the effect of Reynolds number using controlled damping. J. Fluid Mech. 561, 147–180.

Hallam, A., Wignall, P.B., 1997. Mass Extinctions and their Aftermath. Oxford University Press, UK.

Khalak, A., Williamson, C., 1999. Motions, forces and mode transitions in vortex-induced vibrations at low mass-damping. J. Fluids Struct. 13, 813–851.

Kim, S., Alam, M.M., Sakamoto, H., Zhou, Y., 2009. Flow-induced vibrations of two circular cylinders in tandem arrangement. Part 1: Characteristics of vibration. J. Wind Eng. Ind. Aerodyn. 97, 304–311.

King, R., Johns, D., 1976. Wake interaction experiments with two flexible circular cylinders in flowing water. J. Sound Vib. 45, 259–283.

Kitagawa, T., Ohta, H., 2008. Numerical investigation on flow around circular cylinders in tandem arrangement at a subcritical Reynolds number. J. Fluids Struct. 24, 680–699.

Ljungkrona, L., Norberg, C., Sunden, B., 1991. Free-stream turbulence and tube spacing effects on surface pressure fluctuations for two tubes in an in-line arrangement. J. Fluids Struct. 5, 701–727.

Ljungkrona, L., Sundén, B., 1993. Flow visualization and surface pressure measurement on two tubes in an inline arrangement. Exp. Therm Fluid Sci. 6, 15–27.

Nemes, A., Kalapos, A., Domsik, P., Forster, T., 2012. Three-dimensional speckle-tracking echocardiography–a further step in the non-invasive three-dimensional cardiac imaging. Orvosi Hetil. 153, 1570–1577.

Norwegian Public Road Administration (NPRA), 2012. Feasibility study for crossing the Sognefjord - Submerged floating tunnel. https://www.vegvesen.no/en/Home, download on 1st Feb. 2019.

Norwegian Public Road Administration (NPRA), 2016. Report for BJØRNAFJORDEN submerged floating tube bridge. https://www.vegvesen.no/en/Home, download on 1st Feb. 2019.

Ruscheweyh, H., 1983. Aeroelastic interference effects between slender structures. J. Wind Eng. Ind. Aerodyn. 14, 129–140.

Schewe, G., 1983. On the force fluctuations acting on a circular cylinder in crossflow from subcritical up to transcritical Reynolds numbers. J. Fluid Mech. 133, 265–285.

Schlichting, H.T., Truckenbrodt, E.A., 1979. Aerodynamics of the Airplane. McGraw-Hill Companies.

Sumner, D., 2010. Two circular cylinders in cross-flow: a review. J. Fluids Struct. 26, 849–899.

Williamson, C., 1989. Oblique and parallel modes of vortex shedding in the wake of a circular cylinder at low Reynolds numbers. J. Fluid Mech. 206, 579–627.

Xu, G., Zhou, Y., 2004. Strouhal numbers in the wake of two inline cylinders. Exp. Fluids 37, 248–256.

Zhao, M., 2013. Flow induced vibration of two rigidly coupled circular cylinders in tandem and side-by-side arrangements at a low Reynolds number of 150. Phys. Fluids 25, 123601.

Zhou, Y., Yiu, M., 2006. Flow structure, momentum and heat transport in a two-tandem-cylinder wake. J. Fluid Mech. 548, 17–48.

## D.2 Paper 2

**Paper 2:**
Deng S, Ren H, Xu Y, Fu S, Moan T, Gao Z. Experimental Study on the Drag Forces on a Twin-tube Submerged Floating Tunnel Segment Model in Current. *Applied Ocean Research* 2020 **104**:102326

Applied Ocean Research 104 (2020) 102326

Contents lists available at ScienceDirect

Applied Ocean Research

journal homepage: www.elsevier.com/locate/apor

# Experimental study on the drag forces on a twin-tube submerged floating tunnel segment model in current

Shi Deng[a], Haojie Ren[b], Yuwang Xu[b,*], Shixiao Fu[a,b,c], Torgeir Moan[a,c,d], Zhen Gao[a,c,d]

[a] Department of Marine Technology, NTNU, NO-7491 Trondheim, Norway
[b] State Key Laboratory of Ocean Engineering, Shanghai Jiao Tong University, Shanghai, 200030 China
[c] Centre for Ships and Ocean Structures, NTNU, Marine Technology Centre, NO-7491, Trondheim, Norway
[d] Center for Autonomous Operations and System, NTNU, Marine Technology Centre, NO-7491, Trondheim, Norway

ARTICLE INFO

*Keywords:*
Submerged floating tunnel
Drag force
Spacing distance
Vortex induced vibration
Submergence

ABSTRACT

In this paper, the drag forces on a rigid segment of a twin-tube submerged floating tunnel (SFT) under various Re number and submergence are experimentally investigated with a simplified rigidly connected tandem twin-cylinder model towed in a tank. The effects of the spacing distance between two cylinders and vortex-induced vibration (VIV) on the drag forces are investigated through stationary and self-oscillation towing tests. It is found that, in the stationary cases, the drag forces on the cylinders act in opposing directions when the spacing ratio is 2 and 3, which leads them attracting each other. Under VIV conditions, the drag forces are significantly amplified. The maximum mean drag coefficients of the up- and downstream cylinders increase from 1.27 to 4.1 and 0.43 to 1.7, respectively. As for the submergence effect, it is found that both the VIV response amplitude and mean drag coefficient decrease with the decreasing of the submerged depth, especially when the depth ratio is below 3.7.

## 1. Introduction

The Norwegian Public Road Administration (NPRA) is planning to upgrade Coastal Highway E39, which is located on the west coast of Norway, by replacing the ferry connections with a submerged floating tunnel (SFT). The SFT consists of two rigidly connected identical concrete tunnel tubes with a diameter of 12.6 m in a tandem configuration. It is suspended 24.6-32.6 m below the water surface, which is defined as the distance from the lower side of the tunnel tube to the initial free surface, as shown in Fig. 1 (Fjeld et al., 2012). In this submerged depth, current load is a key factor challenging the reliability and fatigue lifetime. The hydrodynamic force acting on the tunnel in a current field consists of the lift force in the crossflow (CF) direction and the drag force in the inline (IL) direction. The former one will excite small amplitude but high frequency oscillation in the CF direction, namely vortex-induced vibration (VIV) which has been found to significantly amplify the drag forces (Vandiver, 1983). The mean drag force causes steady deformation of the tunnel tube with a relatively large amplitude which subsequently affects the structural strength (Kitagawa and Ohta, 2008, Meneghini et al., 2001, Schewe, 1983, Sumer, 2006). The Morison equation is typically used to calculate the mean drag force on the tunnel tube during its strength and safety design. Mean drag force coefficients of the two tunnel tubes are different from those of the conventional single cylinder system, and heavily depend on the spacing distance since it is a key parameter to decide the flow pattern between and behind the tandem twin cylinders (Sumner, 2010). Free surface could also affect the mean drag coefficients of the SFT because of its small submerged depth (Chu et al., 2018). Thus, investigations of the effects from VIV, spacing ratios (defined by the ratio between center-to-center distance dividing the cylinder diameter) and submergences on the mean drag forces of SFT are necessary (Chu et al., 2018, Chung, 2016, Fu et al., 2013, Ren et al., 2019, Sareen et al., 2018).

Many researchers have performed physical model tests with a single cylinder. As for the drag amplification due to VIV (Gopalkrishnan, 1993, Jhingran, 2008), the results from previous studies show that the mean drag coefficient synchronizes with the VIV response amplitude (Gopalkrishnan, 1993, Jhingran, 2008, Kaiktsis et al., 2007, Song et al., 2016), and the maximum values coincidently appear at the same time (Khalak and Williamson, 1997). In addition, Khalak and Williamson presented the influences of system parameters, such as the mass and damping ratio, on the VIV-amplified drag forces (Khalak and Williamson, 1997, Khalak and Williamson, 1999). In the study of the effects of submergence, most of the researchers are focused on a fixed cylinder (Bozkaya et al., 2011,

* Corresponding author.
*E-mail address:* xuyuwang@sjtu.edu.cn (Y. Xu).

https://doi.org/10.1016/j.apor.2020.102326
Received 23 January 2020; Received in revised form 28 July 2020; Accepted 5 August 2020

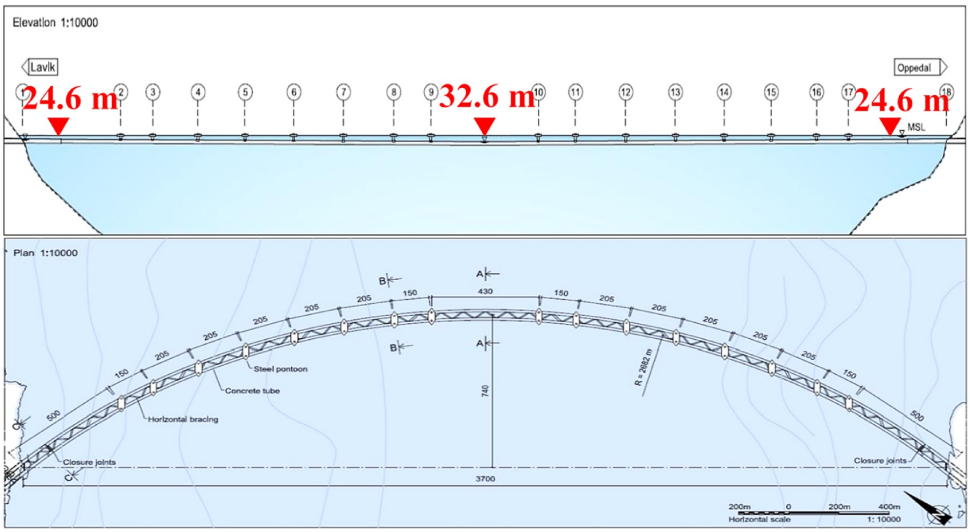


**Fig. 1.** SFT configuration (Fjeld et al., 2012).

Reichl et al., 2005, Sheridan et al., 1997). The modal tests and numerical simulations have shown that the free surface can limit the vortex formation as the cylinder approaches it. Meanwhile, the VIV response amplitude and mean drag force decreases monotonically as the immersion depth decreases (Chung, 2016, Sareen et al., 2018). The effect of the submergence on VIV is normally discussed with respect to the Froude number ($F_r = \frac{U}{\sqrt{gh}}$), which is defined by the flow velocity $U$, gravitational acceleration $g$ and submerged water depth $h$ (Gopalkrishnan, 1993). The previous studies have led to a comprehensive understanding of the features and mechanisms of VIV-generated drag amplification and the effect of the submergence for a single-cylinder.

However, the floating tunnel considered by NPRA is composed of two identical tubes that are rigidly connected in tandem through truss structures (Fjeld et al., 2012). For the tandem twin cylinders structure, some researchers have studied the effect of the center-to-center distance on the drag forces on the up- and downstream cylinders separately at low Reynolds number (Re) under static condition through towing tests or numerical simulations (Kitagawa and Ohta, 2008, Alam et al., 2003, Carmo et al., 2010, Carmo et al., 2010). It was observed that the drag coefficients of the two stationary cylinders gradually increased with the increases of the spacing ratio. A critical spacing ratio ($\lambda = 4.0$) has been found, which corresponds to the point where an abrupt increase appears in the drag coefficient (Alam et al., 2003), and the drag coefficient of the upstream cylinder approaches to that of the single cylinder (Alam et al., 2003, Alam et al., 2005, Alam and Zhou, 2007). Compared with an isolated cylinder, a large amplitude of oscillation and a wider lock-in region are found for cylinders in tandem arrangement (Borazjani and Sotiropoulos, 2009). The 'response amplitude-reduced velocity curve' for the upstream cylinder is similar to that of an isolated cylinder, but it displays a shift on the reduced velocity axis depending on the spacing ratio (Chen et al., 2018, Papaioannou et al., 2008). Meanwhile, for the downstream cylinder, it is found that the VIV amplitude, frequency and amplified drag forces are highly affected by its own reduced velocity as well as that of the upstream cylinder (Huang and Herfjord, 2013, Huang and Sworn, 2011).

However, those previous studies on drag forces of twin cylinders in tandem arrangement were based on either stationary model tests with large submergence, or unconnected (two cylinders oscillate individually) cylinders which are not suitable for the design of SFT which comprises two rigidly connected tubes. The VIV-generated drag amplification and the free surface effect on oscillating rigidly connected twin cylinders are still unclear and require further research.

In this study, a series of stationary model towing tests and self-oscillation experiments were conducted to investigate the effect of the spacing distance, VIV and submergence on the drag forces acting on rigidly connected tandem twin cylinders. The reliability of the experimental setup was first validated by comparing the experimental results of a stationary single cylinder in steady flow with the published data in the literature. Then, the effect of the spacing distance, VIV and submergence on the drag forces on the tandem twin-cylinder model was investigated.

## 2. Experimental setup

### 2.1. Test setup

In the study of VIV of flexible cylinders, such as the submerged floating tunnel and marine risers, there are normally two approaches. The first one is using a rigid segment model. It can provide a basic understanding of the VIV features, especially the hydrodynamic forces (Khalak and Williamson, 1999, Govardhan and Williamson, 2000). The second one is to use a long and flexible cylinder model, mainly focusing on its deformations (Song et al., 2016, Song et al., 2016). In the second approach, the scaling from the prototype to the experimental model is more challenging because many parameters, such as the mass, length, diameter, stiffness and so on, should be considered. In the first approach, as applied in the paper, we mainly guarantee two parameters, i.e., mass ratio and reduced velocity, to be similar between the experimental model and the prototype, which are the key parameters that determine the oscillation amplitude and hydrodynamic forces.

The experiments were conducted in the Marine Cybernetics Laboratory towing tank at the Norwegian University of Science and Technology. The dimensions of the tank are 40 m × 6.45 m × 1.5 m. The maximum speed of the towing carriage is 1.2 m/s. The test setup consists of a towing carriage, two support frames and a rigidly connected tandem twin-cylinder model. The two smooth rigid cylinders are made of aluminum with a relative surface roughness $k/D = 0.6 \times 10^{-5}$ ($k$ is the average height of the surface irregularities and $D$ is the cylinder diameter). The diameter and length of the cylinder are 0.1 m and 2.05

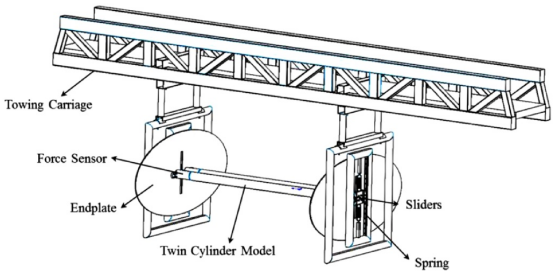


**Fig. 2.** Sketch of the experimental setup

**Fig. 3.** Photograph of the experimental setup

m, respectively. The cylinder models were elastically mounted between two support frames that were suspended beneath a towing carriage, as shown in Figs. 2 and 3. Two groups of springs were equipped on the support frame to provide the restoring forces for the models. In the self-oscillation test, the model was only allowed to oscillate vertically, i.e. in the CF direction. A pair of low-friction tracks was mounted on one side of each frame to guide the CF motion. One displacement sensor and two force sensors were set up at both ends of the cylinder. The drag forces acting on each cylinder and the CF displacement response were measured simultaneously and recorded in digital form.

Two methods were adopted to avoid 3D effects stemming from the finite length of the cylinder. First, two dummy cylinders with the same diameter as the model were assembled at both ends of the model. A small space (< 1 mm) was left between the dummy cylinder and the model to guarantee that the force transducer measured only the force acting on the model. Second, two circular endplates were assembled outside the dummy cylinder to reduce the impact of the other devices on the flow field.

### 2.2. Test arrangement

Fig. 4 shows the definition of the spacing ratio used in the spacing distance effect discussion, which is equal to the center-to-center distance divided by the cylinder diameter, used in the spacing distance effect discussion. The towing speed in this test varies from 0.2 m/s to 1.0 m/s, which corresponds to the reduced velocity range of 2.0-10.0 in the VIV self-oscillation test. To discuss the submergence effect, a non-dimensional depth ($h^*$) is defined in Fig. 4, $h^*=h/D$, where $h$ is the distance from the bottom of the cylinder to the initial free surface and $D$ is the cylinder diameter. Details of the test cases are shown in Table 1. The submerged depth of the first three cases is set to $h^*=6.8$.

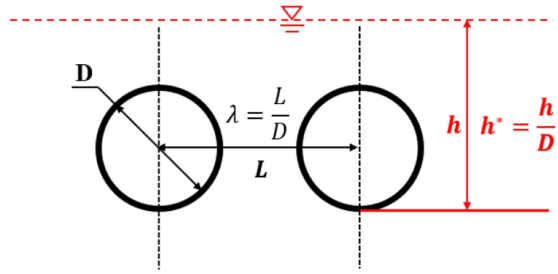


**Fig. 4.** Sketch of the spacing ratio and submergence

**Table 1**
Details of the test cases.

| Case | Spacing ratio | Towing speed (m/s) | Submerged water depth $h^*$ |
|---|---|---|---|
| Validation test (single-cylinder) | - | 0.2-1.0 | 6.8 |
| Stationary model test | 2, 3, 4 | 0.2-1.0 | 6.8 |
| Self-oscillation test | 2, 3, 4 | 0.2-1.0 | 6.8 |
| Submerged depth test | 4 | 0.2-1.0 | 0.1-6.8 |

## 3. Basic theory

The drag forces on the up- ($F_{D\_U}$) and downstream ($F_{D\_D}$) cylinders can be expressed by Eqs. (1) and (2), respectively (Sumer, 2006):

$$F_{D\_U} = \frac{1}{2}\rho C_{D\_U} DlU^2 \tag{1}$$

$$F_{D\_D} = \frac{1}{2}\rho C_{D\_D} DlU^2 \tag{2}$$

where $F_{D\_U}$ and $F_{D\_D}$ are the mean drag forces on the up- and downstream cylinders in the IL direction, respectively; ρ is the fluid density; $C_{D\_U}$ and $C_{D\_D}$ denote the mean drag coefficients of the up- and downstream cylinders, respectively; $D$ and $l$ represent the cylinder diameter and length, respectively; and $U$ is the towing speed.

In the discussion of the drag forces and response amplitude properties of the tandem twin cylinders, $Re$ and reduced velocity ($Ur$) (Govardhan and Williamson, 2000, Roshko et al., 1975, Sheridan et al., 1995) are two of the key principal parameters, which are expressed as follows:

$$\mathrm{Re} = \frac{UD}{\upsilon} \tag{3}$$

$$U_r = \frac{U}{f_n D} \tag{4}$$

where $f_n$ denotes the natural frequency tested in water and υ is the kinematic viscosity coefficient. In this experiment, the ambient temperature is maintained at approximately 15°C; therefore, υ is approximately $1.14 \times 10^{-6} m^2/s$.

## 4. Results and discussion

### 4.1. Drag force on a single Cylinder—Benchmark test

The drag forces measured in the stationary single-cylinder towing tests are compared with those of the references (Achenbach, 1971). Fig. 5 shows a typical time history of the drag force for a stationary single cylinder at a flow velocity of 0.55 $m/s$. The whole drag force history can be divided into five stages: initial (zero force), acceleration, stable, deceleration and final (zero force).

In data processing, the drag force signals are firstly properly

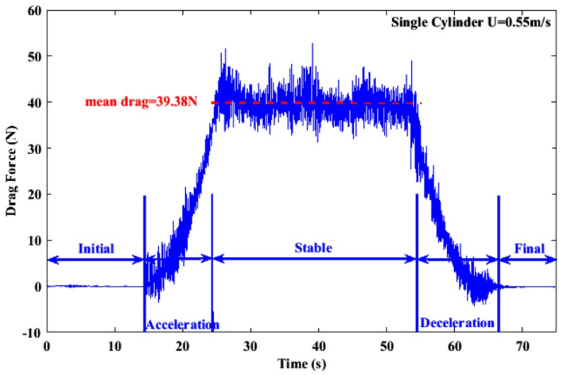


**Fig. 5.** Time history of measured drag force for a single cylinder

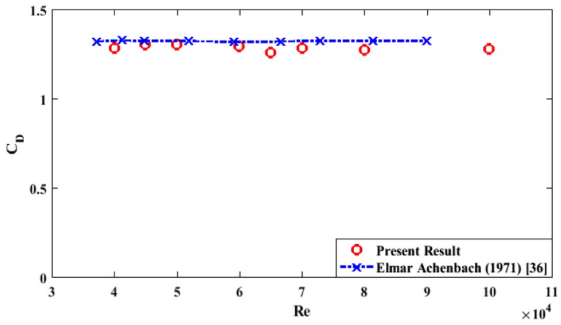


**Fig. 6.** Mean drag coefficient versus Reynolds number for a single cylinder

selected to maintain a pretty long period of stable. The mean drag coefficient as shown in Fig. 6 can be obtained through Eq. (1). It shows that the experimental results agree very well with the “smooth cylinder” in Achenbach's test (Achenbach, 1971).

### 4.2. Stationary model test of twin cylinders

Stationary towing tests of twin cylinders were conducted with three different spacing ratios of 2, 3 and 4; a typical time histories of the drag forces measured from these tests are shown in Fig. 7. The directions of the drag forces on the up- and downstream cylinders are opposite in the cases of λ equals to 2 and 3 where the force on the downstream cylinder is becoming "driving" instead of dragging. When λ increases to 4, the directions of the forces on both cylinders became the same . The variations in the wake modes of the upstream cylinder at different spacing ratio have been considered as the main reason for this “driving-dragging” shift. The downstream cylinder is surrounded by low-pressure water in the upstream side formed by the separated shear layers emanating from the upstream cylinder, and its downstream side is surrounded by the water formed by the separated layers emanating from itself. Then, in cases of smaller spacing ratios ($\lambda$= 2 and 3), the pressure on the upstream side is smaller than those on the downstream side for the downstream cylinder, which will lead to “diving” forces on it. When $\lambda$= 4 it becomes opposite (Ljungkrona and Sundén, 1993) which indicates the downstream cylinder is outside of the vortex formation region of the upstream cylinder (Sumner, 2010).

The drag coefficients on the up- and downstream cylinders from the tests are further summarized in Fig. 8, where the corresponding results on a single cylinder are also provided as references. As shown in the figure, the mean drag coefficient of the upstream cylinder is larger than

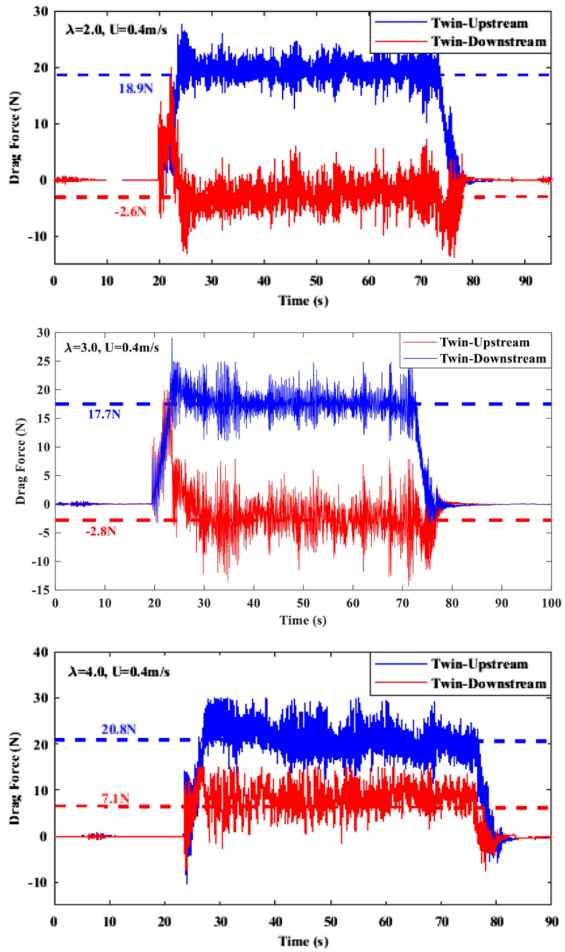


**Fig. 7.** Time history of drag force for twin cylinders in the stationary model test at a flow velocity of 0.4 *m/s*. The mean drag force shown in the figures are obtained based on the stable stage.

that of the downstream cylinder in all the cases due to the shielding effect, as expected. Compared with the single cylinder, the mean drag coefficient of the upstream cylinder is smaller when $\lambda$=2 and 3, whereas the coefficients are equal when $\lambda$= 4, which means that the effect of the downstream cylinder on the upstream cylinder is diminished when the spacing ratio reaches 4.

In addition, the total and difference of the drag forces on the up- and downstream cylinder are also important for the SFT. The former could be used in the global static analysis of the whole structure, and the latter is the key factor for the connection structure (i.e., the truss system) between the two tubes. Eq. (5) further defines the total drag force and the drag force difference.

$$\begin{cases} F_{D\_U} + F_{D\_D} = \frac{1}{2}\rho C_{D\_T} DlU^2 \\ F_{D\_U} - F_{D\_D} = \frac{1}{2}\rho C_{D\_\delta} DlU^2 \end{cases} \quad (5)$$

where $C_{D\_T}$ and $C_{D\_\delta}$ denote the coefficient of the total drag force and the drag force difference, respectively. As can be seen in Fig. 8, the $C_{D\_\delta}$ is much larger, even close to that of the single cylinder when $\lambda$=2 or 3. Meanwhile, the $C_{D\_T}$ is much smaller than twice of the coefficient of the

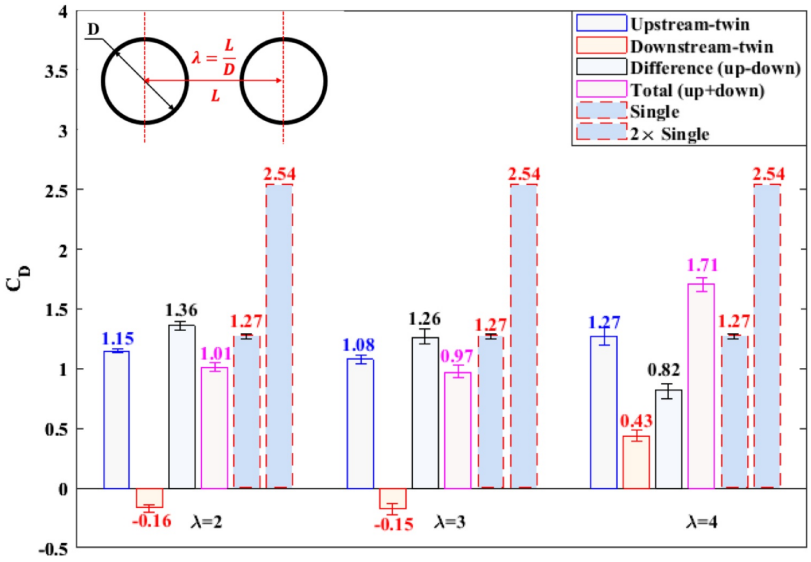


**Fig. 8.** Mean drag coefficient of a single cylinder and twin cylinders under different spacing ratios (the data displayed the average values of the mean drag coefficient, whereas the ranges on the bars show the mean drag coefficients obtained in the test with different flow velocities).

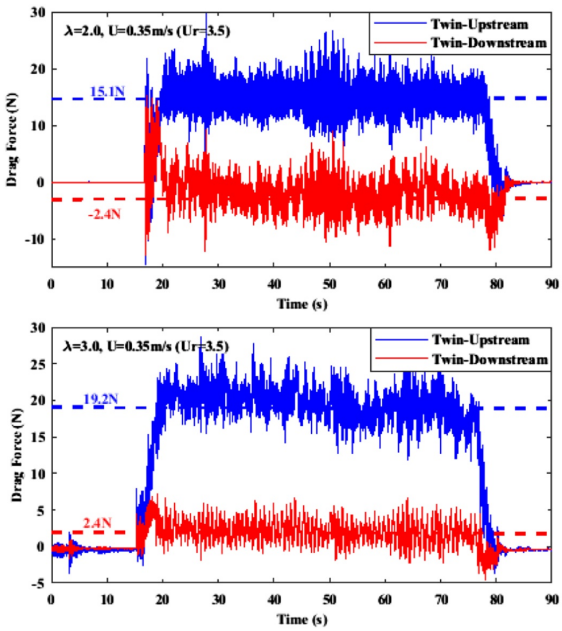


**Fig. 9.** Time history of drag forces on the up- and downstream cylinders under VIV conditions. The mean drag force shown in the figures are obtained based on the stable stage.

single cylinder.

### 4.3. VIV Effects on drag forces

The current and tide will generate alternatively shedding vortex around the cylinders, which could induce a significant periodical vibration (i.e., VIV), and then cause fatigue damage of the floating tunnel.

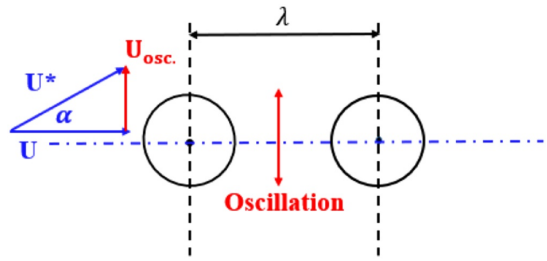


**Fig. 10.** Sketch of the relative flow velocity in the VIV condition.

VIV can heavily affect the drag forces in IL direction.

Fig. 9 shows the typical time histories of the drag forces on the up- and downstream cylinders under VIV conditions. Similar to the stationary results, the drag forces on the up- and downstream cylinders still act in opposing directions when $\lambda = 2$, but in the same direction when $\lambda = 3.0$ which is different from the stationary tests. That is to say, compared with the stationary testing conditions, VIV changed the pressure distribution around the downstream cylinder. The relative flow direction under VIV conditions is not horizontal anymore, as illustrated by Fig. 10. The angle ($\alpha$) between the incident flow velocity ($U$) and the relative flow velocity ($U^*$) heavily depends on the oscillation velocity ($U_{osc.}$). Therefore, in the cases where lock-in occurs (with relatively large response amplitude), the downstream cylinder is no longer immersed in the low-pressure region in the wake of the upstream cylinder, even when $\lambda = 3$. Fig. 11 summarizes the mean drag coefficients of the twin cylinders as a function of reduced velocity, and the drag coefficient of the single cylinder is also presented as a reference.

Generally speaking, the mean drag coefficients of both cylinders are heavily amplified by VIV compared with the stationary result. The maximum coefficients increase from 1.27 to 4.1 and 0.43 to 1.7 for up- and downstream cylinder, respectively. The mean drag coefficients of both cylinders are smaller than those of the single cylinder in most cases. The coefficient of the downstream cylinder is much smaller than that of the upstream cylinder because of the shielding effect induced

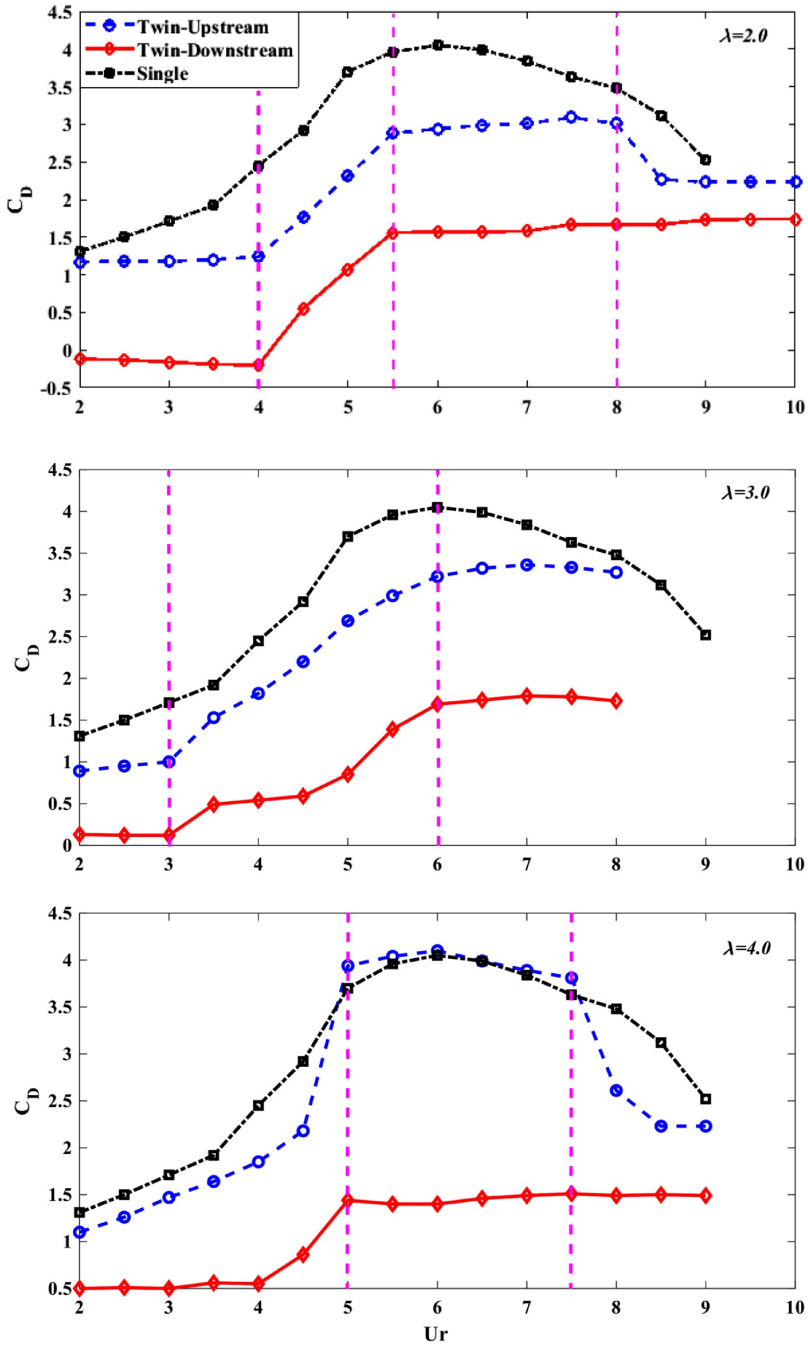


**Fig. 11.** Mean drag coefficients of the up- and downstream cylinders under spacing ratios of 2, 3 and 4, the values of *Ur* in this figure also corresponds to the Reynold number dividing $10^4$.

low flow velocity in the gap area.

The drag coefficient of the upstream cylinder strictly follows the trend of the response amplitude with respect to the reduced velocity, whereas the coefficient of downstream cylinder dose not, especially when $\lambda = 4$. In the cases with a small reduced velocity as $\lambda = 2$ and 3, the mean drag coefficients of both cylinders remain constant. These cases correspond to the zero VIV response amplitude, as shown in Fig. 12. In the following range of reduced velocity, the growth of the

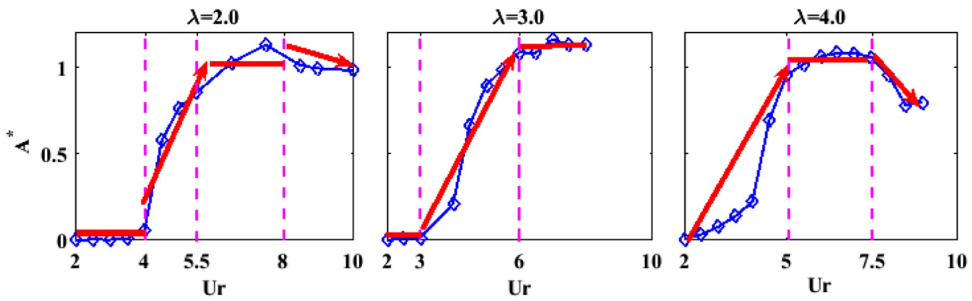


**Fig. 12.** VIV response amplitude of the twin cylinders for $\lambda$=2, 3 and 4 (Deng et al., 2020). The blue line shows the response amplitude and the red line shows the main trend ($A^* = A/D$, $A$ is the peak value of response displacement obtained by $rms \times \sqrt{2}$, $D$ is the cylinder diameter).

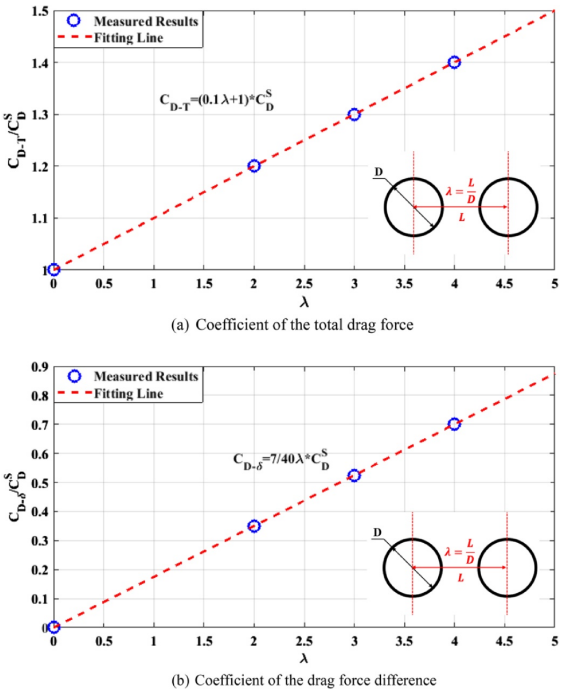


**Fig. 13.** Relations between the spacing ratio and $C_{D\_T}$ (a), $C_{D\_\delta}$ (b) with respect to the maximum drag coefficient of the single cylinder $C_D^S = 4$.

response amplitude leads to an increase of the mean drag coefficients on both cylinders except the downstream cylinder when λ = 4. When the response amplitude decreases, the drag on the upstream cylinder decreases, whereas the drag on the downstream cylinder remains constant.

The VIV amplified mean drag force will determine the largest steady horizontal deformation of the SFT. Therefore, the maximum values of the total drag force and the drag force difference defined in Eq. 5 are studied.

Based on the test results, a linear relation is found between the maximum value of the coefficient of the total drag force $C_{D\_T}$, the maximum value of the coefficient of the drag force difference $C_{D\_\delta}$, and the spacing ratio λ, as shown in Fig. 13.

$$\begin{cases} C_{D\_T} = (0.1\lambda + 1)^* C_D^S \\ C_{D\_\delta} = \frac{7}{40}\lambda^* C_D^S \end{cases} \quad (6)$$

where $C_D^S$ is the maximum drag coefficient of the single cylinder. If the spacing ratio λ decreases to zero, the total coefficient will be the same as the coefficient of the single cylinder, and the difference will be zero. However, the upper thresholds of these linear relations need further validation in the future. It should be noted here that the three maximum drag coefficients (total, difference and single cylinder) are mostly obtained in the cases of $Ur = 6$. Therefore, these relations could be adopted in the IL loads design of an SFT with a conservative view.

### 4.4. Submerged depth effect on drag

The above results provide a basic reference for the IL load design of the SFT in strong current and tide conditions with a large submergence. In the feasibility design phase shown in Fig. 1, because of the requirement of the navigational channel, the submergence of the SFT could vary within a range of 24.6 m to 32.6 m (Fjeld et al., 2012), and the design of the submerged depth of a SFT should also be a key factor.

Fig. 14 shows the VIV response amplitude of the twin cylinders segment versus the flow velocity under various submergences. It is clearly seen that both factors significantly affect the VIV response amplitude. Under the first three conditions of $h^* = 6.8$, 5.6 and 3.7, the amplitudes are very close , except for the cases when $h^* = 3.7$ while $Ur > 6.5$. It indicates that the response amplitude is irrespective of the submergence when $h^* \geq 5.6$ and $Ur \leq 8$. When $h^* = 2.7$, the amplitudes are similar to those of the former three conditions as $Ur \leq 4.5$ but becomes much smaller as the reduced velocity increases. The amplitude continues to decrease with a decrease in submergence. It can be attributed to the free surface effect, as shown in Fig. 15. The vortex shedding at the upper side near the free-surface can be depressed significantly (Bozkaya et al., 2011). The weak shear layers lead to a small lift force, which further result in a small oscillation amplitude.

In addition to the response amplitude, the mean drag coefficient is also heavily affected by the submergence. Fig. 16 shows the mean drag coefficient of the upstream cylinder under various submergences, which exhibits a similar trend as that of the response amplitude. This mean drag coefficient can reach approximately 4.1 when $Ur = 6$ and $h^* \geq 3.7$. There is a conspicuous decrease in the coefficient when $Ur = 7$ and $h^* = 3.7$. The critical reduced velocity, which is defined by the initiation of the free surface effect, is 4.5 and 3.0 when $h^*$ is 2.7 and 1.8, respectively. When the reduced velocity exceeds the critical value, the free surface effect could lead to a smaller drag coefficient with the decrease of the submergence. In addition, a weak relevance of flow velocity is observed when $h^* = 1.8$. Similar findings were found in the drag coefficient of the downstream cylinder, as shown in Fig. 17.

The critical value of reduced velocity, $Ur_{cri.}$ heavily depends on the submergence as well as the current velocity, strongly affects the drag coefficient by its influence on the VIV response amplitude. Froude number is usually used to describe the effect of the submergence. However, we did not find a critical case-independent $F_r$ value that can

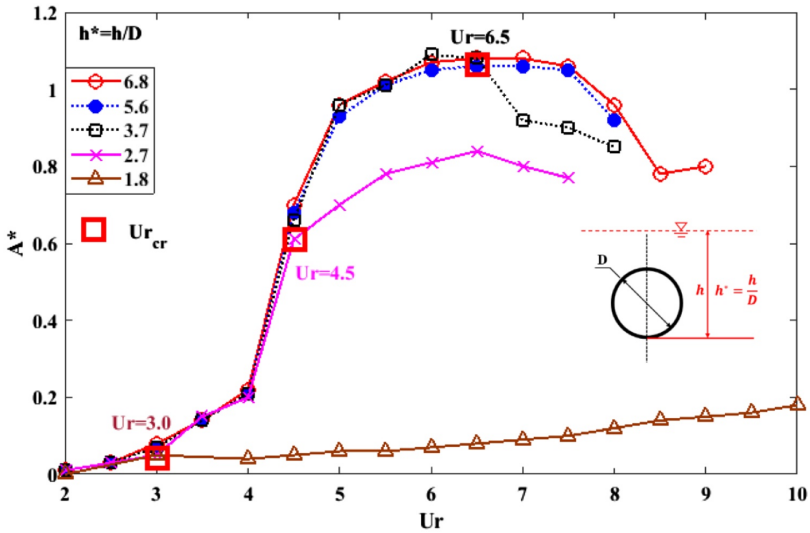


**Fig. 14.** Response amplitude versus flow velocity under various submergences, the values of *Ur* in this figure also corresponds to the Reynold number dividing $10^4$.

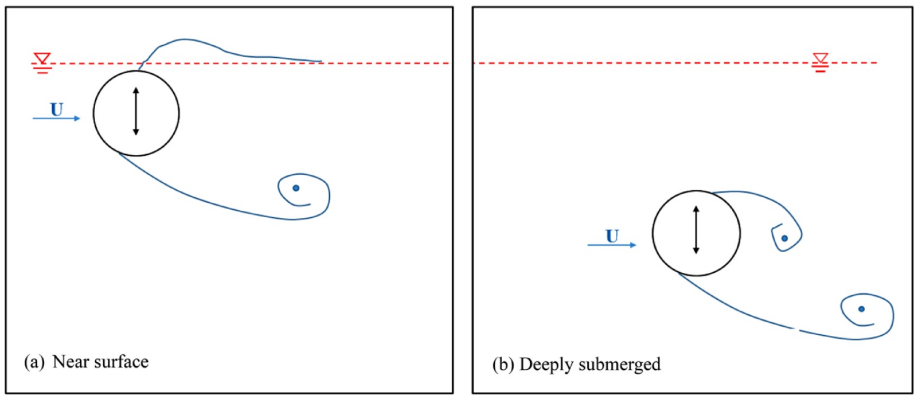


**Fig. 15.** Configuration of wake patterns for various submergences (Sumer, 2006).

divide the regions whether or not we should consider the free surface effect, as shown in Table 2.

Therefore, a new principal parameter in terms of flow velocity and submerged depth is introduced to describe the free surface effect on the VIV response amplitude and the drag force for any conditions.

In VIV studies of cylinders with large submergence, the reduced velocity ($Ur = \frac{U}{f_n D}$, which is represented in terms of the flow velocity, natural frequency and cylinder diameter) is a widely used key parameter. To illustrate the VIV features that occur in various submergences, a new parameter is defined:

$$h' = \frac{1}{Ur^*} = \frac{hf_n}{U} = \frac{h}{D}\frac{1}{Ur} \tag{7}$$

*h'* is a non-dimensional parameter (or normalized method) and proposed mainly to tell the readers whether or not to consider the free-surface effect at a specific submergence and current velocity. As can be seen in the Eq. 7, the non-dimensional indicator accounts for the effects of submergence, pipe diameter, natural frequency and flow velocity, which are the main parameters that may dominate the free surface effects.

Figs. 18–20 represent the drag coefficients of the up- and downstream cylinders and the response amplitude versus $h'$. The dashed lines highlight the critical value of $h'$. When $h' < 0.55$, the response amplitudes and drag coefficients are smaller than those of the cases with larger submergence at each reduced velocity. However, they are irrespective of the submergence when $h' > h'_{cri.}$. Therefore, the free surface effects must be considered when $h' < 0.55$; and, the hydrodynamic coefficient database obtained from the tests with large submergence is no longer suitable.

To provide a simple reference for the floating tunnel design, the maximum value of the coefficient of the total drag force $C_{D\_T}$ and the maximum value of the coefficient of the drag force difference $C_{D\_\delta}$ versus the submerged depth are shown in Fig. 21 with the spacing ratio of 4. In the range of $h^*$ from 1.8 to 3.7, the $C_{D\_T}$ and $C_{D\_\delta}$ are nearly linear with the submerged depth, which is briefly shown in Eq. (8).

$$\begin{cases} C_{D\_T} = (0.5h^* - 1)^* C_D^S \\ C_{D\_\delta} = (0.19h^* - 0.05)^* C_D^S \end{cases} \tag{8}$$

where $C_D^S$ is the maximum drag coefficient of a deeply submerged single cylinder under VIV conditions.

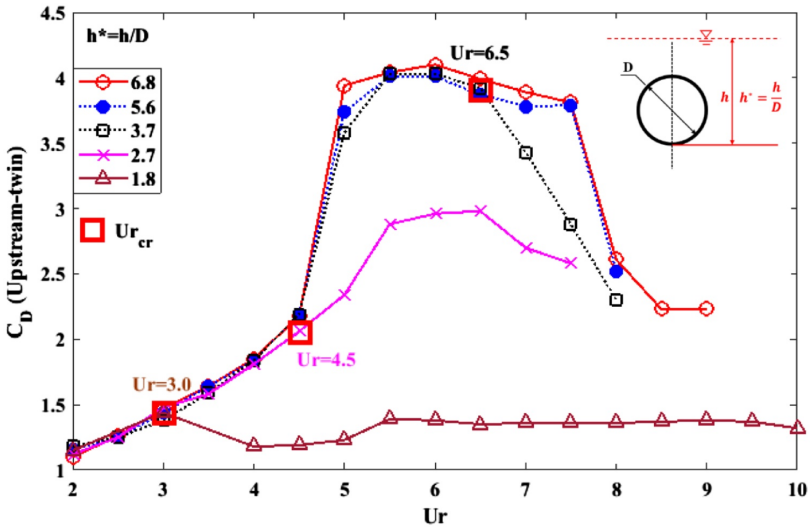


**Fig. 16.** Mean drag coefficient of the upstream cylinder under various submergences, the values of *Ur* in this figure also corresponds to the Reynold number dividing $10^4$.

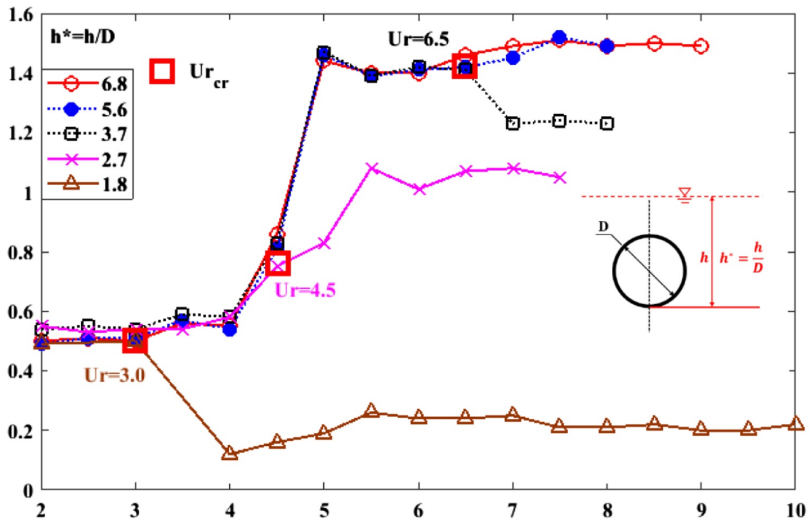


**Fig. 17.** Mean drag coefficient of the downstream cylinder under various submergences, the values of *Ur* in this figure also corresponds to the Reynold number dividing $10^4$.

**Table 2**
$F_r$ number and new defined submerged depth in the test.

| h* | $Ur_{cr}$ | $Fr_{cr} = Ur_{cr}\frac{f_n D}{\sqrt{gh}}$ |
|---|---|---|
| [-] | [-] | [-] |
| 6.8 | - | - |
| 5.6 | - | - |
| 3.7 | 6.5 | 0.34 |
| 2.7 | 4.5 | 0.28 |
| 1.8 | 3.0 | 0.23 |

The above discussion gives a qualitative result of the drag coefficients on twin cylinders with respect to the submerged depth. A new defined nondimensional depth is introduced to describe the free surface effect. However, the testing range of the flow velocity is limited. More cases are suggested to conduct to further validate the present findings, for which the critical ish′ 0.55. Particle image velocimetry (PIV) or computational fluid dynamics (CFD) results are also suggested to reveal the mechanics behind the findings presented here.

## 5. Conclusions

In this paper, the mean drag forces on rigidly connected tandem twin cylinders are discussed through experiments considering the

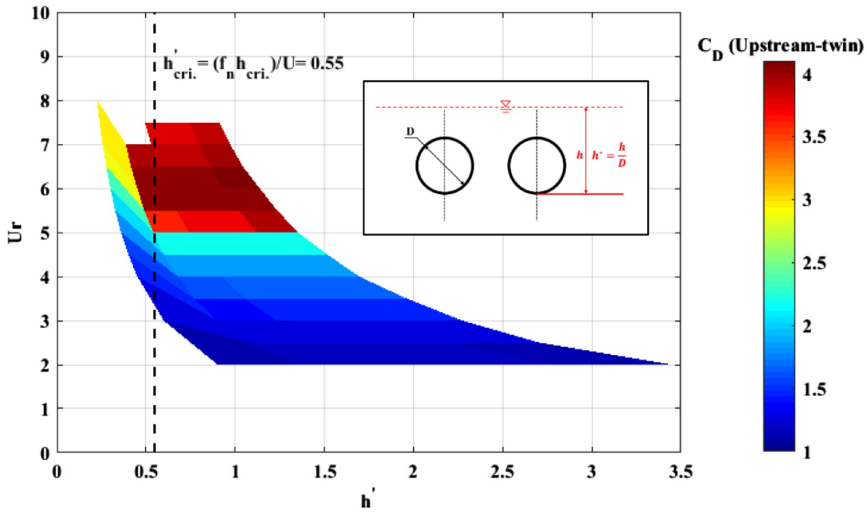


**Fig. 18.** Mean drag coefficient of the upstream cylinder versus the new defined submerged depth.

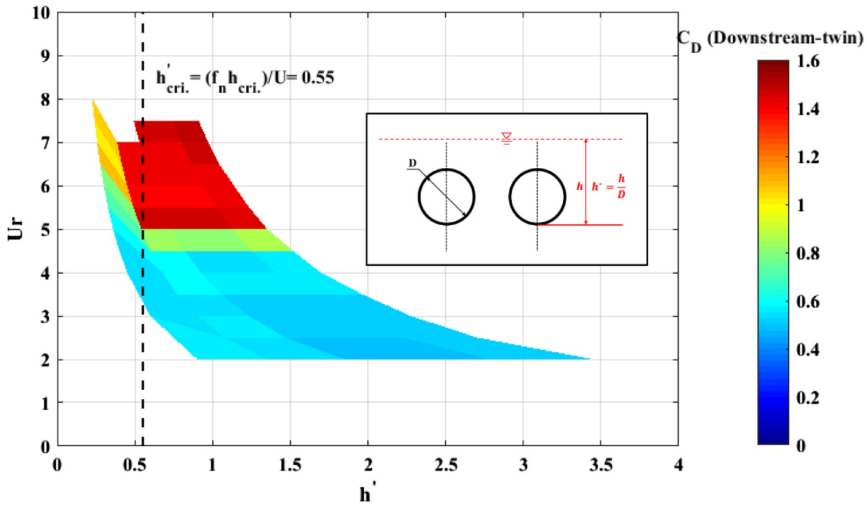


**Fig. 19.** Mean drag coefficient of the downstream cylinder versus the new defined submerged depth.

effects of spacing distance, VIV and submergence. Three spacing distances between the twin cylinders was tested in the experiments, and the VIV-generated drag amplification was discussed within the reduced velocity range of 2.0-10.0. Finally, experiments under different submergences of the model were performed to investigate the free surface effects on the drag forces. The main conclusions drawn from this study are as follows:

(1) In the stationary conditions, the directions of the drag forces on the two cylinders are opposite when $\lambda$=2.0 and 3.0, and the drag coefficient of the upstream cylinder is much larger than that of the downstream cylinder due to the shielding effect. Whereas when $\lambda$ is equal to or lager than 4, the shielding effects will disappear.
(2) In VIV conditions, both the vibration amplitudes and the spacing ratio heavily affect the drag forces on the twin cylinders. Under smaller spacing ratio, the drag force is nearly 3 times larger than that on the stationary one. Under VIV conditions, a novel feature was revealed namely that the total and difference drag coefficients of the twin cylinder can be described by a linear function of the spacing ratio.
(3) A measure for the submergence when the free surface effect needs to be taken into account is established by introducing a new non-dimensional submerged depth $h'$. A critical value of $h' = 0.55$ is found. Both the VIV response amplitude and the drag forces on the twin cylinders will decrease with decreasing of the submergence when $h' < 0.55$ at a specified reduced velocity. It then remains constant as $h' > 0.55$.

## CRediT authorship contribution statement

**Shi Deng:** Formal analysis, Writing - original draft, Investigation. **Haojie Ren:** Writing - review & editing, Investigation. **Yuwang Xu:** Writing - review & editing, Investigation. **Shixiao Fu:** Project administration, Supervision, Writing - review & editing. **Torgeir Moan:**

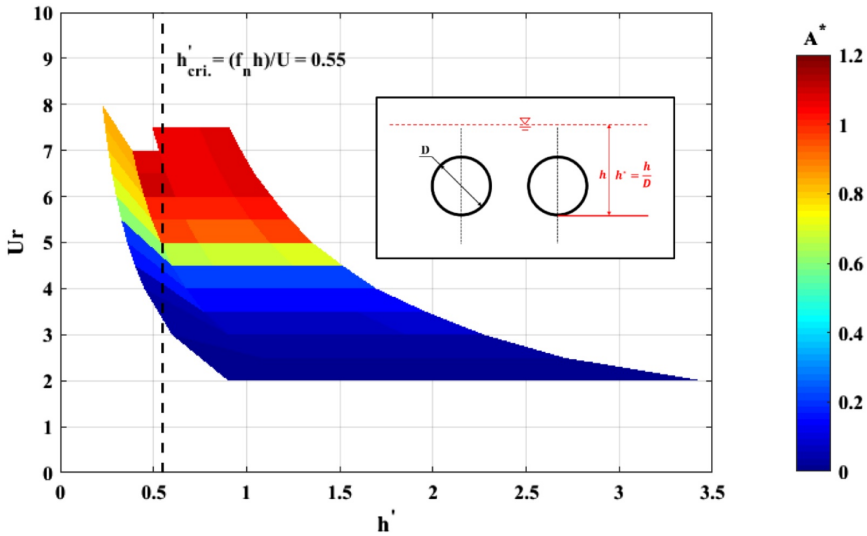


**Fig. 20.** Response amplitude versus the new defined submerged depth.

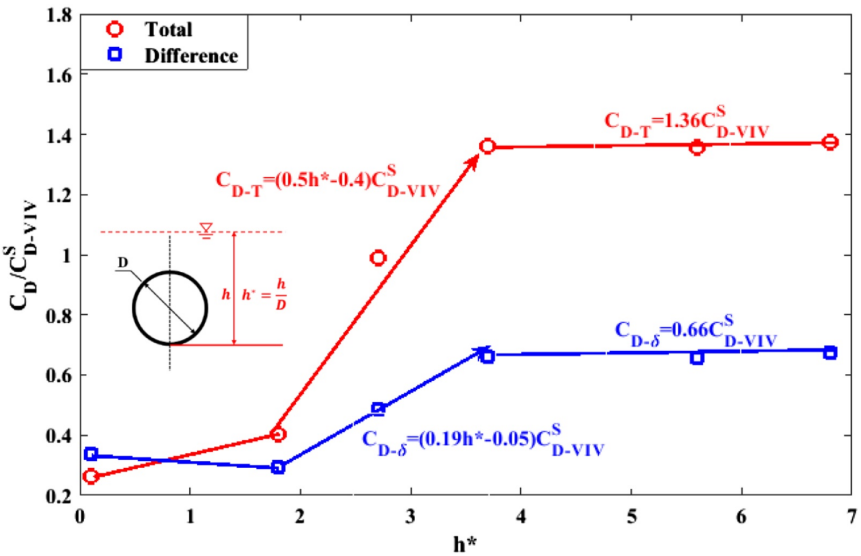


**Fig. 21.** Maximum value of the coefficient of the total drag force $C_{D\_T}$, maximum value of the coefficient of the drag force difference $C_{D\_\delta}$ versus the submerged water depth (in terms of the drag coefficient of a deeply submerged single cylinder, $C^S_{D\_VIV} = 4$).

Funding acquisition, Project administration, Supervision, Writing - review & editing. **Zhen Gao:** Supervision, Writing - review & editing.

## Declaration of Competing Interest

We wish to draw the attention of the Editor to the following facts which may be considered as potential conflicts of interest and to significant financial contributions to this work.

We confirm that the manuscript has been read and approved by all named authors and that there are no other persons who satisfied the criteria for authorship but are not listed. We further confirm that the order of authors listed in the manuscript has been approved by all of us.

We confirm that we have given due consideration to the protection of intellectual property associated with this work and that there are no impediments to publication, including the timing of publication, with respect to intellectual property. In so doing we confirm that we have followed the regulations of our institutions concerning intellectual property.

We understand that the Corresponding Author is the sole contact for the Editorial process (including Editorial Manager and direct communications with the office). They are responsible for communicating with the other authors about progress, submissions of revisions and final approval of proofs. We confirm that we have provided a current, correct email address which is accessible by the Corresponding Author and which has been configured to accept email from.

## Acknowledgments

The authors gratefully acknowledge the financial support by Norwegian Public Roads Administration andsupports from the Research Council of Norway through the Centre for Ships and Ocean Structures (CeSOS), Centre for Autonomous Marine Operations and Systems (AMOS, Project No. 223254), Department of Marine Technology (Project: 642030/69863000) at NTNU. The financial supports from the national Science Fund for Distinguished Young Scholars of China (No. 51825903), National Natural Science Foundation of China (51909159, U19B2013). Shanghai Science and Technology Program (No. 19XD1402000) are highly acknowledged.

## References

Achenbach, E., 1971. Influence of surface roughness on the cross-flow around a circular cylinder. J. Fluid Mech. 46, 321–335.
Alam, M.M., Moriya, M., Takai, K., Sakamoto, H., 2003. Fluctuating fluid forces acting on two circular cylinders in a tandem arrangement at a subcritical Reynolds number. J. Wind Eng. Ind. Aerodyn. 91, 139–154.
Alam, M.M., Sakamoto, H., Zhou, Y., 2005. Determination of flow configurations and fluid forces acting on two staggered circular cylinders of equal diameter in cross-flow. J. Fluids Struct. 21, 363–394.
Alam, M.M., Zhou, Y., 2007. Phase lag between vortex shedding from two tandem bluff bodies. J. Fluids Struct. 23, 339–347.
Borazjani, I., Sotiropoulos, F., 2009. Vortex-induced vibrations of two cylinders in tandem arrangement in the proximity–wake interference region. J. Fluid Mech. 621, 321–364.
Bozkaya, C., Kocabiyik, S., Mironova, L., Gubanov, O., 2011. Streamwise oscillations of a cylinder beneath a free surface: free surface effects on vortex formation modes. J. Comput. Appl. Math. 235, 4780–4795.
Carmo, B., Meneghini, J., Sherwin, S., 2010. Possible states in the flow around two circular cylinders in tandem with separations in the vicinity of the drag inversion spacing. Phys. Fluids 22, 054101.
Carmo, B.S., Meneghini, J.R., Sherwin, S.J., 2010. Secondary instabilities in the flow around two circular cylinders in tandem. J. Fluid Mech. 644, 395–431.
Chen, W., Ji, C., Williams, J., Xu, D., Yang, L., Cui, Y., 2018. Vortex-induced vibrations of three tandem cylinders in laminar cross-flow: Vibration response and galloping mechanism. J. Fluids Struct. 78, 215–238.
Chu, C.-R., Lin, Y.-A., Wu, T.-R., Wang, C.-Y., 2018. Hydrodynamic force of a circular cylinder close to the water surface. Comput. Fluids 171, 154–165.
Chung, M.-H., 2016. Two-degree-of-freedom vortex induced vibration of low-mass horizontal circular cylinder near a free surface at low Reynolds number. Int. J. Heat Fluid Flow 57, 58–78.
Deng, S., Ren, H., Xu, Y., Fu, S., Moan, T., Gao, Z., 2020. Experimental study of vortex-induced vibration of a twin-tube submerged floating tunnel segment model. J. Fluids Struct. 94, 102908.
Fjeld A, Soreide TH, Haugerud SA. Feasibility study for crossing the Sognefjord - Submerged floating tunnel. Norwegian Public Road Administration (NPRA). 2012, https://www.vegvesen.no/en/Home, download on 1st Feb. 2019.
Fu, S., Xu, Y., Hu, K., Zhang, Y., 2013. Experimental investigation on hydrodynamics of floating cylinder in oscillatory and steady flows by forced oscillation test. Mar. struct. 34, 41–55.
Gopalkrishnan, R., 1993. Vortex-induced forces on oscillating bluff cylinders. Woods Hole Oceanographic Institution, MA.
Govardhan, R., Williamson, C., 2000. Modes of vortex formation and frequency response of a freely vibrating cylinder. J. Fluid Mech. 420, 85–130.
Huang, S, Herfjord, K., 2013. Experimental investigation of the forces and motion responses of two interfering VIV circular cylinders at various tandem and staggered positions. Appl. Ocean Res. 43, 264–273.
Huang, S., Sworn, A., 2011. Some observations of two interfering VIV circular cylinders of unequal diameters in tandem. J. Hydrodyn. Ser. B (English Ed.) 23, 535–543.
Jhingran V.G.Drag amplification and fatigue damage in vortex-induced vibrations: Massachusetts institute of technology; 2008.
Kaiktsis, L., Triantafyllou, G., Özbas, M., 2007. Excitation, inertia, and drag forces on a cylinder vibrating transversely to a steady flow. J. Fluids Struct. 23, 1–21.
Khalak, A., Williamson, C., 1997. Fluid forces and dynamics of a hydroelastic structure with very low mass and damping. J. Fluids Struct. 11, 973–982.
Khalak, A., Williamson, C., 1999. Motions, forces and mode transitions in vortex-induced vibrations at low mass-damping. J. Fluids Struct. 13, 813–851.
Kitagawa, T., Ohta, H., 2008. Numerical investigation on flow around circular cylinders in tandem arrangement at a subcritical Reynolds number. J. Fluids Struct. 24, 680–699.
Ljungkrona, L., Sundén, B., 1993. Flow visualization and surface pressure measurement on two tubes in an inline arrangement. Exp. Therm. Fluid Sci. 6, 15–27.
Meneghini, J.R., Saltara, F., Siqueira, C., Ferrari Jr, J., 2001. Numerical simulation of flow interference between two circular cylinders in tandem and side-by-side arrangements. J. Fluids Struct. 15, 327–350.
Papaioannou, G., Yue, D., Triantafyllou, M., Karniadakis, G., 2008. On the effect of spacing on the vortex-induced vibrations of two tandem cylinders. J. Fluids Struct. 24, 833–854.
Reichl, P., Hourigan, K., Thompson, M., 2005. Flow past a cylinder close to a free surface. J. Fluid Mech. 533, 269–296.
Ren, H., Xu, Y., Zhang, M., Deng, S., Li, S., Fu, S., et al., 2019. Hydrodynamic forces on a partially submerged cylinder at high Reynolds number in a steady flow. Appl. Ocean Res. 88, 160–169.
Roshko, A., Steinolfson, A., Chattoorgoon, V., 1975. Flow Forces on a Cylinder Near a Wall or Near Another Cylinder. California Inst of Tech Pasadena.
Sareen, A., Zhao, J., Sheridan, J., Hourigan, K., Thompson, M., 2018. Vortex-induced vibrations of a sphere close to a free surface. J. Fluid Mech. 846, 1023–1058.
Schewe, G., 1983. On the force fluctuations acting on a circular cylinder in crossflow from subcritical up to transcritical Reynolds numbers. J. Fluid Mech. 133, 265–285.
Sheridan, J., Lin, J.C., Rockwell, D., 1995. Metastable states of a cylinder wake adjacent to a free surface. Phys. Fluids 7, 2099–2101.
Sheridan, J., Lin, J.-C., Rockwell, D., 1997. Flow past a cylinder close to a free surface. J. Fluid Mech. 330, 1–30.
Song, L., Fu, S., Cao, J., Ma, L., Wu, J., 2016. An investigation into the hydrodynamics of a flexible riser undergoing vortex-induced vibration. J. Fluids Struct. 63, 325–350.
Song, L., Fu, S., Dai, S., Zhang, M., Chen, Y., 2016. Distribution of drag force coefficient along a flexible riser undergoing VIV in sheared flow. Ocean Eng. 126, 1–11.
Sumer, B.M., 2006. Hydrodynamics Around Cylindrical Strucures. World scientific.
Sumner, D., 2010. Two circular cylinders in cross-flow: a review. J. Fluids Struct. 26, 849–899.
Vandiver, J.K., 1983. Drag coefficients of long flexible cylinders. In: Offshore Technology Conference: Offshore Technology Conference.

## D.3 Paper 3

**Paper 3:**
Deng S, Xu Y, Ren H, Fu S, Li S, Moan T, Gao Z. Numerical simulation of wave-induced hydroelasticity and flow-induced vibration of a twin-tube submerged floating tunnel. *prepare to submit.*

**Previous PhD theses published at the Department of Marine Technology (earlier: Faculty of Marine Technology) NORWEGIAN UNIVERSITY OF SCIENCE AND TECHNOLOGY**

| Report No. | Author | Title |
|---|---|---|
| | Kavlie, Dag | Optimization of Plane Elastic Grillages, 1967 |
| | Hansen, Hans R. | Man-Machine Communication and Data-Storage Methods in Ship Structural Design, 1971 |
| | Gisvold, Kaare M. | A Method for non-linear mixed -integer programming and its Application to Design Problems, 1971 |
| | Lund, Sverre | Tanker Frame Optimalization by means of SUMT-Transformation and Behaviour Models, 1971 |
| | Vinje, Tor | On Vibration of Spherical Shells Interacting with Fluid, 1972 |
| | Lorentz, Jan D. | Tank Arrangement for Crude Oil Carriers in Accordance with the new Anti-Pollution Regulations, 1975 |
| | Carlsen, Carl A. | Computer-Aided Design of Tanker Structures, 1975 |
| | Larsen, Carl M. | Static and Dynamic Analysis of Offshore Pipelines during Installation, 1976 |
| UR-79-01 | Brigt Hatlestad, MK | The finite element method used in a fatigue evaluation of fixed offshore platforms. (Dr.Ing. Thesis) |
| UR-79-02 | Erik Pettersen, MK | Analysis and design of cellular structures. (Dr.Ing. Thesis) |
| UR-79-03 | Sverre Valsgård, MK | Finite difference and finite element methods applied to nonlinear analysis of plated structures. (Dr.Ing. Thesis) |
| UR-79-04 | Nils T. Nordsve, MK | Finite element collapse analysis of structural members considering imperfections and stresses due to fabrication. (Dr.Ing. Thesis) |
| UR-79-05 | Ivar J. Fylling, MK | Analysis of towline forces in ocean towing systems. (Dr.Ing. Thesis) |
| UR-80-06 | Nils Sandsmark, MM | Analysis of Stationary and Transient Heat Conduction by the Use of the Finite Element Method. (Dr.Ing. Thesis) |
| UR-80-09 | Sverre Haver, MK | Analysis of uncertainties related to the stochastic modeling of ocean waves. (Dr.Ing. Thesis) |
| UR-81-15 | Odland, Jonas | On the Strength of welded Ring stiffened cylindrical Shells primarily subjected to axial Compression |
| UR-82-17 | Engesvik, Knut | Analysis of Uncertainties in the fatigue Capacity of |

| | | |
|---|---|---|
| | | Welded Joints |
| UR-82-18 | Rye, Henrik | Ocean wave groups |
| UR-83-30 | Eide, Oddvar Inge | On Cumulative Fatigue Damage in Steel Welded Joints |
| UR-83-33 | Mo, Olav | Stochastic Time Domain Analysis of Slender Offshore Structures |
| UR-83-34 | Amdahl, Jørgen | Energy absorption in Ship-platform impacts |
| UR-84-37 | Mørch, Morten | Motions and mooring forces of semi submersibles as determined by full-scale measurements and theoretical analysis |
| UR-84-38 | Soares, C. Guedes | Probabilistic models for load effects in ship structures |
| UR-84-39 | Aarsnes, Jan V. | Current forces on ships |
| UR-84-40 | Czujko, Jerzy | Collapse Analysis of Plates subjected to Biaxial Compression and Lateral Load |
| UR-85-46 | Alf G. Engseth, MK | Finite element collapse analysis of tubular steel offshore structures. (Dr.Ing. Thesis) |
| UR-86-47 | Dengody Sheshappa, MP | A Computer Design Model for Optimizing Fishing Vessel Designs Based on Techno-Economic Analysis. (Dr.Ing. Thesis) |
| UR-86-48 | Vidar Aanesland, MH | A Theoretical and Numerical Study of Ship Wave Resistance. (Dr.Ing. Thesis) |
| UR-86-49 | Heinz-Joachim Wessel, MK | Fracture Mechanics Analysis of Crack Growth in Plate Girders. (Dr.Ing. Thesis) |
| UR-86-50 | Jon Taby, MK | Ultimate and Post-ultimate Strength of Dented Tubular Members. (Dr.Ing. Thesis) |
| UR-86-51 | Walter Lian, MH | A Numerical Study of Two-Dimensional Separated Flow Past Bluff Bodies at Moderate KC-Numbers. (Dr.Ing. Thesis) |
| UR-86-52 | Bjørn Sortland, MH | Force Measurements in Oscillating Flow on Ship Sections and Circular Cylinders in a U-Tube Water Tank. (Dr.Ing. Thesis) |
| UR-86-53 | Kurt Strand, MM | A System Dynamic Approach to One-dimensional Fluid Flow. (Dr.Ing. Thesis) |
| UR-86-54 | Arne Edvin Løken, MH | Three Dimensional Second Order Hydrodynamic Effects on Ocean Structures in Waves. (Dr.Ing. Thesis) |
| UR-86-55 | Sigurd Falch, MH | A Numerical Study of Slamming of Two-Dimensional Bodies. (Dr.Ing. Thesis) |
| UR-87-56 | Arne Braathen, MH | Application of a Vortex Tracking Method to the Prediction of Roll Damping of a Two-Dimension Floating Body. (Dr.Ing. Thesis) |

| | | |
|---|---|---|
| UR-87-57 | Bernt Leira, MK | Gaussian Vector Processes for Reliability Analysis involving Wave-Induced Load Effects. (Dr.Ing. Thesis) |
| UR-87-58 | Magnus Småvik, MM | Thermal Load and Process Characteristics in a Two-Stroke Diesel Engine with Thermal Barriers (in Norwegian). (Dr.Ing. Thesis) |
| MTA-88-59 | Bernt Arild Bremdal, MP | An Investigation of Marine Installation Processes – A Knowledge - Based Planning Approach. (Dr.Ing. Thesis) |
| MTA-88-60 | Xu Jun, MK | Non-linear Dynamic Analysis of Space-framed Offshore Structures. (Dr.Ing. Thesis) |
| MTA-89-61 | Gang Miao, MH | Hydrodynamic Forces and Dynamic Responses of Circular Cylinders in Wave Zones. (Dr.Ing. Thesis) |
| MTA-89-62 | Martin Greenhow, MH | Linear and Non-Linear Studies of Waves and Floating Bodies. Part I and Part II. (Dr.Techn. Thesis) |
| MTA-89-63 | Chang Li, MH | Force Coefficients of Spheres and Cubes in Oscillatory Flow with and without Current. (Dr.Ing. Thesis |
| MTA-89-64 | Hu Ying, MP | A Study of Marketing and Design in Development of Marine Transport Systems. (Dr.Ing. Thesis) |
| MTA-89-65 | Arild Jæger, MH | Seakeeping, Dynamic Stability and Performance of a Wedge Shaped Planing Hull. (Dr.Ing. Thesis) |
| MTA-89-66 | Chan Siu Hung, MM | The dynamic characteristics of tilting-pad bearings |
| MTA-89-67 | Kim Wikstrøm, MP | Analysis av projekteringen for ett offshore projekt. (Licenciat-avhandling) |
| MTA-89-68 | Jiao Guoyang, MK | Reliability Analysis of Crack Growth under Random Loading, considering Model Updating. (Dr.Ing. Thesis) |
| MTA-89-69 | Arnt Olufsen, MK | Uncertainty and Reliability Analysis of Fixed Offshore Structures. (Dr.Ing. Thesis) |
| MTA-89-70 | Wu Yu-Lin, MR | System Reliability Analyses of Offshore Structures using improved Truss and Beam Models. (Dr.Ing. Thesis) |
| MTA-90-71 | Jan Roger Hoff, MH | Three-dimensional Green function of a vessel with forward speed in waves. (Dr.Ing. Thesis) |
| MTA-90-72 | Rong Zhao, MH | Slow-Drift Motions of a Moored Two-Dimensional Body in Irregular Waves. (Dr.Ing. Thesis) |
| MTA-90-73 | Atle Minsaas, MP | Economical Risk Analysis. (Dr.Ing. Thesis) |
| MTA-90-74 | Knut-Aril Farnes, MK | Long-term Statistics of Response in Non-linear Marine Structures. (Dr.Ing. Thesis) |
| MTA-90-75 | Torbjørn Sotberg, MK | Application of Reliability Methods for Safety Assessment of Submarine Pipelines. (Dr.Ing. |

| | | |
|---|---|---|
| | | Thesis) |
| MTA-90-76 | Zeuthen, Steffen, MP | SEAMAID. A computational model of the design process in a constraint-based logic programming environment. An example from the offshore domain. (Dr.Ing. Thesis) |
| MTA-91-77 | Haagensen, Sven, MM | Fuel Dependant Cyclic Variability in a Spark Ignition Engine - An Optical Approach. (Dr.Ing. Thesis) |
| MTA-91-78 | Løland, Geir, MH | Current forces on and flow through fish farms. (Dr.Ing. Thesis) |
| MTA-91-79 | Hoen, Christopher, MK | System Identification of Structures Excited by Stochastic Load Processes. (Dr.Ing. Thesis) |
| MTA-91-80 | Haugen, Stein, MK | Probabilistic Evaluation of Frequency of Collision between Ships and Offshore Platforms. (Dr.Ing. Thesis) |
| MTA-91-81 | Sødahl, Nils, MK | Methods for Design and Analysis of Flexible Risers. (Dr.Ing. Thesis) |
| MTA-91-82 | Ormberg, Harald, MK | Non-linear Response Analysis of Floating Fish Farm Systems. (Dr.Ing. Thesis) |
| MTA-91-83 | Marley, Mark J., MK | Time Variant Reliability under Fatigue Degradation. (Dr.Ing. Thesis) |
| MTA-91-84 | Krokstad, Jørgen R., MH | Second-order Loads in Multidirectional Seas. (Dr.Ing. Thesis) |
| MTA-91-85 | Molteberg, Gunnar A., MM | The Application of System Identification Techniques to Performance Monitoring of Four Stroke Turbocharged Diesel Engines. (Dr.Ing. Thesis) |
| MTA-92-86 | Mørch, Hans Jørgen Bjelke, MH | Aspects of Hydrofoil Design: with Emphasis on Hydrofoil Interaction in Calm Water. (Dr.Ing. Thesis) |
| MTA-92-87 | Chan Siu Hung, MM | Nonlinear Analysis of Rotordynamic Instabilities in Highspeed Turbomachinery. (Dr.Ing. Thesis) |
| MTA-92-88 | Bessason, Bjarni, MK | Assessment of Earthquake Loading and Response of Seismically Isolated Bridges. (Dr.Ing. Thesis) |
| MTA-92-89 | Langli, Geir, MP | Improving Operational Safety through exploitation of Design Knowledge - an investigation of offshore platform safety. (Dr.Ing. Thesis) |
| MTA-92-90 | Sævik, Svein, MK | On Stresses and Fatigue in Flexible Pipes. (Dr.Ing. Thesis) |
| MTA-92-91 | Ask, Tor Ø., MM | Ignition and Flame Growth in Lean Gas-Air Mixtures. An Experimental Study with a Schlieren System. (Dr.Ing. Thesis) |
| MTA-86-92 | Hessen, Gunnar, MK | Fracture Mechanics Analysis of Stiffened Tubular Members. (Dr.Ing. Thesis) |

| | | |
|---|---|---|
| MTA-93-93 | Steinebach, Christian, MM | Knowledge Based Systems for Diagnosis of Rotating Machinery. (Dr.Ing. Thesis) |
| MTA-93-94 | Dalane, Jan Inge, MK | System Reliability in Design and Maintenance of Fixed Offshore Structures. (Dr.Ing. Thesis) |
| MTA-93-95 | Steen, Sverre, MH | Cobblestone Effect on SES. (Dr.Ing. Thesis) |
| MTA-93-96 | Karunakaran, Daniel, MK | Nonlinear Dynamic Response and Reliability Analysis of Drag-dominated Offshore Platforms. (Dr.Ing. Thesis) |
| MTA-93-97 | Hagen, Arnulf, MP | The Framework of a Design Process Language. (Dr.Ing. Thesis) |
| MTA-93-98 | Nordrik, Rune, MM | Investigation of Spark Ignition and Autoignition in Methane and Air Using Computational Fluid Dynamics and Chemical Reaction Kinetics. A Numerical Study of Ignition Processes in Internal Combustion Engines. (Dr.Ing. Thesis) |
| MTA-94-99 | Passano, Elizabeth, MK | Efficient Analysis of Nonlinear Slender Marine Structures. (Dr.Ing. Thesis) |
| MTA-94-100 | Kvålsvold, Jan, MH | Hydroelastic Modelling of Wetdeck Slamming on Multihull Vessels. (Dr.Ing. Thesis) |
| MTA-94-102 | Bech, Sidsel M., MK | Experimental and Numerical Determination of Stiffness and Strength of GRP/PVC Sandwich Structures. (Dr.Ing. Thesis) |
| MTA-95-103 | Paulsen, Hallvard, MM | A Study of Transient Jet and Spray using a Schlieren Method and Digital Image Processing. (Dr.Ing. Thesis) |
| MTA-95-104 | Hovde, Geir Olav, MK | Fatigue and Overload Reliability of Offshore Structural Systems, Considering the Effect of Inspection and Repair. (Dr.Ing. Thesis) |
| MTA-95-105 | Wang, Xiaozhi, MK | Reliability Analysis of Production Ships with Emphasis on Load Combination and Ultimate Strength. (Dr.Ing. Thesis) |
| MTA-95-106 | Ulstein, Tore, MH | Nonlinear Effects of a Flexible Stern Seal Bag on Cobblestone Oscillations of an SES. (Dr.Ing. Thesis) |
| MTA-95-107 | Solaas, Frøydis, MH | Analytical and Numerical Studies of Sloshing in Tanks. (Dr.Ing. Thesis) |
| MTA-95-108 | Hellan, Øyvind, MK | Nonlinear Pushover and Cyclic Analyses in Ultimate Limit State Design and Reassessment of Tubular Steel Offshore Structures. (Dr.Ing. Thesis) |
| MTA-95-109 | Hermundstad, Ole A., MK | Theoretical and Experimental Hydroelastic Analysis of High Speed Vessels. (Dr.Ing. Thesis) |
| MTA-96-110 | Bratland, Anne K., MH | Wave-Current Interaction Effects on Large-Volume Bodies in Water of Finite Depth. (Dr.Ing. Thesis) |
| MTA-96-111 | Herfjord, Kjell, MH | A Study of Two-dimensional Separated Flow by a Combination of the Finite Element Method and |

| | | |
|---|---|---|
| | | Navier-Stokes Equations. (Dr.Ing. Thesis) |
| MTA-96-112 | Æsøy, Vilmar, MM | Hot Surface Assisted Compression Ignition in a Direct Injection Natural Gas Engine. (Dr.Ing. Thesis) |
| MTA-96-113 | Eknes, Monika L., MK | Escalation Scenarios Initiated by Gas Explosions on Offshore Installations. (Dr.Ing. Thesis) |
| MTA-96-114 | Erikstad, Stein O., MP | A Decision Support Model for Preliminary Ship Design. (Dr.Ing. Thesis) |
| MTA-96-115 | Pedersen, Egil, MH | A Nautical Study of Towed Marine Seismic Streamer Cable Configurations. (Dr.Ing. Thesis) |
| MTA-97-116 | Moksnes, Paul O., MM | Modelling Two-Phase Thermo-Fluid Systems Using Bond Graphs. (Dr.Ing. Thesis) |
| MTA-97-117 | Halse, Karl H., MK | On Vortex Shedding and Prediction of Vortex-Induced Vibrations of Circular Cylinders. (Dr.Ing. Thesis) |
| MTA-97-118 | Igland, Ragnar T., MK | Reliability Analysis of Pipelines during Laying, considering Ultimate Strength under Combined Loads. (Dr.Ing. Thesis) |
| MTA-97-119 | Pedersen, Hans-P., MP | Levendefiskteknologi for fiskefartøy. (Dr.Ing. Thesis) |
| MTA-98-120 | Vikestad, Kyrre, MK | Multi-Frequency Response of a Cylinder Subjected to Vortex Shedding and Support Motions. (Dr.Ing. Thesis) |
| MTA-98-121 | Azadi, Mohammad R. E., MK | Analysis of Static and Dynamic Pile-Soil-Jacket Behaviour. (Dr.Ing. Thesis) |
| MTA-98-122 | Ulltang, Terje, MP | A Communication Model for Product Information. (Dr.Ing. Thesis) |
| MTA-98-123 | Torbergsen, Erik, MM | Impeller/Diffuser Interaction Forces in Centrifugal Pumps. (Dr.Ing. Thesis) |
| MTA-98-124 | Hansen, Edmond, MH | A Discrete Element Model to Study Marginal Ice Zone Dynamics and the Behaviour of Vessels Moored in Broken Ice. (Dr.Ing. Thesis) |
| MTA-98-125 | Videiro, Paulo M., MK | Reliability Based Design of Marine Structures. (Dr.Ing. Thesis) |
| MTA-99-126 | Mainçon, Philippe, MK | Fatigue Reliability of Long Welds Application to Titanium Risers. (Dr.Ing. Thesis) |
| MTA-99-127 | Haugen, Elin M., MH | Hydroelastic Analysis of Slamming on Stiffened Plates with Application to Catamaran Wetdecks. (Dr.Ing. Thesis) |
| MTA-99-128 | Langhelle, Nina K., MK | Experimental Validation and Calibration of Nonlinear Finite Element Models for Use in Design of Aluminium Structures Exposed to Fire. (Dr.Ing. Thesis) |
| MTA-99- | Berstad, Are J., MK | Calculation of Fatigue Damage in Ship Structures. |

| | | |
|---|---|---|
| 129 | | (Dr.Ing. Thesis) |
| MTA-99-130 | Andersen, Trond M., MM | Short Term Maintenance Planning. (Dr.Ing. Thesis) |
| MTA-99-131 | Tveiten, Bård Wathne, MK | Fatigue Assessment of Welded Aluminium Ship Details. (Dr.Ing. Thesis) |
| MTA-99-132 | Søreide, Fredrik, MP | Applications of underwater technology in deep water archaeology. Principles and practice. (Dr.Ing. Thesis) |
| MTA-99-133 | Tønnessen, Rune, MH | A Finite Element Method Applied to Unsteady Viscous Flow Around 2D Blunt Bodies With Sharp Corners. (Dr.Ing. Thesis) |
| MTA-99-134 | Elvekrok, Dag R., MP | Engineering Integration in Field Development Projects in the Norwegian Oil and Gas Industry. The Supplier Management of Norne. (Dr.Ing. Thesis) |
| MTA-99-135 | Fagerholt, Kjetil, MP | Optimeringsbaserte Metoder for Ruteplanlegging innen skipsfart. (Dr.Ing. Thesis) |
| MTA-99-136 | Bysveen, Marie, MM | Visualization in Two Directions on a Dynamic Combustion Rig for Studies of Fuel Quality. (Dr.Ing. Thesis) |
| MTA-2000-137 | Storteig, Eskild, MM | Dynamic characteristics and leakage performance of liquid annular seals in centrifugal pumps. (Dr.Ing. Thesis) |
| MTA-2000-138 | Sagli, Gro, MK | Model uncertainty and simplified estimates of long term extremes of hull girder loads in ships. (Dr.Ing. Thesis) |
| MTA-2000-139 | Tronstad, Harald, MK | Nonlinear analysis and design of cable net structures like fishing gear based on the finite element method. (Dr.Ing. Thesis) |
| MTA-2000-140 | Kroneberg, André, MP | Innovation in shipping by using scenarios. (Dr.Ing. Thesis) |
| MTA-2000-141 | Haslum, Herbjørn Alf, MH | Simplified methods applied to nonlinear motion of spar platforms. (Dr.Ing. Thesis) |
| MTA-2001-142 | Samdal, Ole Johan, MM | Modelling of Degradation Mechanisms and Stressor Interaction on Static Mechanical Equipment Residual Lifetime. (Dr.Ing. Thesis) |
| MTA-2001-143 | Baarholm, Rolf Jarle, MH | Theoretical and experimental studies of wave impact underneath decks of offshore platforms. (Dr.Ing. Thesis) |
| MTA-2001-144 | Wang, Lihua, MK | Probabilistic Analysis of Nonlinear Wave-induced Loads on Ships. (Dr.Ing. Thesis) |
| MTA-2001-145 | Kristensen, Odd H. Holt, MK | Ultimate Capacity of Aluminium Plates under Multiple Loads, Considering HAZ Properties. (Dr.Ing. Thesis) |
| MTA-2001-146 | Greco, Marilena, MH | A Two-Dimensional Study of Green-Water |

| | | |
|---|---|---|
| | | Loading. (Dr.Ing. Thesis) |
| MTA-2001-147 | Heggelund, Svein E., MK | Calculation of Global Design Loads and Load Effects in Large High Speed Catamarans. (Dr.Ing. Thesis) |
| MTA-2001-148 | Babalola, Olusegun T., MK | Fatigue Strength of Titanium Risers – Defect Sensitivity. (Dr.Ing. Thesis) |
| MTA-2001-149 | Mohammed, Abuu K., MK | Nonlinear Shell Finite Elements for Ultimate Strength and Collapse Analysis of Ship Structures. (Dr.Ing. Thesis) |
| MTA-2002-150 | Holmedal, Lars E., MH | Wave-current interactions in the vicinity of the sea bed. (Dr.Ing. Thesis) |
| MTA-2002-151 | Rognebakke, Olav F., MH | Sloshing in rectangular tanks and interaction with ship motions. (Dr.Ing. Thesis) |
| MTA-2002-152 | Lader, Pål Furset, MH | Geometry and Kinematics of Breaking Waves. (Dr.Ing. Thesis) |
| MTA-2002-153 | Yang, Qinzheng, MH | Wash and wave resistance of ships in finite water depth. (Dr.Ing. Thesis) |
| MTA-2002-154 | Melhus, Øyvin, MM | Utilization of VOC in Diesel Engines. Ignition and combustion of VOC released by crude oil tankers. (Dr.Ing. Thesis) |
| MTA-2002-155 | Ronæss, Marit, MH | Wave Induced Motions of Two Ships Advancing on Parallel Course. (Dr.Ing. Thesis) |
| MTA-2002-156 | Økland, Ole D., MK | Numerical and experimental investigation of whipping in twin hull vessels exposed to severe wet deck slamming. (Dr.Ing. Thesis) |
| MTA-2002-157 | Ge, Chunhua, MK | Global Hydroelastic Response of Catamarans due to Wet Deck Slamming. (Dr.Ing. Thesis) |
| MTA-2002-158 | Byklum, Eirik, MK | Nonlinear Shell Finite Elements for Ultimate Strength and Collapse Analysis of Ship Structures. (Dr.Ing. Thesis) |
| IMT-2003-1 | Chen, Haibo, MK | Probabilistic Evaluation of FPSO-Tanker Collision in Tandem Offloading Operation. (Dr.Ing. Thesis) |
| IMT-2003-2 | Skaugset, Kjetil Bjørn, MK | On the Suppression of Vortex Induced Vibrations of Circular Cylinders by Radial Water Jets. (Dr.Ing. Thesis) |
| IMT-2003-3 | Chezhian, Muthu | Three-Dimensional Analysis of Slamming. (Dr.Ing. Thesis) |
| IMT-2003-4 | Buhaug, Øyvind | Deposit Formation on Cylinder Liner Surfaces in Medium Speed Engines. (Dr.Ing. Thesis) |
| IMT-2003-5 | Tregde, Vidar | Aspects of Ship Design: Optimization of Aft Hull with Inverse Geometry Design. (Dr.Ing. Thesis) |
| IMT- | Wist, Hanne Therese | Statistical Properties of Successive Ocean Wave |

| | | |
|---|---|---|
| 2003-6 | | Parameters. (Dr.Ing. Thesis) |
| IMT-2004-7 | Ransau, Samuel | Numerical Methods for Flows with Evolving Interfaces. (Dr.Ing. Thesis) |
| IMT-2004-8 | Soma, Torkel | Blue-Chip or Sub-Standard. A data interrogation approach of identity safety characteristics of shipping organization. (Dr.Ing. Thesis) |
| IMT-2004-9 | Ersdal, Svein | An experimental study of hydrodynamic forces on cylinders and cables in near axial flow. (Dr.Ing. Thesis) |
| IMT-2005-10 | Brodtkorb, Per Andreas | The Probability of Occurrence of Dangerous Wave Situations at Sea. (Dr.Ing. Thesis) |
| IMT-2005-11 | Yttervik, Rune | Ocean current variability in relation to offshore engineering. (Dr.Ing. Thesis) |
| IMT-2005-12 | Fredheim, Arne | Current Forces on Net-Structures. (Dr.Ing. Thesis) |
| IMT-2005-13 | Heggernes, Kjetil | Flow around marine structures. (Dr.Ing. Thesis |
| IMT-2005-14 | Fouques, Sebastien | Lagrangian Modelling of Ocean Surface Waves and Synthetic Aperture Radar Wave Measurements. (Dr.Ing. Thesis) |
| IMT-2006-15 | Holm, Håvard | Numerical calculation of viscous free surface flow around marine structures. (Dr.Ing. Thesis) |
| IMT-2006-16 | Bjørheim, Lars G. | Failure Assessment of Long Through Thickness Fatigue Cracks in Ship Hulls. (Dr.Ing. Thesis) |
| IMT-2006-17 | Hansson, Lisbeth | Safety Management for Prevention of Occupational Accidents. (Dr.Ing. Thesis) |
| IMT-2006-18 | Zhu, Xinying | Application of the CIP Method to Strongly Nonlinear Wave-Body Interaction Problems. (Dr.Ing. Thesis) |
| IMT-2006-19 | Reite, Karl Johan | Modelling and Control of Trawl Systems. (Dr.Ing. Thesis) |
| IMT-2006-20 | Smogeli, Øyvind Notland | Control of Marine Propellers. From Normal to Extreme Conditions. (Dr.Ing. Thesis) |
| IMT-2007-21 | Storhaug, Gaute | Experimental Investigation of Wave Induced Vibrations and Their Effect on the Fatigue Loading of Ships. (Dr.Ing. Thesis) |
| IMT-2007-22 | Sun, Hui | A Boundary Element Method Applied to Strongly Nonlinear Wave-Body Interaction Problems. (PhD Thesis, CeSOS) |
| IMT-2007-23 | Rustad, Anne Marthine | Modelling and Control of Top Tensioned Risers. (PhD Thesis, CeSOS) |
| IMT-2007-24 | Johansen, Vegar | Modelling flexible slender system for real-time simulations and control applications |
| IMT-2007-25 | Wroldsen, Anders Sunde | Modelling and control of tensegrity structures. |

| | | |
|---|---|---|
| | | (PhD Thesis, CeSOS) |
| IMT-2007-26 | Aronsen, Kristoffer Høye | An experimental investigation of in-line and combined inline and cross flow vortex induced vibrations. (Dr. avhandling, IMT) |
| IMT-2007-27 | Gao, Zhen | Stochastic Response Analysis of Mooring Systems with Emphasis on Frequency-domain Analysis of Fatigue due to Wide-band Response Processes (PhD Thesis, CeSOS) |
| IMT-2007-28 | Thorstensen, Tom Anders | Lifetime Profit Modelling of Ageing Systems Utilizing Information about Technical Condition. (Dr.ing. thesis, IMT) |
| IMT-2008-29 | Refsnes, Jon Erling Gorset | Nonlinear Model-Based Control of Slender Body AUVs (PhD Thesis, IMT) |
| IMT-2008-30 | Berntsen, Per Ivar B. | Structural Reliability Based Position Mooring. (PhD-Thesis, IMT) |
| IMT-2008-31 | Ye, Naiquan | Fatigue Assessment of Aluminium Welded Box-stiffener Joints in Ships (Dr.ing. thesis, IMT) |
| IMT-2008-32 | Radan, Damir | Integrated Control of Marine Electrical Power Systems. (PhD-Thesis, IMT) |
| IMT-2008-33 | Thomassen, Paul | Methods for Dynamic Response Analysis and Fatigue Life Estimation of Floating Fish Cages. (Dr.ing. thesis, IMT) |
| IMT-2008-34 | Pákozdi, Csaba | A Smoothed Particle Hydrodynamics Study of Two-dimensional Nonlinear Sloshing in Rectangular Tanks. (Dr.ing.thesis, IMT/ CeSOS) |
| IMT-2007-35 | Grytøyr, Guttorm | A Higher-Order Boundary Element Method and Applications to Marine Hydrodynamics. (Dr.ing.thesis, IMT) |
| IMT-2008-36 | Drummen, Ingo | Experimental and Numerical Investigation of Nonlinear Wave-Induced Load Effects in Containerships considering Hydroelasticity. (PhD thesis, CeSOS) |
| IMT-2008-37 | Skejic, Renato | Maneuvering and Seakeeping of a Singel Ship and of Two Ships in Interaction. (PhD-Thesis, CeSOS) |
| IMT-2008-38 | Harlem, Alf | An Age-Based Replacement Model for Repairable Systems with Attention to High-Speed Marine Diesel Engines. (PhD-Thesis, IMT) |
| IMT-2008-39 | Alsos, Hagbart S. | Ship Grounding. Analysis of Ductile Fracture, Bottom Damage and Hull Girder Response. (PhD-thesis, IMT) |
| IMT-2008-40 | Graczyk, Mateusz | Experimental Investigation of Sloshing Loading and Load Effects in Membrane LNG Tanks Subjected to Random Excitation. (PhD-thesis, CeSOS) |
| IMT-2008-41 | Taghipour, Reza | Efficient Prediction of Dynamic Response for Flexible amd Multi-body Marine Structures. (PhD- |

| | | |
|---|---|---|
| | | thesis, CeSOS) |
| IMT-2008-42 | Ruth, Eivind | Propulsion control and thrust allocation on marine vessels. (PhD thesis, CeSOS) |
| IMT-2008-43 | Nystad, Bent Helge | Technical Condition Indexes and Remaining Useful Life of Aggregated Systems. PhD thesis, IMT |
| IMT-2008-44 | Soni, Prashant Kumar | Hydrodynamic Coefficients for Vortex Induced Vibrations of Flexible Beams, PhD thesis, CeSOS |
| IMT-2009-45 | Amlashi, Hadi K.K. | Ultimate Strength and Reliability-based Design of Ship Hulls with Emphasis on Combined Global and Local Loads. PhD Thesis, IMT |
| IMT-2009-46 | Pedersen, Tom Arne | Bond Graph Modelling of Marine Power Systems. PhD Thesis, IMT |
| IMT-2009-47 | Kristiansen, Trygve | Two-Dimensional Numerical and Experimental Studies of Piston-Mode Resonance. PhD-Thesis, CeSOS |
| IMT-2009-48 | Ong, Muk Chen | Applications of a Standard High Reynolds Number Model and a Stochastic Scour Prediction Model for Marine Structures. PhD-thesis, IMT |
| IMT-2009-49 | Hong, Lin | Simplified Analysis and Design of Ships subjected to Collision and Grounding. PhD-thesis, IMT |
| IMT-2009-50 | Koushan, Kamran | Vortex Induced Vibrations of Free Span Pipelines, PhD thesis, IMT |
| IMT-2009-51 | Korsvik, Jarl Eirik | Heuristic Methods for Ship Routing and Scheduling. PhD-thesis, IMT |
| IMT-2009-52 | Lee, Jihoon | Experimental Investigation and Numerical in Analyzing the Ocean Current Displacement of Longlines. Ph.d.-Thesis, IMT. |
| IMT-2009-53 | Vestbøstad, Tone Gran | A Numerical Study of Wave-in-Deck Impact usin a Two-Dimensional Constrained Interpolation Profile Method, Ph.d.thesis, CeSOS. |
| IMT-2009-54 | Bruun, Kristine | Bond Graph Modelling of Fuel Cells for Marine Power Plants. Ph.d.-thesis, IMT |
| IMT 2009-55 | Holstad, Anders | Numerical Investigation of Turbulence in a Sekwed Three-Dimensional Channel Flow, Ph.d.-thesis, IMT. |
| IMT 2009-56 | Ayala-Uraga, Efren | Reliability-Based Assessment of Deteriorating Ship-shaped Offshore Structures, Ph.d.-thesis, IMT |
| IMT 2009-57 | Kong, Xiangjun | A Numerical Study of a Damaged Ship in Beam Sea Waves. Ph.d.-thesis, IMT/CeSOS. |
| IMT 2010-58 | Kristiansen, David | Wave Induced Effects on Floaters of Aquaculture Plants, Ph.d.-thesis, CeSOS. |

| | | |
|---|---|---|
| IMT 2010-59 | Ludvigsen, Martin | An ROV-Toolbox for Optical and Acoustic Scientific Seabed Investigation. Ph.d.-thesis IMT. |
| IMT 2010-60 | Hals, Jørgen | Modelling and Phase Control of Wave-Energy Converters. Ph.d.thesis, CeSOS. |
| IMT 2010- 61 | Shu, Zhi | Uncertainty Assessment of Wave Loads and Ultimate Strength of Tankers and Bulk Carriers in a Reliability Framework. Ph.d. Thesis, IMT/ CeSOS |
| IMT 2010-62 | Shao, Yanlin | Numerical Potential-Flow Studies on Weakly-Nonlinear Wave-Body Interactions with/without Small Forward Speed, Ph.d.thesis,CeSOS. |
| IMT 2010-63 | Califano, Andrea | Dynamic Loads on Marine Propellers due to Intermittent Ventilation. Ph.d.thesis, IMT. |
| IMT 2010-64 | El Khoury, George | Numerical Simulations of Massively Separated Turbulent Flows, Ph.d.-thesis, IMT |
| IMT 2010-65 | Seim, Knut Sponheim | Mixing Process in Dense Overflows with Emphasis on the Faroe Bank Channel Overflow. Ph.d.thesis, IMT |
| IMT 2010-66 | Jia, Huirong | Structural Analysis of Intect and Damaged Ships in a Collission Risk Analysis Perspective. Ph.d.thesis CeSoS. |
| IMT 2010-67 | Jiao, Linlin | Wave-Induced Effects on a Pontoon-type Very Large Floating Structures (VLFS). Ph.D.-thesis, CeSOS. |
| IMT 2010-68 | Abrahamsen, Bjørn Christian | Sloshing Induced Tank Roof with Entrapped Air Pocket. Ph.d.thesis, CeSOS. |
| IMT 2011-69 | Karimirad, Madjid | Stochastic Dynamic Response Analysis of Spar-Type Wind Turbines with Catenary or Taut Mooring Systems. Ph.d.-thesis, CeSOS. |
| IMT - 2011-70 | Erlend Meland | Condition Monitoring of Safety Critical Valves. Ph.d.-thesis, IMT. |
| IMT – 2011-71 | Yang, Limin | Stochastic Dynamic System Analysis of Wave Energy Converter with Hydraulic Power Take-Off, with Particular Reference to Wear Damage Analysis, Ph.d. Thesis, CeSOS. |
| IMT – 2011-72 | Visscher, Jan | Application of Particla Image Velocimetry on Turbulent Marine Flows, Ph.d.Thesis, IMT. |
| IMT – 2011-73 | Su, Biao | Numerical Predictions of Global and Local Ice Loads on Ships. Ph.d.Thesis, CeSOS. |
| IMT – 2011-74 | Liu, Zhenhui | Analytical and Numerical Analysis of Iceberg Collision with Ship Structures. Ph.d.Thesis, IMT. |
| IMT – 2011-75 | Aarsæther, Karl Gunnar | Modeling and Analysis of Ship Traffic by Observation and Numerical Simulation. Ph.d.Thesis, IMT. |

| | | |
|---|---|---|
| Imt – 2011-76 | Wu, Jie | Hydrodynamic Force Identification from Stochastic Vortex Induced Vibration Experiments with Slender Beams. Ph.d.Thesis, IMT. |
| Imt – 2011-77 | Amini, Hamid | Azimuth Propulsors in Off-design Conditions. Ph.d.Thesis, IMT. |
| IMT – 2011-78 | Nguyen, Tan-Hoi | Toward a System of Real-Time Prediction and Monitoring of Bottom Damage Conditions During Ship Grounding. Ph.d.thesis, IMT. |
| IMT- 2011-79 | Tavakoli, Mohammad T. | Assessment of Oil Spill in Ship Collision and Grounding, Ph.d.thesis, IMT. |
| IMT- 2011-80 | Guo, Bingjie | Numerical and Experimental Investigation of Added Resistance in Waves. Ph.d.Thesis, IMT. |
| IMT- 2011-81 | Chen, Qiaofeng | Ultimate Strength of Aluminium Panels, considering HAZ Effects, IMT |
| IMT- 2012-82 | Kota, Ravikiran S. | Wave Loads on Decks of Offshore Structures in Random Seas, CeSOS. |
| IMT- 2012-83 | Sten, Ronny | Dynamic Simulation of Deep Water Drilling Risers with Heave Compensating System, IMT. |
| IMT- 2012-84 | Berle, Øyvind | Risk and resilience in global maritime supply chains, IMT. |
| IMT- 2012-85 | Fang, Shaoji | Fault Tolerant Position Mooring Control Based on Structural Reliability, CeSOS. |
| IMT- 2012-86 | You, Jikun | Numerical studies on wave forces and moored ship motions in intermediate and shallow water, CeSOS. |
| IMT- 2012-87 | Xiang ,Xu | Maneuvering of two interacting ships in waves, CeSOS |
| IMT- 2012-88 | Dong, Wenbin | Time-domain fatigue response and reliability analysis of offshore wind turbines with emphasis on welded tubular joints and gear components, CeSOS |
| IMT- 2012-89 | Zhu, Suji | Investigation of Wave-Induced Nonlinear Load Effects in Open Ships considering Hull Girder Vibrations in Bending and Torsion, CeSOS |
| IMT- 2012-90 | Zhou, Li | Numerical and Experimental Investigation of Station-keeping in Level Ice, CeSOS |
| IMT- 2012-91 | Ushakov, Sergey | Particulate matter emission characteristics from diesel enignes operating on conventional and alternative marine fuels, IMT |
| IMT- 2013-1 | Yin, Decao | Experimental and Numerical Analysis of Combined In-line and Cross-flow Vortex Induced Vibrations, CeSOS |

| | | |
|---|---|---|
| IMT-2013-2 | Kurniawan, Adi | Modelling and geometry optimisation of wave energy converters, CeSOS |
| IMT-2013-3 | Al Ryati, Nabil | Technical condition indexes doe auxiliary marine diesel engines, IMT |
| IMT-2013-4 | Firoozkoohi, Reza | Experimental, numerical and analytical investigation of the effect of screens on sloshing, CeSOS |
| IMT-2013-5 | Ommani, Babak | Potential-Flow Predictions of a Semi-Displacement Vessel Including Applications to Calm Water Broaching, CeSOS |
| IMT-2013-6 | Xing, Yihan | Modelling and analysis of the gearbox in a floating spar-type wind turbine, CeSOS |
| IMT-7-2013 | Balland, Océane | Optimization models for reducing air emissions from ships, IMT |
| IMT-8-2013 | Yang, Dan | Transitional wake flow behind an inclined flat plate-----Computation and analysis, IMT |
| IMT-9-2013 | Abdillah, Suyuthi | Prediction of Extreme Loads and Fatigue Damage for a Ship Hull due to Ice Action, IMT |
| IMT-10-2013 | Ramìrez, Pedro Agustìn Pèrez | Ageing management and life extension of technical systems-<br>Concepts and methods applied to oil and gas facilities, IMT |
| IMT-11-2013 | Chuang, Zhenju | Experimental and Numerical Investigation of Speed Loss due to Seakeeping and Maneuvering. IMT |
| IMT-12-2013 | Etemaddar, Mahmoud | Load and Response Analysis of Wind Turbines under Atmospheric Icing and Controller System Faults with Emphasis on Spar Type Floating Wind Turbines, IMT |
| IMT-13-2013 | Lindstad, Haakon | Strategies and measures for reducing maritime CO2 emissons, IMT |
| IMT-14-2013 | Haris, Sabril | Damage interaction analysis of ship collisions, IMT |
| IMT-15-2013 | Shainee, Mohamed | Conceptual Design, Numerical and Experimental Investigation of a SPM Cage Concept for Offshore Mariculture, IMT |
| IMT-16-2013 | Gansel, Lars | Flow past porous cylinders and effects of biofouling and fish behavior on the flow in and around Atlantic salmon net cages, IMT |
| IMT-17-2013 | Gaspar, Henrique | Handling Aspects of Complexity in Conceptual Ship Design, IMT |
| IMT-18-2013 | Thys, Maxime | Theoretical and Experimental Investigation of a Free Running Fishing Vessel at Small Frequency of Encounter, CeSOS |
| IMT-19-2013 | Aglen, Ida | VIV in Free Spanning Pipelines, CeSOS |

| | | |
|---|---|---|
| IMT-1-2014 | Song, An | Theoretical and experimental studies of wave diffraction and radiation loads on a horizontally submerged perforated plate, CeSOS |
| IMT-2-2014 | Rogne, Øyvind Ygre | Numerical and Experimental Investigation of a Hinged 5-body Wave Energy Converter, CeSOS |
| IMT-3-2014 | Dai, Lijuan | Safe and efficient operation and maintenance of offshore wind farms ,IMT |
| IMT-4-2014 | Bachynski, Erin Elizabeth | Design and Dynamic Analysis of Tension Leg Platform Wind Turbines, CeSOS |
| IMT-5-2014 | Wang, Jingbo | Water Entry of Freefall Wedged – Wedge motions and Cavity Dynamics, CeSOS |
| IMT-6-2014 | Kim, Ekaterina | Experimental and numerical studies related to the coupled behavior of ice mass and steel structures during accidental collisions, IMT |
| IMT-7-2014 | Tan, Xiang | Numerical investigation of ship's continuous- mode icebreaking in leverl ice, CeSOS |
| IMT-8-2014 | Muliawan, Made Jaya | Design and Analysis of Combined Floating Wave and Wind Power Facilities, with Emphasis on Extreme Load Effects of the Mooring System, CeSOS |
| IMT-9-2014 | Jiang, Zhiyu | Long-term response analysis of wind turbines with an emphasis on fault and shutdown conditions, IMT |
| IMT-10-2014 | Dukan, Fredrik | ROV Motion Control Systems, IMT |
| IMT-11-2014 | Grimsmo, Nils I. | Dynamic simulations of hydraulic cylinder for heave compensation of deep water drilling risers, IMT |
| IMT-12-2014 | Kvittem, Marit I. | Modelling and response analysis for fatigue design of a semisubmersible wind turbine, CeSOS |
| IMT-13-2014 | Akhtar, Juned | The Effects of Human Fatigue on Risk at Sea, IMT |
| IMT-14-2014 | Syahroni, Nur | Fatigue Assessment of Welded Joints Taking into Account Effects of Residual Stress, IMT |
| IMT-1-2015 | Bøckmann, Eirik | Wave Propulsion of ships, IMT |
| IMT-2-2015 | Wang, Kai | Modelling and dynamic analysis of a semi-submersible floating vertical axis wind turbine, CeSOS |
| IMT-3-2015 | Fredriksen, Arnt Gunvald | A numerical and experimental study of a two-dimensional body with moonpool in waves and current, CeSOS |
| IMT-4-2015 | Jose Patricio Gallardo Canabes | Numerical studies of viscous flow around bluff bodies, IMT |

| | | |
|---|---|---|
| IMT-5-2015 | Vegard Longva | Formulation and application of finite element techniques for slender marine structures subjected to contact interactions, IMT |
| IMT-6-2015 | Jacobus De Vaal | Aerodynamic modelling of floating wind turbines, CeSOS |
| IMT-7-2015 | Fachri Nasution | Fatigue Performance of Copper Power Conductors, IMT |
| IMT-8-2015 | Oleh I Karpa | Development of bivariate extreme value distributions for applications in marine technology,CeSOS |
| IMT-9-2015 | Daniel de Almeida Fernandes | An output feedback motion control system for ROVs, AMOS |
| IMT-10-2015 | Bo Zhao | Particle Filter for Fault Diagnosis: Application to Dynamic Positioning Vessel and Underwater Robotics, CeSOS |
| IMT-11-2015 | Wenting Zhu | Impact of emission allocation in maritime transportation, IMT |
| IMT-12-2015 | Amir Rasekhi Nejad | Dynamic Analysis and Design of Gearboxes in Offshore Wind Turbines in a Structural Reliability Perspective, CeSOS |
| IMT-13-2015 | Arturo Jesùs Ortega Malca | Dynamic Response of Flexibles Risers due to Unsteady Slug Flow, CeSOS |
| IMT-14-2015 | Dagfinn Husjord | Guidance and decision-support system for safe navigation of ships operating in close proximity, IMT |
| IMT-15-2015 | Anirban Bhattacharyya | Ducted Propellers: Behaviour in Waves and Scale Effects, IMT |
| IMT-16-2015 | Qin Zhang | Image Processing for Ice Parameter Identification in Ice Management, IMT |
| IMT-1-2016 | Vincentius Rumawas | Human Factors in Ship Design and Operation: An Experiential Learning, IMT |
| IMT-2-2016 | Martin Storheim | Structural response in ship-platform and ship-ice collisions, IMT |
| IMT-3-2016 | Mia Abrahamsen Prsic | Numerical Simulations of the Flow around single and Tandem Circular Cylinders Close to a Plane Wall, IMT |
| IMT-4-2016 | Tufan Arslan | Large-eddy simulations of cross-flow around ship sections, IMT |

| | | |
|---|---|---|
| IMT-5-2016 | Pierre Yves-Henry | Parametrisation of aquatic vegetation in hydraulic and coastal research,IMT |
| IMT-6-2016 | Lin Li | Dynamic Analysis of the Instalation of Monopiles for Offshore Wind Turbines, CeSOS |
| IMT-7-2016 | Øivind Kåre Kjerstad | Dynamic Positioning of Marine Vessels in Ice, IMT |
| IMT-8-2016 | Xiaopeng Wu | Numerical Analysis of Anchor Handling and Fish Trawling Operations in a Safety Perspective, CeSOS |
| IMT-9-2016 | Zhengshun Cheng | Integrated Dynamic Analysis of Floating Vertical Axis Wind Turbines, CeSOS |
| IMT-10-2016 | Ling Wan | Experimental and Numerical Study of a Combined Offshore Wind and Wave Energy Converter Concept |
| IMT-11-2016 | Wei Chai | Stochastic dynamic analysis and reliability evaluation of the roll motion for ships in random seas, CeSOS |
| IMT-12-2016 | Øyvind Selnes Patricksson | Decision support for conceptual ship design with focus on a changing life cycle and future uncertainty, IMT |
| IMT-13-2016 | Mats Jørgen Thorsen | Time domain analysis of vortex-induced vibrations, IMT |
| IMT-14-2016 | Edgar McGuinness | Safety in the Norwegian Fishing Fleet – Analysis and measures for improvement, IMT |
| IMT-15-2016 | Sepideh Jafarzadeh | Energy effiency and emission abatement in the fishing fleet, IMT |
| IMT-16-2016 | Wilson Ivan Guachamin Acero | Assessment of marine operations for offshore wind turbine installation with emphasis on response-based operational limits, IMT |
| IMT-17-2016 | Mauro Candeloro | Tools and Methods for Autonomous Operations on Seabed and Water Coumn using Underwater Vehicles, IMT |
| IMT-18-2016 | Valentin Chabaud | Real-Time Hybrid Model Testing of Floating Wind Tubines, IMT |
| IMT-1-2017 | Mohammad Saud Afzal | Three-dimensional streaming in a sea bed boundary layer |
| IMT-2-2017 | Peng Li | A Theoretical and Experimental Study of Wave-induced Hydroelastic Response of a Circular Floating Collar |
| IMT-3-2017 | Martin Bergström | A simulation-based design method for arctic maritime transport systems |

| | | |
|---|---|---|
| IMT-4-2017 | Bhushan Taskar | The effect of waves on marine propellers and propulsion |
| IMT-5-2017 | Mohsen Bardestani | A two-dimensional numerical and experimental study of a floater with net and sinker tube in waves and current |
| IMT-6-2017 | Fatemeh Hoseini Dadmarzi | Direct Numerical Simualtion of turbulent wakes behind different plate configurations |
| IMT-7-2017 | Michel R. Miyazaki | Modeling and control of hybrid marine power plants |
| IMT-8-2017 | Giri Rajasekhar Gunnu | Safety and effiency enhancement of anchor handling operations with particular emphasis on the stability of anchor handling vessels |
| IMT-9-2017 | Kevin Koosup Yum | Transient Performance and Emissions of a Turbocharged Diesel Engine for Marine Power Plants |
| IMT-10-2017 | Zhaolong Yu | Hydrodynamic and structural aspects of ship collisions |
| IMT-11-2017 | Martin Hassel | Risk Analysis and Modelling of Allisions between Passing Vessels and Offshore Installations |
| IMT-12-2017 | Astrid H. Brodtkorb | Hybrid Control of Marine Vessels – Dynamic Positioning in Varying Conditions |
| IMT-13-2017 | Kjersti Bruserud | Simultaneous stochastic model of waves and current for prediction of structural design loads |
| IMT-14-2017 | Finn-Idar Grøtta Giske | Long-Term Extreme Response Analysis of Marine Structures Using Inverse Reliability Methods |
| IMT-15-2017 | Stian Skjong | Modeling and Simulation of Maritime Systems and Operations for Virtual Prototyping using co-Simulations |
| IMT-1-2018 | Yingguang Chu | Virtual Prototyping for Marine Crane Design and Operations |
| IMT-2-2018 | Sergey Gavrilin | Validation of ship manoeuvring simulation models |
| IMT-3-2018 | Jeevith Hegde | Tools and methods to manage risk in autonomous subsea inspection,maintenance and repair operations |
| IMT-4-2018 | Ida M. Strand | Sea Loads on Closed Flexible Fish Cages |
| IMT-5-2018 | Erlend Kvinge Jørgensen | Navigation and Control of Underwater Robotic Vehicles |

| | | |
|---|---|---|
| IMT-6-2018 | Bård Stovner | Aided Intertial Navigation of Underwater Vehicles |
| IMT-7-2018 | Erlend Liavåg Grotle | Thermodynamic Response Enhanced by Sloshing in Marine LNG Fuel Tanks |
| IMT-8-2018 | Børge Rokseth | Safety and Verification of Advanced Maritime Vessels |
| IMT-9-2018 | Jan Vidar Ulveseter | Advances in Semi-Empirical Time Domain Modelling of Vortex-Induced Vibrations |
| IMT-10-2018 | Chenyu Luan | Design and analysis for a steel braceless semi-submersible hull for supporting a 5-MW horizontal axis wind turbine |
| IMT-11-2018 | Carl Fredrik Rehn | Ship Design under Uncertainty |
| IMT-12-2018 | Øyvind Ødegård | Towards Autonomous Operations and Systems in Marine Archaeology |
| IMT-13-2018 | Stein Melvær Nornes | Guidance and Control of Marine Robotics for Ocean Mapping and Monitoring |
| IMT-14-2018 | Petter Norgren | Autonomous Underwater Vehicles in Arctic Marine Operations: Arctic marine research and ice monitoring |
| IMT-15-2018 | Minjoo Choi | Modular Adaptable Ship Design for Handling Uncertainty in the Future Operating Context |
| MT-16-2018 | Ole Alexander Eidsvik | Dynamics of Remotely Operated Underwater Vehicle Systems |
| IMT-17-2018 | Mahdi Ghane | Fault Diagnosis of Floating Wind Turbine Drivetrain- Methodologies and Applications |
| IMT-18-2018 | Christoph Alexander Thieme | Risk Analysis and Modelling of Autonomous Marine Systems |
| IMT-19-2018 | Yugao Shen | Operational limits for floating-collar fish farms in waves and current, without and with well-boat presence |
| IMT-20-2018 | Tianjiao Dai | Investigations of Shear Interaction and Stresses in Flexible Pipes and Umbilicals |
| IMT-21-2018 | Sigurd Solheim Pettersen | Resilience by Latent Capabilities in Marine Systems |
| IMT-22-2018 | Thomas Sauder | Fidelity of Cyber-physical Empirical Methods. Application to the Active Truncation of Slender Marine Structures |
| IMT-23-2018 | Jan-Tore Horn | Statistical and Modelling Uncertainties in the Design of Offshore Wind Turbines |

| | | |
|---|---|---|
| IMT-24-2018 | Anna Swider | Data Mining Methods for the Analysis of Power Systems of Vessels |
| IMT-1-2019 | Zhao He | Hydrodynamic study of a moored fish farming cage with fish influence |
| IMT-2-2019 | Isar Ghamari | Numerical and Experimental Study on the Ship Parametric Roll Resonance and the Effect of Anti-Roll Tank |
| IMT-3-2019 | Håkon Strandenes | Turbulent Flow Simulations at Higher Reynolds Numbers |
| IMT-4-2019 | Siri Mariane Holen | Safety in Norwegian Fish Farming – Concepts and Methods for Improvement |
| IMT-5-2019 | Ping Fu | Reliability Analysis of Wake-Induced Riser Collision |
| IMT-6-2019 | Vladimir Krivopolianskii | Experimental Investigation of Injection and Combustion Processes in Marine Gas Engines using Constant Volume Rig |
| IMT-7-2019 | Anna Maria Kozlowska | Hydrodynamic Loads on Marine Propellers Subject to Ventilation and out of Water Condition. |
| IMT-8-2019 | Hans-Martin Heyn | Motion Sensing on Vessels Operating in Sea Ice: A Local Ice Monitoring System for Transit and Stationkeeping Operations under the Influence of Sea Ice |
| IMT-9-2019\| | Stefan Vilsen | Method for Real-Time Hybrid Model Testing of Ocean Structures – Case on Slender Marine Systems |
| IMT-10-2019 | Finn-Christian W. Hanssen | Non-Linear Wave-Body Interaction in Severe Waves |
| IMT-11-2019 | Trygve Olav Fossum | Adaptive Sampling for Marine Robotics |
| IMT-12-2019 | Jørgen Bremnes Nielsen | Modeling and Simulation for Design Evaluation |
| IMT-13-2019 | Yuna Zhao | Numerical modelling and dyncamic analysis of offshore wind turbine blade installation |
| IMT-14-2019 | Daniela Myland | Experimental and Theoretical Investigations on the Ship Resistance in Level Ice |
| IMT-15-2019 | Zhengru Ren | Advanced control algorithms to support automated offshore wind turbine installation |
| IMT-16-2019 | Drazen Polic | Ice-propeller impact analysis using an inverse propulsion machinery simulation approach |
| IMT-17-2019 | Endre Sandvik | Sea passage scenario simulation for ship system performance evaluation |

| | | |
|---|---|---|
| IMT-18-2019 | Loup Suja-Thauvin | Response of Monopile Wind Turbines to Higher Order Wave Loads |
| IMT-19-2019 | Emil Smilden | Structural control of offshore wind turbines – Increasing the role of control design in offshore wind farm development |
| IMT-20-2019 | Aleksandar-Sasa Milakovic | On equivalent ice thickness and machine learning in ship ice transit simulations |
| IMT-1-2020 | Amrit Shankar Verma | Modelling, Analysis and Response-based Operability Assessment of Offshore Wind Turbine Blade Installation with Emphasis on Impact Damages |
| IMT-2-2020 | Bent Oddvar Arnesen Haugaløkken | Autonomous Technology for Inspection, Maintenance and Repair Operations in the Norwegian Aquaculture |
| IMT-3-2020 | Seongpil Cho | Model-based fault detection and diagnosis of a blade pitch system in floating wind turbines |
| IMT-4-2020 | Jose Jorge Garcia Agis | Effectiveness in Decision-Making in Ship Design under Uncertainty |
| IMT-5-2020 | Thomas H. Viuff | Uncertainty Assessment of Wave-and Current-induced Global Response of Floating Bridges |
| IMT-6-2020 | Fredrik Mentzoni | Hydrodynamic Loads on Complex Structures in the Wave Zone |
| IMT-7-2020 | Senthuran Ravinthrakumar | Numerical and Experimental Studies of Resonant Flow in Moonpools in Operational Conditions |
| IMT-8-2020 | Stian Skaalvik Sandøy | Acoustic-based Probabilistic Localization and Mapping using Unmanned Underwater Vehicles for Aquaculture Operations |
| IMT-9-2020 | Kun Xu | Design and Analysis of Mooring System for Semi-submersible Floating Wind Turbine in Shallow Water |
| IMT-10-2020 | Jianxun Zhu | Cavity Flows and Wake Behind an Elliptic Cylinder Translating Above the Wall |
| IMT-11-2020 | Sandra Hogenboom | Decision-making within Dynamic Positioning Operations in the Offshore Industry – A Human Factors based Approach |
| IMT-12-2020 | Woongshik Nam | Structural Resistance of Ship and Offshore Structures Exposed to the Risk of Brittle Failure |
| IMT-13-2020 | Svenn Are Tutturen Værnø | Transient Performance in Dynamic Positioning of Ships: Investigation of Residual Load Models and Control Methods for Effective Compensation |
| IMT-14-2020 | Mohd Atif Siddiqui | Experimental and Numerical Hydrodynamics Analysis of a Damaged Ship in Waves |
| IMT-15-2020 | John Marius Hegseth | Efficient Modelling and Design Optimization of Large Floating Wind Turbines |

| | | |
|---|---|---|
| IMT-16-2020 | Asle Natskår | Reliability-based Assessment of Marine Operations with Emphasis on Sea Transport on Barges |
| IMT-17-2020 | Shi Deng | Experimental and Numerical Study of Hydrodynamic Responses of a Twin-Tube Submerged Floating Tunnel Considering Vortex-Induced Vibration |